Effect of Ultrasound on the Hydrophobicity of Microparticles

Jean de Bruin Jordaan

A dissertation submitted to the Faculty of Engineering and the Built Environment, University of the Witwatersrand, Johannesburg, in fulfilment of the requirements for the degree of Master of Science in Engineering.

Johannesburg, 2022

Declaration

I declare that this dissertation is my own, unaided work, except where otherwise acknowledged. It is being submitted for the degree of Master of Science in Engineering to the University of the Witwatersrand, Johannesburg. It has not been submitted before for any degree or examination to any other university.

Signed this 29^{th} day of August, 2022

Jean de Bruin Jordaan

Abstract

Ultrasound is used extensively in medical applications and has uses in industrial applications as well. Hydrophobic microparticles are acoustically active and are manipulated using ultrasound in various ways with applications as ultrasound contrast agents and ultrasound-guided drug delivery. The hydrophobicity of microparticles has been qualitatively observed to change when exposed to ultrasound. This phenomenon has not been previously described nor verified through a quantitative measurement technique. This research investigated and quantified the effect of ultrasound on microparticle hydrophobicity. Hydrophobic carbon black microparticles were exposed to various regimes of ultrasound. Microparticle samples were suspended in distilled water and exposed to various controlled acoustic regimes, at various frequencies of 1-10 MHz and at various amplitudes of 0-100 kPa, for 5 min. The hydrophobicity of the samples is measured using a novel technique, the colourimetric partition coefficient measurement. The partition coefficient quantifies hydrophobicity through the partitioning phenomena of octanol and water. The partitioning coefficient value is then calculated through image colourimetry and digital image processing. The microparticles exposed to the various ultrasound regimes used had their hydrophobicity reduced by 42% compared to control null samples, with a statistical significance of $\approx 3\sigma$. This research provides the foundational knowledge for possible manipulation of microparticle hydrophobicity using ultrasound and its wide-reaching applications.

Acknowledgements

This research was performed under the auspices of the Biomedical Engineering Research Group at the University of the Witwatersrand, Johannesburg.

I wish to thank Professor Michiel Postema, who started with me on my Master's journey in the wonderful world of acoustics. The Covid-19 pandemic had the unfortunate effect of separating us with a rather unexpected and large social distancing policy.

I'd like to thank my supervisor, Doctor Craig Carlson, who inherited me as a Master's student and was going through a similar experience with his PhD research. Our paths crossed in the most unexpected ways, but your supervision and guidance have had a profound impact on my thinking.

I would like to thank my co-supervisor, Professor Kenneth Nixon, who likewise has had a similar impact.

Lastly, I would like to thank fellow colleagues of the school, my family and friends. Doing my Master's during a pandemic hasn't been easy. It has been a trying time for us all, and you've made it all worthwhile.

Contents

List of Figures

List of Tables

List of Symbols

Symbol	Description	Value/Units	See
	Constants		
α_{cbmp}	lumped optical molar-path-length attenuation coefficient for carbon black microparticles (cbmp) with a set optical path length, $\alpha_{\text{cbmp}} = \varepsilon_{\text{cbmp}} l_0$	$\text{m}^3\,\text{mol}^{-1}$	*p.133*
β_ν	lumped optical absorptivity for the cuvette material ν, with $\beta_\nu = \varepsilon_\nu \rho_{\text{mol}\,\nu} \chi$		*p.133*
β_φ	lumped optical absorptivity absorptivity for the phase φ, with $\beta_\varphi = \varepsilon_\varphi \rho_{\text{mol}\,\varphi} l_0$		*p.133*
$B_{\varphi\nu}$	total optical absorptivity of the phase φ (octanol or water) and the cuvette material ν, with $B_{\varphi\nu} = \beta_\varphi + \beta_\nu$		*p.133*
c_P	specific heat capacity of atmospheric air at constant pressure	$1.006\,\text{kJ}\,\text{kg}^{-1}\,\text{K}^{-1}$	*p.15*
c_V	specific heat capacity of atmospheric air at constant volume	$0.717\,\text{kJ}\,\text{kg}^{-1}\,\text{K}^{-1}$	*p.15*
ε	optical molar attenuation coefficient	$\text{m}^2\,\text{mol}^{-1}$	*p.10*
ε_ν	optical molar attenuation coefficient of the cuvette material ν	$\text{m}^2\,\text{mol}^{-1}$	*p.133*
ε_φ	optical molar attenuation coefficient of the phase φ (octanol or water)	$\text{m}^2\,\text{mol}^{-1}$	*p.133*
$\varepsilon_{\text{cbmp}}$	optical molar attenuation coefficient of carbon black microparticles (cbmp)	$\text{m}^2\,\text{mol}^{-1}$	*p.133*
γ	polytropic index for adiabatic reversible thermodynamic processes, equal to the ratio of specific heats $\gamma = \frac{c_P}{c_V}$ (for the gas and vapour in a bubble)	1.4	*p.15*

l_0	optical path length through the cuvette	m	*p.133*
M_x	molar mass of a substance "x"	$\mathrm{kg\,mol^{-1}}$	*p.133*
p_0	ambient atmospheric pressure (the value provided defines the standard pressure in NTP)	101.325 kPa	*p.13*
π	circle constant, ratio of circumference to diameter	3.1415	*p.15*
p_v	vapour pressure (of water in bubble)	1 kPa	*p.14*
$\mathcal{R}$	gas constant	$8.314\,\mathrm{JK^{-1}\,mol^{-1}}$	*p.186*
ρ_x	mass density of a substance "x"	$\mathrm{kg\,m^{-3}}$	*p.133*
ρ_{wat}	fluid mass density of water at NTP	$998\,\mathrm{kg\,m^{-3}}$	*p.14*
$\rho_{\mathrm{mol}x}$	molar density, equal to the mass density ρ_x divided by the molar mass M_x of a substance "x"	$\mathrm{mol\,m^{-3}}$	*p.133*
$\rho_{\mathrm{mol}\nu}$	molar density of the cuvette material ν	$\mathrm{mol\,m^{-3}}$	*p.133*
$\rho_{\mathrm{mol}\varphi}$	molar density of the phase φ (octanol or water)	$\mathrm{mol\,m^{-3}}$	*p.133*
$R_\theta {R_0}^{-1}$	Blake cavitation threshold ratio	≈ 2	*p.17*
ς	surface tension (of a water-air interface at NTP)	$0.072\,\mathrm{N\,m^{-1}}$	*p.14*
Υ_x	molar volume of a species "x"	$\mathrm{m^3\,mol^{-1}}$	*p.186*
χ	the effective optical path thickness of a cuvette	m	*p.133*

Variables

A	optical molar absorptivity		*p.10*
$A^{\varphi}_{\mathrm{cbmp}}$	optical molar absorptivity of carbon black microparticles (cbmp) in the φ phase (octanol or water)		*p.133*
$A^{\varphi}_{\mathrm{cbmp_{eff}}}$	total optical absorbance due to the multicomponent, multilayered sample, i.e. cuvette, phase and carbon black microparticles		*p.134*
$\mathcal{A}$	surface area	$\mathrm{m^2}$	*p.192*
$\mathcal{A}_x$	circle area with radius "x"	$\mathrm{m^2}$	*p.198*
$\mathfrak{a}_x$	chemical activity of a species "x", equal to the product of the Henrian activity coefficient and volume fraction of x in the solution, $a_x = h_x \psi_x$		*p.186*
a_f	linear regression y-intercept for the partition coefficient's average frequency effect $\log_{10}\{P(f)_p\}$ (variable frequency, constant pressure contours)		*p.33*
a_p	linear regression y-intercept for the partition coefficient's average pressure effect $\log_{10}\{P(p)_f\}$ (variable pressure, constant frequency contours)		*p.33*

b_f	linear regression gradient for the partition coefficient's average frequency effect $\log_{10}\{P(f)_p\}$ (variable frequency, constant pressure contours)	MHz^{-1}	*p.33*
b_p	linear regression gradient for the partition coefficient's average pressure effect $\log_{10}\{P(p)_f\}$ (variable pressure, constant frequency contours)	kPa^{-1}	*p.33*
$C_A(f)$	preamplifier capacitance (frequency dependent 1–20 MHz)	≈5.9 pF	*p.25*
$C_H(f)$	hydraphone capacitance (frequency dependent 1–20 MHz)	≈7.4 pF	*p.25*
c_x	concentration of the substance "x"	$\mathrm{mol\,m}^{-3}$	*p.10*
c_x^{oct}	concentration of test species "x" in octanol	$\mathrm{mol\,m}^{-3}$	*p.8*
c_x^{wat}	concentration of test species "x" in water	$\mathrm{mol\,m}^{-3}$	*p.8*
$c_{\mathrm{cbmp}}^{\varphi}$	concentration of carbon black microparticles (cbmp) in the φ phase (octanol or water)	$\mathrm{mol\,m}^{-3}$	*p.133*
$c_{\mathrm{cbmp}}^{\mathrm{oct}}$	concentration of carbon black microparticles (cbmp) in octanol	$\mathrm{mol\,m}^{-3}$	*p.134*
$c_{\mathrm{cbmp}}^{\mathrm{wat}}$	concentration of carbon black microparticles (cbmp) in water	$\mathrm{mol\,m}^{-3}$	*p.134*
D	ultrasound duty cycle		*p.13*
f_0	resonant frequency of a bubble/antibubble	Hz	*p.15*
f_c	ultrasound centre frequency	Hz	*p.13*
f	ultrasound frequency (an experimental controlled variable, used interchangeably with f_c)	MHz	*p.32*
$G(f)$	preamplifier gain factor (frequency dependent 1–20 MHz)	≈10	*p.25*
h_x	Henrian activity coefficient of species "x"		*p.186*
I_0	incident light intensity	$\mathrm{W\,m}^{-2}$	*p.10*
I	transmitted light intensity	$\mathrm{W\,m}^{-2}$	*p.10*
$I_{\mathrm{eff\,oct}}$	effective transmitted light intensities of the cuvette and octanol phase	$\mathrm{W\,m}^{-2}$	*p.134*
$I_{\mathrm{eff}\,\varphi}$	effective transmitted light intensity (component), passing through the cuvette and phase φ (octanol or water)		*p.134*
$I_{\mathrm{eff\,wat}}$	effective transmitted light intensities of the cuvette and water phase	$\mathrm{W\,m}^{-2}$	*p.134*

$I^{\varphi}_{\mathrm{cbmp_{eff}}}$	effective transmitted light intensity, passing through the cuvette, phase φ (octanol or water) and carbon black microparticles (cbmp)	$\mathrm{W\,m^{-2}}$	*p.134*
$I^{\mathrm{oct}}_{\mathrm{cbmp_{eff}}}$	total multicomponent transmitted light intensity due to the cuvette, octanol phase and carbon black microparticles (cbmp)	$\mathrm{W\,m^{-2}}$	*p.32*
$I^{\mathrm{oct}}_{\mathrm{cbmp_{eff}}}$	total multicomponent transmitted light intensity due to the cuvette, octanol phase and carbon black microparticles (cbmp)	$\mathrm{W\,m^{-2}}$	*p.134*
$I^{\mathrm{wat}}_{\mathrm{cbmp_{eff}}}$	total multicomponent transmitted light intensity due to the cuvette, water phase and carbon black microparticles (cbmp)	$\mathrm{W\,m^{-2}}$	*p.32*
$I^{\mathrm{wat}}_{\mathrm{cbmp_{eff}}}$	total multicomponent transmitted light intensity due to the cuvette, water phase and carbon black microparticles (cbmp)	$\mathrm{W\,m^{-2}}$	*p.134*
$I_{\mathrm{eff_{oct}}}$	effective transmitted light intensities of the cuvette and octanol phase	$\mathrm{W\,m^{-2}}$	*p.32*
$I_{\mathrm{eff_{wat}}}$	effective transmitted light intensities of the cuvette and water phase	$\mathrm{W\,m^{-2}}$	*p.32*
l	optical path length	m	*p.10*
$\dot{m}_x$	mass flow rate at position "x"	$\mathrm{kgs^{-1}}$	*p.198*
$M_{eoc}(f)$	hydrophone End-of-cable Open Circuit sensitivity (frequency dependent 1–20 MHz)	$\mathrm{nV\,Pa^{-1}}$	*p.25*
$M_L(f)$	loaded hydrophone-preamplifier system sensitivity (frequency dependent 1–20 MHz)	$\mathrm{nV\,Pa^{-1}}$	*p.25*
μ_x	chemical potential of a species "x" in a solution	$\mathrm{Jmol^{-1}}$	*p.186*
μ^0_x	chemical potential of a pure species "x"	$\mathrm{Jmol^{-1}}$	*p.186*
P	partition ratio, defined as $P = \dfrac{{c_x}^{\mathrm{oct}}}{{c_x}^{\mathrm{wat}}}$		*p.8*
$P(f,p)$	experimental point's partition ratio (at a specific experimental acoustic frequency and pressure)		*p.32*
$P(f)_p$	partition ratio as an average function of acoustic frequency, for any given constant acoustic pressure contour		*p.33*
$P(p)_f$	partition ratio as an average function of acoustic pressure, for any given constant acoustic frequency contour		*p.33*
$\log_{10}(P)$	partition coefficient (decade logarithm form of P)		*p.9*

$\log_{10}\{P_{\text{null}}\}$	Partition coefficient of the null samples (mean and standard deviation)		*p.34*
$\log_{10}\{P(f,p)\}$	sample's partition coefficient (at a specific experimental acoustic frequency and pressure)		*p.32*
$\log_{10}\{P(f)_p\}$	average partition coefficient as an average function of acoustic frequency, for any constant acoustic pressure contour		*p.33*
$\log_{10}\{P(p)_f\}$	average partition coefficient as an average function of acoustic pressure, for any constant acoustic frequency contour		*p.33*
$\overline{\log_{10}\{P_{\text{null}}\}}$	mean partition coefficents of the null samples		*p.34*
$\overline{\log_{10}\{P(f,p)\}}$	experimental point's mean partition coefficient (at a specific experimental acoustic frequency and pressure)		*p.32*
$\overline{\log_{10}\{P_{f,p}\}}$	partition coefficient mean of entire experimental set		*p.32*
ΔP	pressure difference across an surface interface	Pa	*p.192*
p_g	gas partial pressure (inside a bubble)	Pa	*p.197*
p_L	pressure at the liquid interface of a bubble	Pa	*p.197*
p^-	peak negative pressure	kPa	*p.13*
p^+	peak positive pressure	kPa	*p.13*
ψ_x	volume fraction of a species "x", equal to the product of the concentration and molar volume, $\psi_x = c_x V_x$		*p.186*
$p(t)$	externally forced pressure signal	kPa	*p.15*
p	ultrasound pressure amplitude (an experimental controlled variable)	kPa	*p.32*
r	radius (at point "r")	m	*p.198*
$\dot{r}$	radial velocity (at point "r")	ms^{-1}	*p.198*
R_x	principal radius of curvature in direction "x" on a surface	m	*p.192*
R_0	equilibrium bubble radius	m	*p.14*
R_c	incompressible core radius of an antibubble	m	*p.14*
R	instantaneous bubble radius	m	*p.14*
$\dot{R}$	instantaneous bubble radial velocity	m s^{-1}	*p.14*
$\ddot{R}$	instantaneous bubble radial acceleration	m s^{-2}	*p.14*
R_{f_0}	associated resonant frequency radius of a bubble with a resonant frequency of f_0	m	*p.201*
R_θ	Blake cavitation threshold radius	m	*p.17*
σ	standard deviation		*p.32*

σ_{null}	standard deviation of the null sample's partition coefficients		*p.34*
$\sigma_{\log_{10}\{P(f,p)\}}$	experimental points' partition coefficient standard deviation (at a specific experimental acoustic frequency and pressure)		*p.32*
$\sigma_{\log_{10}\{P_{f,p}\}}$	partition coefficient's standard deviation of the entire experimental set		*p.32*
σ_s	standard deviation of the sample's partition coefficients (equivalent to $\sigma_{\log_{10}\{P_{f,p}\}}$)		*p.33*
S	circumference (generally the surface perimeter)	m	*p.195*
Θ	Temperature	K	*p.186*
θ	contact angle		*p.191*
T_{off}	ultrasound pulse off-time	s	*p.13*
T_{on}	ultrasound pulse on-time	s	*p.13*
T_{PRT}	ultrasound pulse repetition time	s	*p.13*
v	velocity	ms^{-1}	*p.199*
$\dot{V}_x$	volume flow rate at position "x"	$\text{m}^3\,\text{s}^{-1}$	*p.198*
W	work, energy (surface energy)	J	*p.192*
K_E	kinetic energy	J	*p.199*

Other

gs	gas-solid interface		*p.191*
lg	liquid-gas interface		*p.191*
sl	solid-liquid interface		*p.191*
ν	cuvette material phase		*p.133*
null	null samples, used to indicate a variable/statistical property of all the null samples		*p.34*
φ	phase material, consisting of either a solid, liquid, gas, or even a specific substance (such as octanol or water)		*p.133*
s	samples, used for σ_s to indicate the standard deviation of all the *samples* in the expereimental set		*p.33*

Symbol	**Description**	**Value/Units**	**See**

List of Abbreviations and Acronyms

2D	two-dimensional	141
3D	three-dimensional	xxi, 22, 39, 140
4D	four-dimensional	141, 150
cbmp	carbon black microparticles	xv–xviii, 27, 132–135
csv	comma-separated values file format	94
DIP	digital image processing	5, 19, 39, 87, 132, 137, 211
EOC	End-of-cable Open Circuit	xviii, 25
FFT	fast Fourier Transform	94
NIST	National Institute of Standards and Technology	xxi
NTP	normal temperature and pressure (defined as 293.15 K(20 °C) and 101.325 kPa by the NIST)	xvi, 15, 204
PLA	polylactic acid or polylactide, a plastic polymer commonly used in 3D printing	22
png	portable network graphics file format	139

RGB	red-green-blue	11, 150
ROI	region of interest	29, 132, 137, 211
USB	universal serial bus	29

Chapter 1

Introduction

Microparticles have emerging applications in the medical field and in biomedical engineering in general. Hydrophobic microparticles are acoustically active. Moreover, these hydrophobic microparticles can be used as ultrasound contrast agents to enhance ultrasound imaging. Additionally, acoustically active microparticles have potential use in ultrasound-guided drug delivery [1–3]. More generally, microparticles have a broadening use in drug delivery in general. These microparticles' pharmacokinetics is critical to their safe medical use. One of the crucial factors in pharmacokinetics is a drug's hydrophobicity. The hydrophobicity of a drug ultimately determines the biological compartment and metabolic path the drug will take.

More recent observations have pointed to the impact of tattoos on ultrasound imaging. Tattoos typically use microparticles as their pigments, the most common of which is hydrophobic carbon black. With many emerging uses of microparticles in general, and specifically hydrophobic microparticles in conjunction with ultrasound, the effect of ultrasound on microparticle hydrophobicity needs to be fully understood.

1.1 Problem statement

Previous research has indicated that carbon black microparticles are acoustically active. More recent observations qualitatively indicate that ultrasound affects the hydrophobicity of carbon black microparticles. Currently, no quantitative description relating ultrasound regime parameters to the hydrophobicity of microparticles exists. This is both a problem and an opportunity. The lack of a quantitative description of ultrasound's effect on microparticle hydrophobicity means that its use under ultrasound exposure is not fully understood. This can lead to as yet unknown potential side effects in medical settings, even though the acoustic activity of microparticles has been previously researched and quantified. The potential side effects are of particular concern with the widening use of microparticles in medical applications in general. This presents a clear and critical lack of knowledge base. This also presents an opportunity to use ultrasound with hydrophobic microparticles safely, and potentially further utilise these effects. There is also a potential to broaden this knowledge base to other industrial applications if this effect is quantified.

1.2 Research question

To what extent does ultrasound quantitatively change the hydrophobicity of hydrophobic microparticles?

A host of other implicit questions stem from the fundamental research question above. These implicit questions divide the research question into smaller concerns that can be addressed individually. Firstly, what is a suitable method to quantify microparticles' hydrophobicity? Is there a statistically significant difference in the measured hydrophobicity of microparticles exposed to ultrasound compared to those not? What are the ultrasound parameters that may induce this change? What is the mathematical relationship between the quantified difference of hydrophobicity and the different ultrasound parameters? Is the change static or dynamic?

These implicit questions are tied to developing the foundation of the quantified effect, and will ultimately answer the research question itself. Therefore, the research is

structured to explore and answer these implicit questions. A quantitative hydrophobicity measurement method suitable for microparticles must be found and utilised. Additionally, this method must be easily deployed and repeatable. The method must then be used to measure quantitatively the hydrophobicity of unsonicated hydrophobic microparticles and hydrophobic microparticles exposed to ultrasound. Selected controlled parameters of ultrasound must be identified. Subsequently, these parameters must be individually tested against the change in hydrophobicity. Additionally, any change must be constrained to a chosen timeframe. The stability of any change in hydrophobicity must be observed over this timeframe.

This lays the foundation of the research objectives, which are presented hereafter.

1.3 Research objectives

Individual ultrasound parameters are identified for the research, specifically acoustic frequency and pressure amplitude. These chosen parameters are the basis of investigation, from which the following objectives are formulated and addressed in this dissertation:

Objective 1

Use a quantitative hydrophobicity measurement method to investigate quantitatively any effect that an ultrasonic regime's acoustic frequency has on microparticle hydrophobicity.

Objective 2

Use a quantitative hydrophobicity measurement method to investigate quantitatively any effect that an ultrasonic regime's acoustic pressure amplitude has on microparticle hydrophobicity.

Objective 3

Determine the timeframe over which any change in hydrophobicity caused by ultrasound is stable.

1.4 Outline

In this *Chapter 1*, there is a short introduction contextualising the research. The qualitative observation of ultrasound changing microparticle hydrophobicity is introduced as the starting point of this dissertation. The absence of a quantitative description of this change is identified as a lack in the body of knowledge. This shortcoming is the focus of the research, with the research question centred around this lack of foundation. The objectives are structured around investigating specific aspects of ultrasound's effect on microparticle hydrophobicity.

In *Chapter 2*, the background knowledge is explored. A definition of microparticles is provided and explored. This is used to constrain the remaining background knowledge in the context of the known knowledge on microparticles. A definition of hydrophobicity is provided thereafter. A method of quantifying hydrophobicity for microparticles is explored directly from the definition of hydrophobicity. Ultrasound is then defined, and various parameters thereof are identified. These parameters are specific to quantifiable signal characteristics of ultrasound, such as frequency, amplitude, and duty cycle. The known effects of ultrasound on hydrophobic microparticles are also explored. Additionally, the specific observation of ultrasound affecting microparticle hydrophobicity is discussed as a starting point of this research Lastly, colourimetry is discussed as an auxiliary but necessary concept for measuring the concentration of a substance in a solution using optical phenomena. Colourimetry is tied to the quantitative methods of measuring hydrophobicity used in the methodology.

The Materials and methods *Chapter 3* follows from the background. The experimental setup is described in four conceptual categories. These are; ultrasound generation, its associated ultrasound measurement, microparticle preparation and processing, and imaging and image processing. These categories are structured according to the methodological process and flow of the experiments. Focus on the ultrasound generation and measurement equipment is then discussed, as this primarily limits the scope of the ultrasound parameters in the research. The microparticle samples' preparation is then provided. Hydrophobic carbon black microparticles from tattoo ink are used as the scope of microparticle materials investigated. The procedure of ultrasound exposure and post-exposure

preparation for the samples' hydrophobicity measurement is discussed. The imaging setup and its associated purpose using colourimetry for measuring the concentration of a solution is discussed. This is tied to the actual hydrophobicity measurement and quantification. Finally, the digital image processing (DIP) algorithm for numerically quantifying the hydrophobicity of an imaged sample is briefly discussed.

Following this are the results in *Chapter 4*. Firstly, the ultrasound transducer measurements and technical characteristics are presented. This characterises the ultrasound signal(s) that is used to sonicate the exposed hydrophobic microparticles. This simultaneously defines, provides and verifies the scope of the ultrasound parameters used. Following this, the experimental results are presented. The experimental results are divided into the samples' respective imaged times. These times correspond to and are laid out in the methodology.

The next *Chapter 5* discusses the results in Chapter 4. Here the results are unpacked in more detail. The phenomena that are observed in the results chapter are critiqued. As quantified in the results, the underlying effects of the ultrasound parameters on microparticle hydrophobicity are discussed in relation to the known acoustic behaviour. An argument on the causality and relationship of the observed changes and how they relate specifically to the acoustic behaviour of microparticles is discussed.

Chapter 6 concludes the research with the important core findings. The starting point of the research is restated, along with the missing body of knowledge that this research seeks to complete. The research question is affirmed, and the nuances of the results are briefly restated.

Chapter 2

Background

2.1 Overview

In this chapter, the necessary knowledge and literature review are covered. The phenomenon of ultrasound qualitatively affecting the hydrophobicity of microparticles has been previously observed. In order to explore this phenomenon and ultimately quantify it, as is the objective of this research, the existing knowledge and topics involved need to be understood. Since no previous work has quantified this effect, the onus of this research is to substantiate the quantified results. This research is highly dependent on the definitions of the underlying topics.

A microparticle's definition is provided since microparticles are a central component of the research. This is essential as it could impact how hydrophobicity is meaningfully and experimentally measured. Thereafter, the definition(s) of hydrophobicity is provided. The definition of hydrophobicity is intimately linked with how it is quantitatively measured, Thus the definition also prescribes the methodology. Ultimately the definition used is the octanol partitioning coefficient, a chemical thermodynamic definition. The coefficient requires the measurement of concentrations of the test material in two solvents. The measurement is dependent on the measured concentrations. The practical issue is then measuring these concentrations.

Colourimetry is covered, which is a method of non-invasively measuring the concentration of solutes or suspended particles in a solution. This is an auxiliary topic but necessary for the research. A literature review on the principle of colourimetry is provided, emphasising the practicality and accuracy of low-cost setups.

Lastly, is a discussion on ultrasound since ultrasound, as a pressure on the underlying thermodynamic phenomenon, ultimately drives the possible change in hydrophobicity observed. Therefore the characteristics of ultrasound are first discussed. The qualitative observation of ultrasound affecting hydrophobic microparticle hydrophobicity is covered. This is the primary motivation of this research. A brief discussion on the known acoustic behaviour of such hydrophobic microparticles follows.

2.2 Microparticles

Microparticles are particles that are defined as physically distinct material from their surroundings with dimensions from 0.1 µm to 1000 µm [4, 5]. The lower end of this range is distinguished from nanoparticles, 1 nm to 100 nm [5]. Microparticles range in shapes, such as microspheres and microrods, and can range in structural types, such as pure microparticles and microcapsules [4, 5]. Microcapsules are microparticles with multi-layer materials [4, 5]. Manufactured ultrasound contrast agents are considered microcapsules, a gaseous microparticle with a re-enforcing pliable shell [6]. Microparticles can consist of hydrophobic materials. The hydrophobic nature of microparticles is characterised by an interconnected network of nanobubbles on the microparticle surface when submerged in water [7]. Now that microparticles have been defined, the hydrophobicity of microparticles needs to be understood. Hydrophobicity is explored in the following section.

2.3 Hydrophobicity

Hydrophobicity is qualitatively described as the ability of a material to repel water [8, 9]. Classically, hydrophobicity is quantified through the contact angle [10, 11]. The contact angle definition of hydrophobicity is a surface thermodynamic balance phenomenon. The method would require the measurement of the three-phase interface angle on a specific microparticle, in water, while it is freely mobile and exposed to ultrasound (which can spatially translate it, as is covered later in Section 2.5). Therefore, the contact angle definition is practically useless for this research. However, it is related to bubble dynamics, and the contact angle is covered in Appendix F for further detail. Another qualitative description is extended from the concept of polar and non-polar molecular groups [8]. The chemical thermodynamic phenomenon of polar and nonpolar molecular groups of materials results in another quantitative description of hydrophobicity, the partition coefficient [8, 12].

Hydrophobic materials are generally nonpolar molecules and will dissolve or disperse easily in a nonpolar liquid solvent [8, 9, 12]. Hydrophilic materials are generally polar molecules and dissolve or disperse easily in a polar liquid solvents [8, 9, 12]. 1-Octanol is a nonpolar solvent consisting of long hydrocarbon molecules [12]. It has eight carbons with a terminating hydroxyl OH group [8, 12]. Water is a polar solvent consisting of one oxygen and two hydrogens in an angled bond [8, 9, 12].

Water and octanol are immiscible solvents [12]. If a test species is introduced to this octanol-water volume, it will dissolve or disperse more easily in one of the solvents [12]. However, it will reach a thermodynamic equilibrium concentration in each solvent [12]. The octanol-water partition coefficient is defined as the unitless ratio of the concentration of the test species in octanol to that of water

$$P = \frac{{c_x}^{\text{oct}}}{{c_x}^{\text{wat}}} \tag{2.1}$$

where, P is the partition ratio; c_x is the concentration of the test species; and superscripts denoting the particular liquid phase (solvent) of the concentration [12].

The concentration in one phase is often significantly higher than in the other, and the ratio spans several orders of magnitude. It is therefore common to represent the value in

a decade log form

$$\Rightarrow \log_{10}(P) = log\left(\frac{{c_x}^{\text{oct}}}{{c_x}^{\text{wat}}}\right) \tag{2.2}$$

where the variables are as explained above for Equation 2.1 [12]. This $\log_{10}(P)$ form of the definition of the partition coefficient will be used in this document moving forward, except where explicitly stated otherwise.

Hydrophilic materials are defined as having a partition coefficient <0, while hydrophobic materials are defined as having a partition coefficient >0 [8]. It is evident that the method requires the concentrations to be measured accurately for each solvent. However, by the conservation of mass and the principle of mass transfer, the coefficient can be calculated by measuring the final concentration in only one phase [12]. This requires the initial concentration to be known prior to partitioning.

The partition coefficient is determined through various techniques. The techniques are either direct methods which measure the concentration directly [12]; or indirect methods which infer the coefficient through other chemical thermodynamic phenomena that do not measure the concentration at all [12]. The simplest direct method is the shake-flask method which directly uses the partitioning phenomenon [12].

The shake-flask method is briefly described as follows. A substance is introduced to an octanol-water volume. The volume is shaken to emulsify the phases, effectively increasing the surface area of the octanol-water interface and speeding up the partitioning process. The mixture is rested to allow the octanol and water to separate again. A sample of each phase is taken, and the concentration of the substance in the particular phase is measured. The coefficient is then calculated as per Equation 2.2. Appendix E covers the details of partitioning as a chemical thermodynamic balance process.

The principle of the shake-flask method is easily understood and accessible as a method. The method is also intimately linked to the definition of hydrophobicity. In the context of microparticles, the method doesn't concern itself with an individual microparticle, but tests all microparticles in a bulk dispersion. The practicality of this defining method is only limited by how the concentration is measured. Ideally, this method should be as non-intrusive as possible in order to not contaminate the phases by mixing, thereby disturbing

the equilibrium and introducing error. Such a method of non-intrusive concentration measurement is colourimetry; this is discussed next.

2.4 Colourimetry

Colourimetry is a method of measuring a solution's concentration by its optical absorbance properties. It uses the fundamental property of the optical density of materials. The intensity of light transmitted through an optical medium is given by the Intensity Absorbance [13],

$$I = I_0 e^{-A} \tag{2.3}$$

where, I is the transmitted light intensity; I_0 is the incident light intensity; and A is the optical molar absorptivity. Absorbance is determined further by the various properties of the optical medium. The optical absorbance is defined by the Beer-Lambert Law below [13].

$$A = \varepsilon c_x l \tag{2.4}$$

where, ε is the optical molar attenuation coefficient (of the substance "x"); c_x is the concentration of the substance "x"; and l is the optical path length through the solution. Thus

$$\ln\left(\frac{I_0}{I}\right) = -A = -\varepsilon c_x l \tag{2.5}$$

For a fixed optical path length and absorption coefficient, this demonstrates that concentration is linearly dependent on the natural logarithm of the intensity ratio.

Consider a colourimetric sample set, in which the samples range in concentration, ideally from zero to saturation. Then measuring the intensity of transmitted light at a particular wavelength and dividing by the intensity measurement of the zero concentration and finding the natural log of this gives the absorption values. Plotting the absorption against the concentrations produces a linear calibration curve. The units of intensity and concentration are arbitrary at this point. The intensity can be measured for an unknown sample, and the absorbance can be calculated appropriately with the zero concentration intensity as a reference. Finally, the concentration can be inferred from the calibration curve.

2.4.1 Review of Colourimetry

Various work has been done on the applications of colourimetry with the exploration of image processing methods and colour analysis to enhance the practicality. This is briefly reviewed.

In previous work, the use of digital imaging to measure the concentration of yellow food colouring in water was investigated [14]. Yellow food colouring was analysed with a spectrophotometer and had the highest absorbance at approximately 440 nm. This wavelength corresponds to the colour blue, the complementary colour of the yellow food colouring. Five reference samples 0 to 100% in steps of 25% of a stock solution were imaged with a digital camera. The light intensity was adjusted so that the 0% reference image was unsaturated, with the digital value <255. The blue channel was used for absorbance analysis, and a linear correlation of R^2=0.9994 was found.

Recently, the ColorX digital image processing software for colourimetry measurement was designed [15]. Five reference samples for each of four different soluble salts are investigated. These salts have different colours in solution. Here the average red-green-blue (RGB) value was calculated from the digital image, and a calibration curve was generated. Another sample is then tested as an unknown to evaluate the ColorX software. The linearity was excellent, with most having R^2>0.999 and the worst R^2>0.98.

Other research tested the implementation of colourimetry using a smartphone camera [16]. A smartphone was used for digital imaging and digital image processing for each Red-Green-Blue channel. This was compared to a standard ultraviolet-visible spectrophotometer with successful results. Here the correlation was found to be R>0.98. Colourimetry shows excellent measurement performance in measuring concentrations of solutions, usually with linearity correlation coefficients R^2>0.998.

The application has also been extended from colourimetry of soluble substances to insoluble suspended particles. Turbidity is the measure of the relative clarity of water [17, 18]. It specifically is a water quality metric describing the clarity of water dependent on insoluble suspended particles [17, 18]. Turbidimetry is the measurement of turbidity using the principles of colourimetry [19]. Similar work implementing colourimetry measurement

systems using custom photometry and digital imaging has shown excellent results [19, 20]. Most of the linearitiy correlation coefficients are R^2>0.995 [19, 20]. Absorbance, light intensity and frequency of light have been investigated in turbidimetry [21]. It was found that larger frequencies were more sensitive and provided the largest dynamic range in turbidimetry [21]. Turbidimetry is a specific application of colourimetry as a baseline for quantifying the number/concentration of particles in water. It can be used in a general sense, i.e. where water's relative clarity is important, but the particulate materials' composition(s) is not important.

2.5 Ultrasound

The research requires the use of ultrasound and its exposure to hydrophobic microparticles. Fundamental background and definitions of microparticles, hydrophobicity as defined and quantified by the partition coefficient, and colourimetry as a method of quantifying solution concentration, has been covered above. The last component necessary to cover is the concepts behind ultrasound. Firstly, ultrasound and its signal properties are appropriately defined. Following this, the existing acoustic behaviour of microparticles is briefly discussed. Lastly, a review of the existing (qualitative) effect of ultrasound on hydrophobic microparticles is covered

Ultrasound is characterised as an acoustic pressure wave propagating in a physical medium with a frequency >20 kHz [6, 22–24]. A piezoelectric transducer is typically used to produce ultrasound, which transduces electrical and acoustic signals [6, 22–24]. An ultrasonic signal is characterised by its centre frequency f_c, peak negative p^- and positive p^+ pressures above and below the ambient pressure p_0, and pulse on-time T_{on} with the associated off-time T_{off} [22]. The centre frequency is the transmitted frequency of the transducer when energised for the duration of the on-time [22]. The duty cycle is the percentage of the transmission on time to that of the pulse-repetition-time $D = \frac{T_{on}}{T_{PRT}}$ [22]. The amplitude of the acoustic signal is given by the peak positive and negative pressure [22]. Figure 2.1 indicates the above ultrasound parameters on an example ultrasound signal.

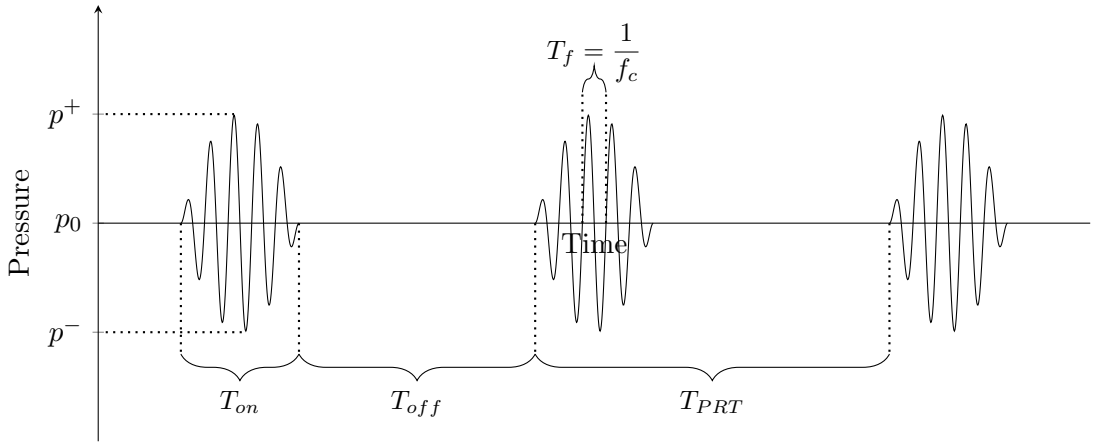

Figure 2.1: Generalised ultrasound signal

2.5.1 Acoustic properties of bubbles

Microbubbles are acoustically active in the ultrasonic range [1, 6, 24–27]. Ultrasound is described as a pressure-changing signal, as discussed above. The Rayleigh-Plesset equation describes the dynamics of microbubbles and how ultrasound as a time-varying pressure signal affects these dynamics [6, 25–27]. Hydrophobic microparticles suspended in water can be modelled as antibubbles, microbubbles with an incompressible core [6, 26, 27]. Since they are fundamentally bubbles, hydrophobic microparticles are also similarly acoustically active. However, the dynamics are slightly modfied to accommodatefor the incompressible core [6, 26, 27]. The modified Rayleigh-Plesset equation for spherical hydrophobic microparticles (as antibubbles) is [27],

$$\frac{3}{2}\dot{R}^2 + R\ddot{R} = \frac{1}{\rho}\left[\left(p_0 - p_v + \frac{2\varsigma R_0}{{R_0}^2 - {R_c}^2}\right)\left(\frac{R_0^3 - R_c^3}{R^3 - R_c^3}\right)^{\gamma} + p_v - \frac{2\varsigma R}{R^2 - {R_c}^2} - p_0 - p(t)\right] \tag{2.6}$$

where, R_0 is the equilibrium bubble radius; R is the instantaneous bubble radius; $\dot{R}$ is the first time-derivative of R, and is the instantaneous bubble radial velocity; $\ddot{R}$ is the second time derivative of R, and is the instantaneous bubble radial acceleration; ρ is the fluid mass density of the surrounding fluid, water in this case with ρ_{wat} =998 kg m^{-3}; p_0 is the ambient pressure; p_v is the vapour pressure of the liquid's vapour in the bubble; ς is the surface tension of the liquid gas interface, for a water-air interface, ς =0.072 N m^{-1}≡ J m^{-2}; R_c is the incompressible core radius of an antibubble; γ is the

polytropic index (for adiabatic reversible thermodynamic processes), assumed to be $\gamma = \frac{c_P}{c_V}$ =1.4 for the bubble gas and vapour; $p(t)$ is the externally forced pressure signal (from an ultrasound transducer). The specified values are all at normal temperature and pressure (NTP), defined as 293.15 K(20 °C) and 101.325 kPa.

The hydrophobic microparticle has a resultant resonant frequency that is derived from the linearised Rayleigh-Plesset equation [27]. The equation is,

$$f_0 = \frac{1}{2\pi R_0\sqrt{\rho}}\sqrt{\left(3\gamma\left(\frac{p_0 - p_v + \frac{2\varsigma R_0}{{R_0}^2 - {R_c}^2}}{1 - \left(\frac{R_c}{R_0}\right)^3}\right) - \frac{2\varsigma R_0}{{R_0}^2 - {R_c}^2}\right)} \tag{2.7}$$

with the symbols as explained above. A hydrophobic microparticle can be exposed to an acoustic frequency that is higher than or lower than its resonance. The bubble is said to be exposed to a quasi-isostatic driving pressure if the acoustic frequency is lower than the resonance frequency I.e. the wavelength is larger than the particle, and the driving pressure is locally uniform around the particle [26, 27].

Hydrophobic microparticles as antibubbles translate in an acoustic field depending on the acoustic frequency and their resonant frequency [6, 25, 26]. Suppose the wavelength is larger than the particle. In that case, primary radiation forces drive the particle to the anti-nodes of a standing ultrasound wave, or the acoustic focus of a propagating acoustic wave [6, 25, 26]. The acoustic focus and the antinodes in a standing wave are regions with the largest dynamic pressure variations in an acoustic field [6, 25, 26]. Suppose the wavelength is smaller than the particle. Then the primary radiation forces drive the particle to the nodes in a standing wave or away from the acoustic focus of the ultrasound signal [6, 25, 26]. These are regions of the lowest dynamic pressure [6, 25, 26]. Secondary radiation forces also occur, which originate from the bubbles re-radiating their own acoustic field [6, 26]. Bubbles that radiate in phase attract one another and repel if they are out of phase [6, 26]. The dynamics of bubbles, their acoustic behaviour and their behaviour relative to their resonant frequency are detailed further in Appendix G.

2.5.2 Ultrasound affecting hydrophobicity

Recently, two types of hydrophobic microparticles were observed while exposed to ultrasound [28]. The microparticles were <10 µm in diameter. The setup consisted of an inverted light microscope with a high-speed camera fixed to the objective lens. Samples were either pre-exposed to an ultrasound bath with a centre frequency of 45 kHz, or shaken by hand. Thereafter the sample was observed under the microscope whilst exposed to a 1 MHz, 0.2 MPa acoustic regime.

One of the hydrophobic microparticle materials investigated, carbon black, exhibited different behaviour depending on if it was pre-treated in the ultrasound bath. Samples that were pre-exposed to ultrasound lost their gaseous shells after one ultrasonic cycle [28]. Other samples of carbon black microparticles that were only shaken by hand retained their gaseous shell and remained acoustically active [28]. The other hydrophobic microparticle material that was investigated, zinc oxide, exhibited no changes and remained acoustically active regardless of being shaken by hand or pre-exposed to ultrasound [28].

More recently, the acoustic and physically related properties of hydrophobic carbon black suspension from Zuper Black pigment dispersion (INTENZE Products, Inc., Rochelle Park, NJ, USA) was quantified [26, 27]. The hydrophobic carbon black microparticle size was measured using atomic force microscopy and compared to the void size when suspended in water [26]. The antibubble void (outer) diameter was found to be 0.29 µm to 1.14 µm [26]. Importantly resultant antibubble core-to-void ratio was determined to be 0.8 [26]. More than 95% of the microparticles were 0.2 µm to 0.6 µm in size, and the rest larger [26].

The acoustic resonance and nucleation properties of hydrophobic carbon black microparticles have also been investigated [27]. Hydrophobic microparticles, as antibubbles, exhibit asymmetrical oscillation when exposed to ultrasound at low acoustic amplitudes [1, 27, 28] This asymmetric oscillation property results in a two-fold increase in the resonant frequency of a hydrophobic antibubble compared to a similarly sized ordinary bubble [27]. For the hydrophobic carbon black microparticle antibubbles (Zuper Black pigment), the resonant frequency was calculated to be >15 MHz using Equation 2.7 [27]. Specifically, for 95% of particles, the modal resonant frequency is >40 MHz [27]. Additionally, the

nucleation threshold radius of antibubbles, specifically that of hydrophobic carbon black, is significantly less than the threshold for ordinary microbubbles. The Blake cavitation threshold radius is two times the resting void radius, i.e. $R_\theta {R_0}^{-1} \approx 2.0$, for standard microbubbles [27]. In contrast, the predicted threshold for hydrophobic carbon black antibubbles of $R_\theta {R_0}^{-1} = 1.3$ was calculated [27]. Additionally, the corresponding threshold pressures for the microparticles were calculated. The resultant threshold pressures for nucleation that was calculated were 0.88 MPa and 0.3 MPa for the particle sizes 0.29 µm and 1.14 µm respectively [27]. The acoustic amplitudes investigated for the nucleation threshold were between 0.2 MPa to 1.0 MPa at 1 MHz [27]. The frequency is much less than resonant, and the particles were in a quasi-isostatic condition [27].

The antibubbles were imaged using high-speed photography during exposure. Bubbles that oscillated in phase experienced nucleation and did not renucleate after subsequent ultrasound pulses [27]. Bubbles that oscillated in anti-phase did not pass the nucleation threshold, did not nucleate and did not lose their gaseous shell [27]. Of the particles imaged, half nucleated, while half did not [27]. The exact threshold ratio was not conclusively determined [27]. However, it was determined that $R_\theta {R_0}^{-1} < 2.0$ [27]. The resultant upper bound on the threshold pressure is 0.2 MPa [27]. An antibubble cavitates and loses its gaseous void at a lower threshold radius and lower acoustic pressure compared to ordinary microbubbles [27].

The qualitative observation of ultrasound changing the hydrophobicity of carbon black microparticles has been observed, the acoustic dynamics of these have recently been investigated [1, 26–28]. The quantitative change in the hydrophobicity has not been investigated nor determined.

2.6 Summary

The fundamental definitions of a microparticle, hydrophobicity and ultrasound have been described above. The definition of microparticles provided a baseline context for an appropriate definition of microparticle hydrophobicity. A microparticle is defined to be distinct material from its surrounding that is on the order of 0.1 µm to 1000 µm in size. A suitable definition of hydrophobicity, the octanol-water partition coefficient, was

found and provided for the context of microparticle hydrophobicity. The definition also prescribes a corresponding methodology of quantification. This method requires, and is limited by, the measurement of the concentration of a test sample in each octanol and water phase. Colourimetry is a suitable noninvasive method for measuring concentrations of solutions and particle dispersions. The concept of colourimetry is based on the optical attenuation of light through a sample solution. The concentration of a sample can be inferred from a predetermined reference baseline. This method is identified as inexpensive and easily implemented, and implementable with the partitioning coefficient.

Ultrasound and the signal properties of ultrasound are defined. The known effects of ultrasound on and the acoustic properties of microbubbles, and specifically antibubbles, are discussed. The acoustic resonant frequency of an antibubble is provided in relation to its derivation from the Rayleigh-Plesset equation of bubble dynamics. The behaviour of antibubbles in an acoustic field is discussed concerning the resonant frequency in comparison with the acoustic field frequency. Bubbles exposed to a frequency such that they are in a quasi-isostatic time-varying pressure will migrate to the antinodes of acoustic focus, thereby exposed to maximal dynamic pressure changes.

The effects of ultrasound on hydrophobic carbon black (from Zuper Black pigment dispersion) have recently been investigated. These particles are between 0.2 µm to 0.6 µm in size, have a void-to-core ratio of 0.8, and a subsequent resonant frequency of 15 MHz. The particles also nucleate at a lower Blake nucleation radius threshold of $R_\theta {R_0}^{-1} = 1.3$. Thus cavitation and the loss of the gaseous shell around the carbon black particles occurs more easily at lower acoustic amplitudes. Nucleation of hydrophobic carbon black microparticles occurs after a single cycle of 0.2 MPa, 1 MHz ultrasound with no subsequent recavitation. This characterises the qualitative change in hydrophobicity of the carbon black microparticles. This change in hydrophobicity has not been quantitatively investigated.

The next chapter discusses an experimental setup designed to quantify the change in hydrophobicity of hydrophobic microparticles caused by ultrasound. This setup and subsequent methodology are based upon the partition coefficient, quantified with colourimetry, and an applicable range of ultrasound parameters.

Chapter 3

Materials and methods

3.1 Overview

Chapter 2 provided vital definitions for this research. The core of this research is to quantify the hydrophobicity of sonicated microparticles. The definition of hydrophobicity, specifically the partition coefficient, not only provides a suitable defining metric, but also prescribes the method of quantification. The method is also suitable for microparticle suspensions, which can be partitioned after the intended sonication. This chapter covers in detail how the concept of the partition coefficient, its method and sonicating microparticles, are all connected into an experimental design to quantify ultrasound's effect on microparticle hydrophobicity.

The generation and measurement of ultrasound are covered first. The generation of ultrasound is scoped to the capabilities of the available equipment. The ultrasound frequency-dependent measurement sensitivity, techniques and parameters are defined. The octanol-water partition method of quantifying hydrophobicity is described in detail in the context of these experiments. The method of processing a sample, from ultrasound exposure to partitioning, is then covered. Following this, the digital image processing (DIP) colourimetry algorithm for quantifying the partition coefficients of the samples is conceptually covered. The statistical methods and regression analysis of the results are described in the closing of this chapter. A high-level diagram of the experimental

setup can be seen in Figure 3.1. Figure 3.2 provides further diagrammatic detail on all the subsystems. The diagram shows where specific equipment is located and how they are physically and conceptually linked to one another. Further details of each subsystem and the experimental protocol are covered below. The detailed diagram in Figure 3.2 should also be considered in combination with the images of the experimental equipment and layout in Figure 3.3, Figure 3.5 and Figure 3.6.

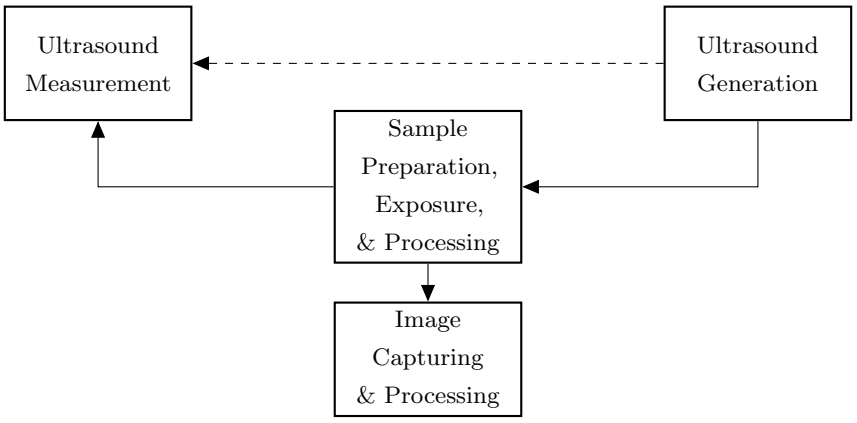

Figure 3.1: High-level block diagram of the experimental setup and procedure

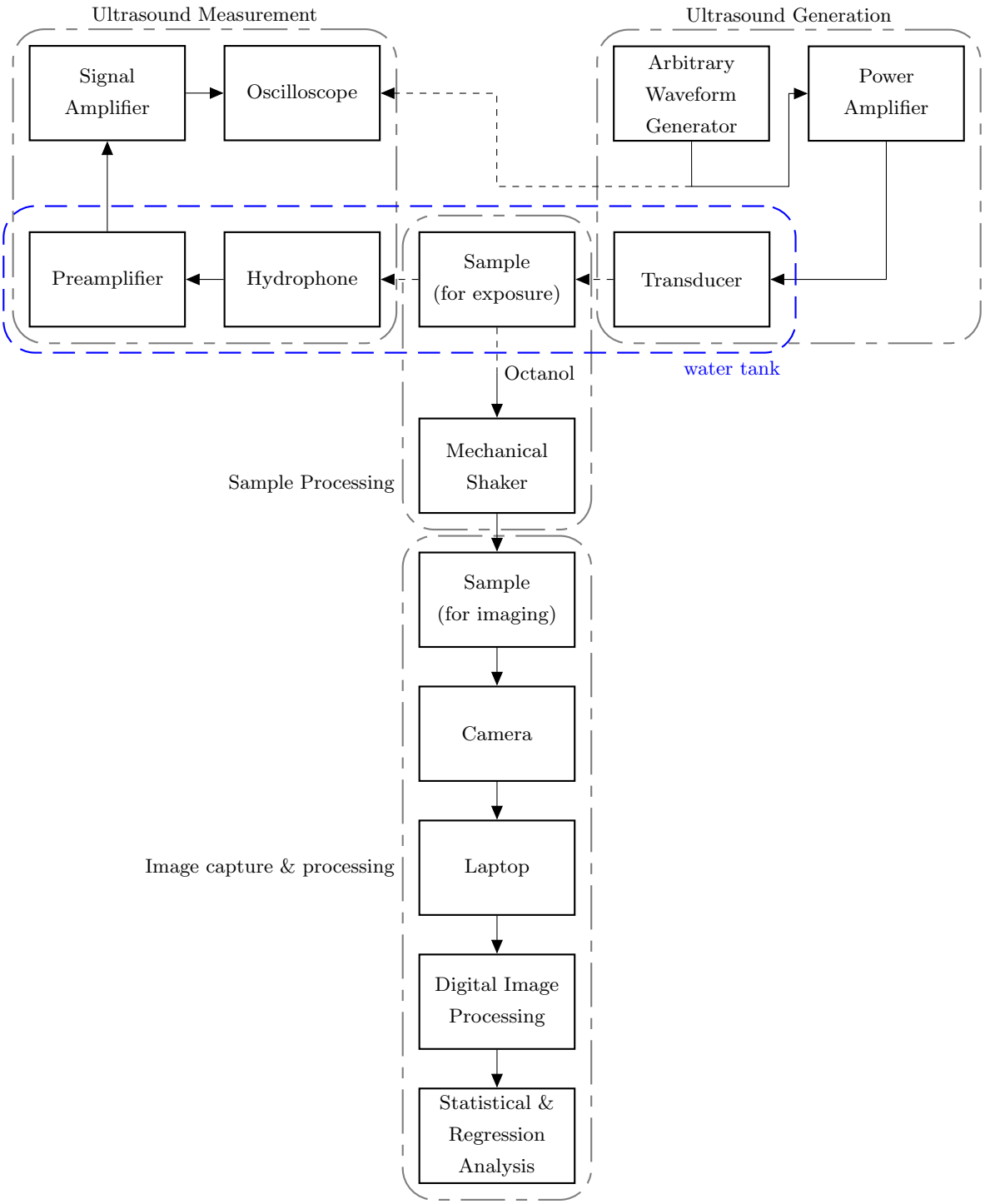

Figure 3.2: Detailed block diagram of experimental setup

3.2 Ultrasound generation and measurement setup

The following describes the *Ultrasound Generation* and *Ultrasound Measurement* subsystems as seen in Figure 3.2. These subsystems were used to simultaneously expose the microparticles and verify the regime parameters for the duration of the exposure. This verification added to the validity of the results.

The ultrasound signal was generated by the Tektronix AFG3022B Dual Channel Arbitrary Waveform Generator (Tektronix, Inc., Beaverton, OR, USA). This signal was split using an RG58 BNC T-connector at the generator output. One of the T-connector outputs was then connected to the Tektronix DPO4034 oscilloscope (Tektronix, Inc., Beaverton, OR, USA) with an RG58 BNC cable for signal verification and measurement purposes. The other part was connected to the A150 RF Power Amplifier (Precision Acoustics Ltd. (Electronics & Innovation Ltd.)) with an RG58 BNC cable to amplify the signal. The amplified signal was then connected to the custom ultrasound transducer using an RG58 BNC cable. The transducer was located in a custom-built Perspex tank (with internal dimensions: depth 65 mm; width 235 mm; length 575 mm) and held in place with a custom made three-dimensional (3D) printed transducer housing (Ultimaker polylactic acid (PLA)). The tank was filled with reverse osmosis distilled and degassed water (CJ Distribution, Midrand, South Africa). The water was degassed by allowing it to stand open to the atmosphere.

The microparticle sample contained in a cuvette was submerged in water. The submerged cuvette was placed directly in front of the transducer, which was also submerged. Here, the cuvette was exposed to the desired ultrasound regime in the tank. The cuvette was held in place with a custom-made 3D printed cuvette rack (Ultimaker PLA). Behind the sample, the Onda HGL-0200 Hydrophone (Onda Corp., California, USA) was used to measure the acoustic signal. The transducer and hydrophone were spaced 1.5 mm away from the cuvette using a glass slide (of 1.5 mm thickness).

The Onda HGL-0200 Hydrophone was connected directly to the Onda AH-2010-025 Preamplifier (Onda Corp., California, USA). The hydrophone-preamplifier was held in place with its own custom-made 3D printed hydrophone housing (Ultimaker PLA). The Preamplifier was connected with the supplied cable to the preamplifier's signal

amplifier. This signal amplifier was then connected directly to the Tektronix DPO4034 oscilloscope to complete the measurement setup. An image of the actual setup can be seen in Figure 3.3 (a £1 coin is included for scale).

The Onda AH-2010-025 Preamplifier's signal amplifier has an output impedance of 50 Ω. The A150 RF Power Amplifier has an input and output impedance of 50 Ω as well. The input impedance of the Tektronix DPO4034 oscilloscope is set to 50 Ω on both the signal generator and hydrophone input channels. The signal generator was set up to have an output impedance of 50 Ω. The RG58 BNC type cables have a 50 Ω characteristic impedance.

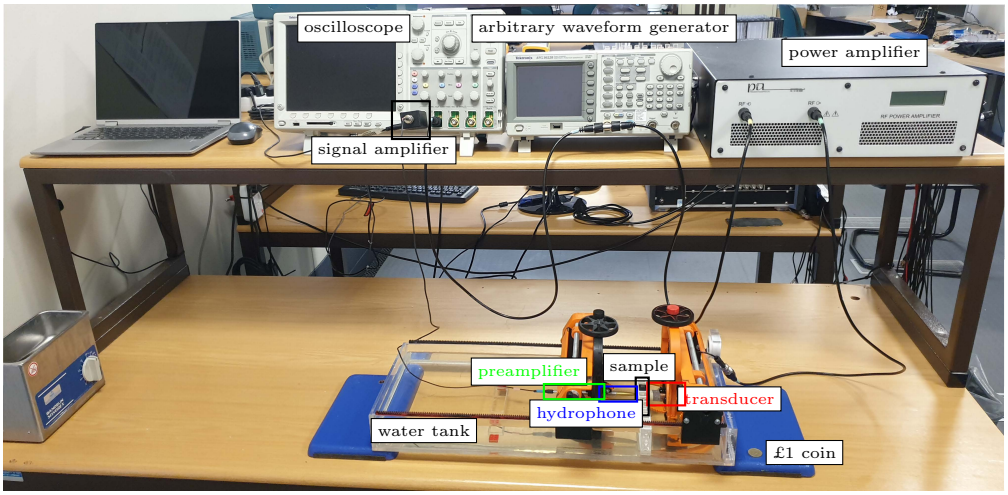

Figure 3.3: Image of ultrasound generation and measurement setup

3.3 Experimental variables and values

The acoustic variables of interest for this research were the acoustic centre frequency and acoustic pressure amplitude. The AFG3022B arbitrary waveform generator was set to generate a pulsed signal of 100 cycles of a sinusoid at a selected centre frequency. The signal was pulsed every 1 ms regardless of the centre frequency. The centre frequency (of the sinusoid) was varied from 1 MHz to 10 MHz in 1 MHz intervals.

The acoustic amplitude was varied from 0 kPa to 100 kPa in 10 kPa intervals for a selected centre frequency. This generates the *null* experiment (0 kPa) and ten other actively exposed samples, for the selected frequency. This process generates 100 experimental points of interest for the actively exposed range.

Additionally, the transducer could generate higher acoustic pressures at specific frequencies. For 5 MHz, additional acoustic pressures of 200 kPa, 250 kPa, 300 kPa and 400 kPa were tested. For 6 MHz and 10 MHz, additional pressures of 200 kPa to 500 kPa in 100 kPa increments were tested. Lastly for 7 MHz, 8 MHz and 9 MHz, additional pressures of 200 kPa to 800 kPa in 200 kPa increments were tested. The range of variables are summarised in Table 3.1.

Table 3.1: Summary of control variable values

	Frequency [MHz]	Acoustic pressure range [kPa]	Increments [kPa]
standard	1-10	0-100 (including null)	10
additional	5	200, 250, 300 and 400	
	6 and 10	200-500	100
	7-9	200-800	200

The transducer and A150 RF power amplifier primarily limited these acoustic pressure control variable parameters. The upper-frequency limit was determined from the capabilities of the AFG3022B arbitrary waveform generator with the pulsed setting used (12.5 MHz maximum); with the upper frequency of 10 MHz being chosen for experimental convenience. The hydrophone is specified to have a calibrated bandwidth from 1 MHz to 20 MHz and, for accuracy purposes, specifies the experiments' lower frequency limit of 1 MHz. The setup is therefore specified over the frequency range of 1 MHz to 10 MHz as mentioned above.

3.3.1 Verification of acoustic pressures

The ultrasound experiment setup determined the acoustic ranges (as seen in Figure 3.3). Distilled water was used in the test sample for the purpose of acoustic calibration and

verification.

The Onda HGL-0200 hydrophone sensitivity is frequency dependent and reported as an End-of-cable Open Circuit (EOC) sensitivity, $M_{eoc}(f)$. This $M_{eoc}(f)$ is provided explicitly in a data file. The measurement system sensitivity changes when the hydrophone is coupled with the Onda AH-2010-025 preamplifier. To accommodate for such changes, the documentation of the hydrophone provides the following correction,

$$M_L(f) = G(f)\ M_{eoc}(f)\frac{C_H(f)}{C_H(f) + C_A(f)} \tag{3.1}$$

where, $M_L(f)$ is the frequency-dependent loaded hydrophone-preamplifier system sensitivity; $G(f)$ is the frequency-dependent preamplifier gain factor; $M_{eoc}(f)$ is the frequency-dependent hydrophone EOC sensitivity; and C_H and C_A are the hydrophone and preamplifier frequency-dependent capacitance respectively.

The capacitance of the hydrophone is frequency dependent and provided in the calibration data file, with the EOC sensitivity. Likewise, for the preamplifier, the frequency-dependent gain and frequency-dependent capacitance is explicitly provided in a data file. The resultant $M_L(f)$ is simply calculated from all the provided calibration data. The resultant loaded hydrophone-preamplifier system sensitivity is shown in Figure 3.4a. The unit of the calibration data provided is $\mathrm{nV\,Pa^{-1}}$. For convenience, this is changed to mV/10kPa (millivolt per 10 kilopascal, i.e. in increments of the pressure variable), with a scaling factor of 0.01. This is shown in Figure 3.4b and explicit values are given in Table 3.2.

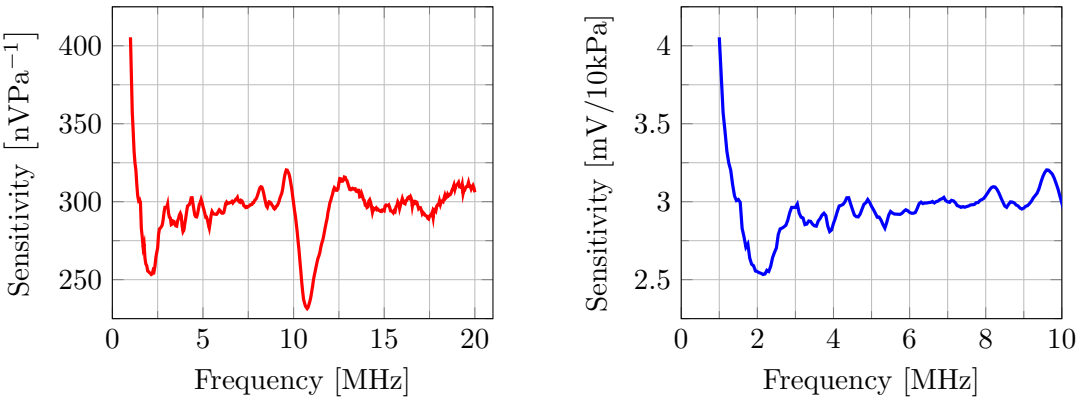

(a) original sensitivity calibration data

(b) scaled sensitivity in range of interest

Figure 3.4: Frequency dependent sensitivity of the hydrophone-preamplifier system.

Table 3.2: Hydrophone-preamplifier system sensitivity at the experimental control frequencies

Frequency[MHz]	Sensitivity [mV/10kPa]
1	4.05
2	2.55
3	2.96
4	2.86
5	2.97
6	2.93
7	3.00
8	3.04
9	2.96
10	2.99

3.4 Sample processing protocol

An aqueous stock solution of carbon black microparticles (cbmp) was made from Zuper Black pigment dispersion (INTENZE Products, Inc., Rochelle Park, NJ, USA), by diluting the pigment in proportions of 250 µL of ink to 1 L of distilled water. From this aqueous stock solution of suspended microparticles, samples were made and used for experimentation.

The frequency of the signal generator was selected for the desired experimental set. This was kept constant for the particular experimental set. The desired amplitude for the specific sample under test was then selected. The signal was verified using the hydrophone measurement setup and a distilled water blank sample.

The sample was prepared by using a syringe to transfer 3 mL of tattoo ink aqueous stock into a cuvette. The cuvette was then sealed with a custom-made TPU 95 cap. The sample was placed in the custom-made rack in the exposure area in the ultrasound water tank, ready to be sonicated.

The signal generator output was then enabled while a timer was set for 5 min. The hydrophone measurement system remained in use and the signal was monitored on the oscilloscope to ensure the acoustic regime was consistent for the duration of the 5 min exposure. Once the sample was sonicated for 5 min, the signal generator output was disabled, and the sample was removed from the tank (and subsequently replaced with the blank again, ready for selecting the next regime parameters). The exposed sample was lightly overturned twice by hand to lightly mix the sample. This ensured that if any part of the sample was locally or partially sonicated and not the entire sample, then the effect of the acoustic exposure was averaged throughout the sample by the light mixing.

The cap was then removed, and 1.5 mL of the sample was micropippetted out (3×500µL) into another cuvett, which was further prepared for imaging. 1.5 mL (3×500µL) of octanol was added to the sample for partitioning. The cuvette was caped off again and put aside on a cuvette rack while other samples of the experimental set (specifically of the other controlled acoustic pressures) were prepared. Once the experimental set was complete, the imaging blank calibration reference (containing only 1.5 mL of octanol and

1.5 mL of distilled water) was also added to form the imaging sample set. All the samples were mechanically shaken with a mechanical shaker, with each sample being shaken for 10 s.

The samples were then left to partition for 2.5 min, and an image was taken using the setup as explained in Section 3.5. After another 2.5 min (5 min total) the samples were imaged again. The comparison between these two images indicates if there is a transient effect in partitioning that could impact the interpretation of the results.

The samples were then re-shaken by hand for 10 s immediately after the 5 min interval image was taken, and left for another 2.5 min (7.5 min total). The samples were then imaged again. The comparison of this image to the previous images is to indicate if the hydrophobicity recovers from the re-gassing of the hydrophobic particles.

The experiments were repeated with the same constant controlled frequency and controlled variable of acoustic pressures, until there were five corresponding images for this experimental set. This enabled a statistical analysis of the measured partition coefficients. A new controlled frequency was then selected, and the process was repeated.

The experiments are divided conceptually according to the standard and extended pressure range groups and the imaging time. There are three associated imaging time data sets for the two pressure range groups. Each imaging time data set has its collective 100 sample points, corresponding to each frequency and pressure (in the respective pressure range group). As mentioned, each experimental point, with its corresponding frequency and pressure, has five values for statistical verification and analysis.

3.5 Imaging setup and digital image processing (DIP)

The imaging setup consists of a laptop, Microsoft LifeCam HD-3000 (720p HD) webcam, and a white A3 sheet of paper (Mondi Rotatrim, Bedfordview, South Africa). The paper was used as a uniform background for imaging. The paper was curved on the corner of a desk and wall to eliminate a crease. This prevents a line artefact in the image. The footprint of a cuvette rack was marked on the paper. The cuvette rack is placed on this

footprint for consistent imaging. The cuvette rack used for imaging was made from white PLA. The camera was placed in a 3D printed camera housing for better geometric control and imaging alignment. The centre of the camera's sensor was placed 400 mm from the centre mark of the rack on the paper. A fluorescent ring light was positioned about half a meter above the camera and angled to face the imaging area for a better and more consistent lighting environment. The webcam was connected directly to a laptop via universal serial bus (USB). The laptop was then used to take and store digital images with a MATLAB script.

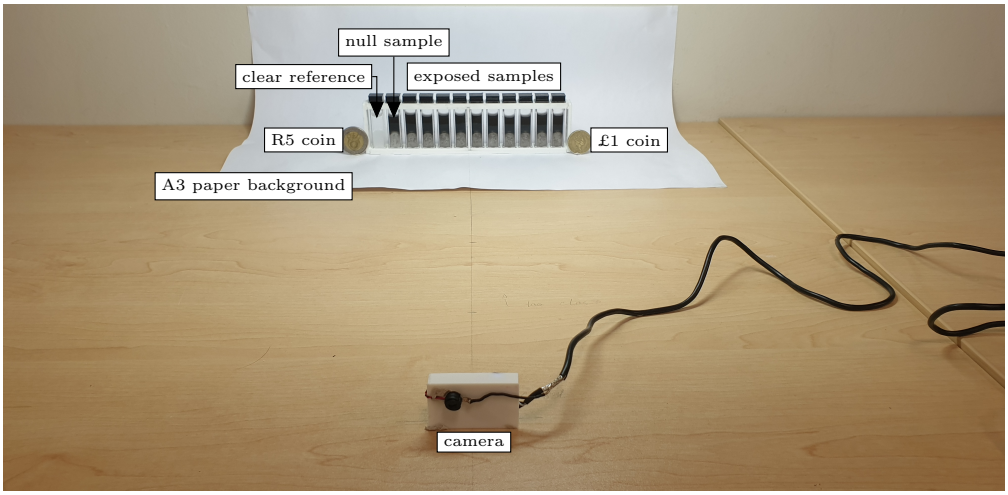

Figure 3.5: A closeup of the imaging area

3.5.1 Digital image processing region of interest extraction

The MATLAB script implemented a colourimetry algorithm modified for calculating the partition coefficient. The algorithm used an image mask to extract each of the samples region of interest (ROI) for both the octanol and water phases. The ROI mask consisted of 15×25 pixels and was manually positioned in the centre of the phase and, ideally, did not include any meniscus of the phases. The average pixel value of the ROI was calculated for each sample's octanol and water ROI.

The clear reference sample was used as a colourimetric calibration because the octanol and water components of the samples have their own colourimetric absorption characteristics,

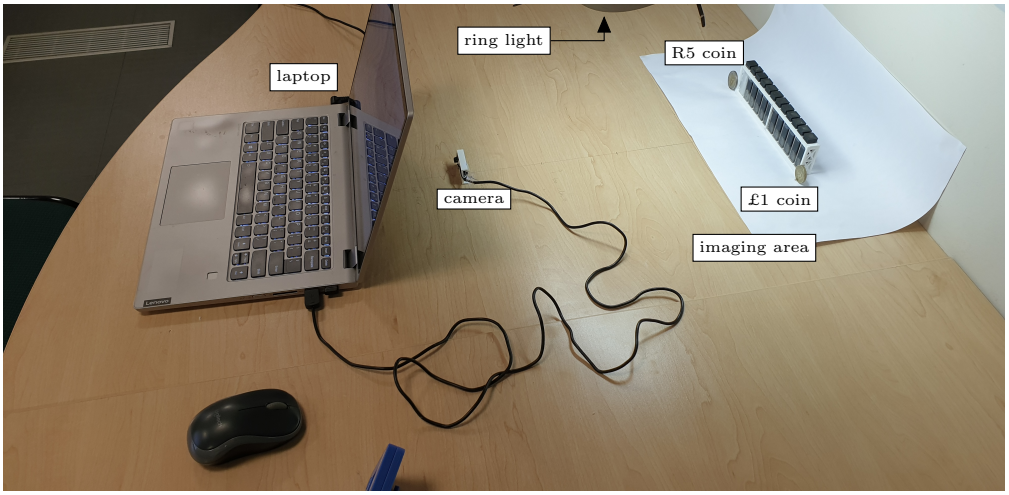

Figure 3.6: Overview of the imaging area

discussed in Subsection 3.5.2. The average pixel value for the clear reference was set as the maximum value for the exposed samples' ROI. Each of the exposed sample's ROI average pixel value was converted to a ratio of the phase's maximum value, the ROI intensity ratio. Only the relative intensity is of interest and not the explicit concentration of each phase (by the nature of the partitioning coefficient). Therefore, the ROI intensity ratio is sufficient for calculating the partition coefficient. The ROI intensity ratio for each octanol and water phase of each sample was then used to calculate the partition coefficient for the sample under the control variable conditions. The calculation of the partition coefficient is briefly covered in Subsection 3.5.2. The results generated by the MATLAB script are shown in Chapter 4.

3.5.2 Colourimetry partition coefficient calculation

The partition coefficient of the carbon black microparticles is calculated using the principles of colourimetry. The full derivation of the fundamental equation used to calculate the partition coefficient is provided in Appendix C. The source code implementation of the ROI extraction and partition coefficient calculation is covered extensively in Appendix D. The fundamental objective of the code is to extract the relevant ROIs pixel values of the samples in the images and perform digital processing to calculate the

partition coefficient. A high-level overview of how the partition coefficient is calculated is briefly covered.

The concept of colourimetry depends on the absorption of light described through the Beer-Lambert-Law, covered in Chapter 2. The law is adapted to account for the non-zero absorption of the phase and cuvette. The absorption from each component in the optical path is additive. This results in the generic expression of light intensity through the lumped cuvette and phase, and the isolated absorption from the cbmp,

$$I^{\varphi}_{\mathrm{cbmp_{eff}}} = I_{\mathrm{eff}_{\varphi}} e^{\left(-\alpha_{\mathrm{cbmp}} c^{\varphi}_{\mathrm{cbmp}}\right)} \tag{3.2}$$

where, $I^{\varphi}_{\mathrm{cbmp_{eff}}}$ is the effective transmitted light intensity, passing through the cuvette, phase and carbon black microparticles; $I_{\mathrm{eff}_{\varphi}}$ is the effective intensity of light due to only the cuvette and phase, i.e. the transmitted light through the cuvette and phase only; α_{cbmp} is the lumped optical molar-path-length attenuation coefficient and optical path length for the carbon black microparticles; and $c^{\varphi}_{\mathrm{cbmp}}$ is the phase concentration of the carbon black microparticles.

Therefore, the effective intensity of a sample in both the octanol and water phase is then,

$$I^{\mathrm{oct}}_{\mathrm{cbmp_{eff}}} = I_{\mathrm{eff_{oct}}} e^{\left(-\alpha_{\mathrm{cbmp}}\ c^{\mathrm{oct}}_{\mathrm{cbmp}}\right)} \qquad I^{\mathrm{wat}}_{\mathrm{cbmp_{eff}}} = I_{\mathrm{eff_{wat}}} e^{\left(-\alpha_{\mathrm{cbmp}}\ c^{\mathrm{wat}}_{\mathrm{cbmp}}\right)} \tag{3.3}$$

where, $I^{\mathrm{oct}}_{\mathrm{cbmp_{eff}}}$ and $I^{\mathrm{wat}}_{\mathrm{cbmp_{eff}}}$ are the total multicomponent transmitted light intensities due to the entire sample in the octanol and water phases, respectively; $I_{\mathrm{eff_{oct}}}$ and $I_{\mathrm{eff_{wat}}}$ are the effective transmitted light intensities of the cuvettes and respective octanol and water phases; α_{cbmp} is as before; $c^{\mathrm{oct}}_{\mathrm{cbmp}}$ and$c^{\mathrm{wat}}_{\mathrm{cbmp}}$ are the concentrations of carbon black microparticles in each respective octanol and water phase.

The final code-implemented Colourimetric Partition Coefficient Equation 3.4 is then,

$$\log_{10} P = \log_{10} \left(\frac{\ln\left(\dfrac{I_{\mathrm{eff_{oct}}}}{I^{\mathrm{oct}}_{\mathrm{cbmp_{eff}}}}\right)}{\ln\left(\dfrac{I_{\mathrm{eff_{wat}}}}{I^{\mathrm{wat}}_{\mathrm{cbmp_{eff}}}}\right)} \right) \tag{3.4}$$

where, $I_{\mathrm{eff_{oct}}}$ is the mean pixel value in the ROI of the clear reference's octanol phase; $I_{\mathrm{eff_{wat}}}$ is the mean pixel value in the ROI of the clear reference's water phase; $I^{\mathrm{oct}}_{\mathrm{cbmp_{eff}}}$ is the mean pixel value in the ROI of the sample's octanol phase; and $I^{\mathrm{wat}}_{\mathrm{cbmp_{eff}}}$ is the mean

pixel value in the ROI of the sample's water phase. The equation is independent of the α_{cbmp} term. It depends on the sample's transmitted light intensity, and the only other dependence is on the reference intensity of the clear samples phases (and not explicitly on their underlying parameters and values). Again, these equations are derived and detailed in length in Appendix C. Equation 3.4 is then used to calculate the partition coefficient for the specific sample imaged.

3.6 Statistical methods for the analysis of results

Each sample measurement $\log_{10}\{P(f,p)\}$ corresponds to a sample point, with a controlled acoustic frequency f and acoustic pressure p (and time of imaging). The experiments were repeated five times to produce five measured partition coefficients for basic statistical analysis and rigidity. All the null experiments compound, thus having more total samples in the generalised analysis (five per frequency at 0 kPa). The mean partition coefficient $\overline{\log_{10}\{P(f,p)\}}$ and the standard deviation $\sigma_{\log_{10}\{P(f,p)\}}$, for the specific f and p sample point were calculated. These are then tabulated according to their corresponding regime parameters f and p unique to that experimental point for each imaging time category in Chapter 4. The results are further combined along contours of constant frequency and constant pressure. The averages along constant pressure contours isolate the average effect of changes in pressure on microparticle hydrophobicity. These pressure contour averages effectively produce an expression for the average partition coefficient as an average function of pressure, along a frequency contour. Similarly, the averages along constant frequency contours isolate the average effect of changes in frequency on microparticle hydrophobicity. Again, these frequency contour averages produce the average partition coefficient as an average function of frequency, along a pressure contour. Additionally, the image set's overall average $\overline{\log_{10}\{P_{f,p}\}}$ and standard deviation $\sigma_{\log_{10}\{P_{f,p}\}}$ of all the sonicated samples were evaluated for holistic analysis and comparison.

Linear statistical regression analysis was employed to quantify the effect that acoustic frequency and pressure individually have on the partition coefficient. (As will be seen in Chapter 4, the trends are all approximately linear). The regression parameters provide the quantified effects of acoustic frequency and pressure on microparticle hydrophobicity.

The gradient regression parameter indicates the correlated change in magnitude of the partition value as a result of a change in the controlled frequency/pressure. Comparing the constant regression parameter with the mean null value specifies any relative change that occurs due to the presence of ultrasound by default. The linear regression equations are of the form

$$\log_{10}\{P(f)_p\} = b_f f + a_f \pm \sigma \tag{3.5}$$

$$\log_{10}\{P(p)_f\} = b_p p + a_p \pm \sigma \tag{3.6}$$

where, $\log_{10}\{P(x)_y\}$ is the partition coefficient (in log base 10 form) as an average function of "x", for any given constant contour of "y"; f is the controlled frequency; p is the controlled pressure; b_f and b_p are the linear regression gradients for frequency and pressure respectively; a_f and a_p are the regression y-intercept values for frequency and pressure respectively; and σ_s is the standard deviation of the samples.

The standard deviation σ in both equations is not the standard deviation of the contour means. Rather, it is the standard deviation of the entire sample set, reasoned as follows. Since the equations are along contours, each contour mean has its own standard deviation. The contour standard deviation is the average standard deviation of the sample points' standard deviations along the contour. The average standard deviation was calculated using

$$\sigma = \sqrt{\frac{n_1{\sigma_1}^2 + n_2{\sigma_2}^2 + \cdots + n_k{\sigma_k}^2}{\Sigma n_k - k}} \tag{3.7}$$

where, σ is the average standard deviation; k is the number of experimental points (at specific frequencies and pressures) along the contour; $n(= 5)$ is the sample size of the k^{th} experimental point; and σ_k is the standard deviation of the samples at the k^{th} experimental point. These contour standard deviations were then averaged again for the final equation, which necessarily is the total standard deviation of all the experimental points.

Importantly the null experiment value necessarily has the following form

$$\log_{10}\{P_{\text{null}}\} = a_{\text{null}} \pm \sigma_{\text{null}} \tag{3.8}$$

Since there was no change in the controlled variables, i.e. the acoustic pressure and frequency were held at 0 MHz and 0 kPa, the gradient "b_{null}" of the regression is zero. The

"y-intercept" of this equation is by definition equal to the null mean, $a_{\text{null}} = \overline{\log_{10}\{P_{\text{null}}\}}$.

3.6.1 Possible outcomes of the statistical and regression analysis

It is important to cover the possible outcomes of the linear regression analysis. These outcomes define the quantified effect of ultrasound on microparticle hydrophobicity. Four overarching outcomes originate from the possible relations of the regression parameters with each other and the null mean. These four outcomes are summarised in a logic table with their accompanying graphics Table 3.3. They are discussed in detail below.

No effect from ultrasound

Firstly, ultrasound may have no quantified effect on microparticle hydrophobicity measured through the partition coefficient. If this is the case, then both of the gradients are zero, $b_f = b_p = 0$, and the null mean and overall sonicated mean are equal, $\overline{\log_{10}\{P_{\text{null}}\}} = \overline{\log\{P_{f,p}\}}$. Additionally, these means will also equal the y-intercepts by consequence of definition, $\overline{\log_{10}\{P_{\text{null}}\}} = \overline{\log\{P_{f,p}\}} = a_f = a_p$. These results would indicate no quantifiable effect of ultrasound on microparticle hydrophobicity. These results would also mean the 3D surface of all these data points would be a flat plane coincident with the null mean value.

Effect through at least one controlled variable

Secondly, ultrasound may only affect microparticle hydrophobicity through the acoustic frequency and/or pressure parameter(s) only. Specifically, the parameter(s) changes will be correlated to the change in magnitude of the partition coefficient. Since the parameter(s) are the only causal link, the parameters' zero value input will necessarily result in the null mean value. Therefore the linear regression constant will equal the null mean $\overline{\log_{10}\{P_{\text{null}}\}} = a_x$. Additionally, the parameter'(s) causal link means the gradient(s) will be non-zero, $b_x \neq 0$. The linear distribution also results in the

sonicated samples' mean being non-equal to the y-intercept, $\overline{\log_{10}\{P(x)_y\}} \neq a_x$ and therefore $\overline{\log_{10}\{P(x)_y\}} \neq \overline{\log_{10}\{P_{\text{null}}\}}$. Both acoustic frequency and pressure may affect microparticle hydrophobicity and will be indicated separately by their respective linear regression analyses. If this is the case, then from the above argument, $a_f = a_p = a_{\text{null}} = \overline{\log_{10}\{P_{\text{null}}\}}$ and $b_f \neq 0$ and $b_p \neq 0$. The gradients will not necessarily be equal but will be non-zero. The comparably larger gradient will indicate stronger dependence and effect by that parameter. If only the frequency or only pressure affects microparticle hydrophobicity, then the 3D surface plot will show an inclined plane in the corresponding axis direction only. If both affect microparticle hydrophobicity, then the surface will be inclined in both axes' directions.

Effect through an unknown parameter

The third scenario is when frequency or pressure does not affect hydrophobicity. Another possibility is that both frequency and pressure have no effect, but an uninvestigated ultrasound parameter, say "v", does affect microparticle hydrophobicity. More on this later.

For the sake of argument, suppose changes in "y" (exclusively frequency or pressure) affect hydrophobicity, but changes in "x" (the other parameter) does not. The following can be expected from the linear regression of "x" examined here. The linear regression will result in a horizontal line offset from the null mean. Since the gradient is zero, the data is only predicted by its mean. Consequently, the y-intercept of the regression analysis will be equal to the sonicated samples' mean. I.e $a_x = \overline{\log_{10}\{P(x)_y\}} \neq \overline{\log_{10}\{P_{\text{null}}\}}$ and $b_x = 0$. Consider this with the originally stated argument, "y" affecting hydrophobicity. The linear regression of "y" will produce results as explained previously in the second scenario of Section 3.6.1. This parameter, blind to the regression analysis in "x", is actually the source of the null offset. The null offset in the regression analysis of "x" is the indicator that there is an "unknown" parameter (actually "y") that affects the microparticle hydrophobicity. The surface plot will be inclined in only the "y" axis direction. The "y" regression analysis may or may not indicate an overall offset (this is explained further in the fourth scenario of Section 3.6.1).

There are, however, many other attributes and parameters that characterise an ultrasonic signal. Hydrophobicity may be independent of both frequency and pressure but dependent on another ultrasound parameter "v" not investigated in this research. In this research, frequency and pressure are the controlled variables. The experimental design keeps all other ultrasound signal's controllable parameters constant. Since these parameters are kept constant, the only effect this parameter will have on the quantified hydrophobicity is an offset on the y-intercept a_x, and $a_x \neq a_{\text{null}} = \overline{\log_{10}\{P_{\text{null}}\}}$. The offset/non-equality is the defining indicator of an unknown parameter affecting microparticle hydrophobicity. I.e. if a_x and $a_y \neq \overline{\log_{10}\{P_{\text{null}}\}}$, then at least one other parameter of ultrasound affects microparticle hydrophobicity. This is true even for the argument above (since the perspective is on "x", the variation of "y" is the source of the offset $a_x \neq \overline{\log_{10}\{P_{\text{null}}\}}$, and "$y$" is the "unknown" variable). Since both frequency and pressure do not affect microparticle hydrophobicity but at least one other ultrasound parameter "v" does, the 3D surface will be a flat plane offset from the null mean.

Effect through at least one controlled variable and an unknown parameter

The fourth and final scenario is a combination of the second and third scenarios, from the second scenario of Section 3.6.1 and third scenario of Section 3.6.1 above. Specifically, frequency and/or pressure affect microparticle hydrophobicity, and an unknown acoustic variable "v". The statistical and regression parameter characteristics will all be relatively the same in each scenario. However, the difference is the offset a_f and/or $a_p \neq \overline{\log_{10}\{P_{\text{null}}\}}$, the defining feature of an unknown acoustic variable. Additionally the y-intercept will not equal the mean, $a_f \neq \overline{\log_{10}\{P(f)_p\}}$ and/or $a_p \neq \overline{\log_{10}\{P(p)_f\}}$. The 3D surface will be a plane, inclined in the frequency and/or the pressure axis directions, offset from the null mean.

summary of statistical outcomes

Each of the linear regression outcomes, as explained above, is summarised in the logic table, Table 3.3. The table also has accompanying generic graphics for the linear regression lines. The results from the linear regression analysis are also complimented with the relevant 3D surface plot. The surface plot is used to verify and emphasise the trend of the data and conclusions drawn from the linear regression. Additionally, in the linear regression analysis, there is a risk that a specific experimental point(s) may exhibit a unique phenomenon at a specific combined frequency and pressure. This point(s) will be lost in the averaging process. The 3D surface plot of the partition coefficients enables visual confirmation if this occurs. Furthermore, the 3D surface plot enables a visual critique and interpretation of the results if such a point(s) exists.

Table 3.3: Logic table of the effect of ultrasound from the linear regression parameter values

	$a_{f,p} = a_{\text{null}}$, y-intercept equals null mean	$a_{f,p} \neq a_{\text{null}}$, y-intercept not equal to null mean
$b_{f,p} = 0$, zero gradient	**1) No effect from ultrasound** 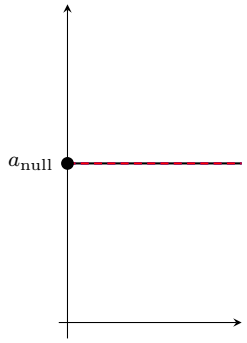 Ultrasound has no quantifiable effect on microparticle hydrophobicity. Indicated by both a gradient of zero and co-incidence with the null mean for both parameters.	**3) Effect through an unknown parameter** 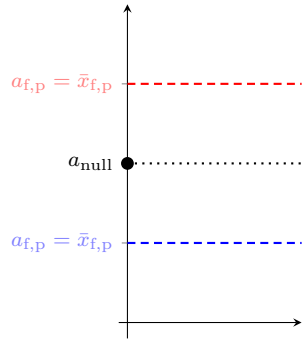 Frequency and/or pressure do not affect microparticle hydrophobicity. However, microparticle hydrophobicity is affected by an unknown acoustic variable "x". Indicated by a zero gradient and an offset from the null mean.
$b_{f,p} \neq 0$, non-zero gradient	**2) Effect through at least one controlled variable** 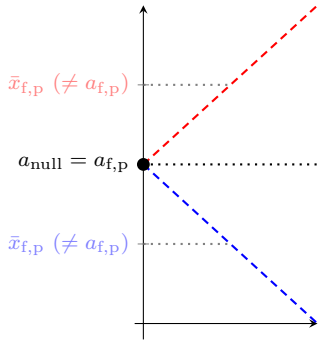 Microparticle hydrophobicity is quantifiably affected by frequency and/or pressure dominantly. Indicated by a non-zero gradient and coincidence with the null mean.	**4) Effect through at least one controlled variable and an unknown parameter** 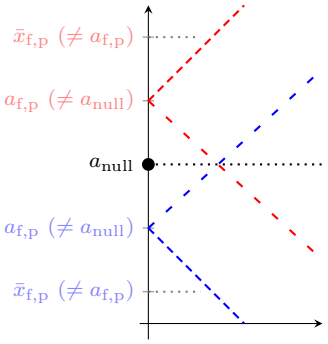 Microparticle hydrophobicity is quantifiably affected by frequency and/or pressure, and an unknown acoustic variable "x". Indicated by a non-zero gradient and an offset from the null mean.

Chapter 4

Results

This chapter presents the results of the partition coefficients of the microparticle samples, as measured through the digital image processing (DIP) of the imaged partitioned samples. The transducer acoustic calibration results and characteristics are first summarised below in Section 4.1. This provides validity in the acoustics of the experimental setup and the actual results from the experiment. Following this are the core results of the experiment.

The experimental procedure started at a selected ultrasound frequency, in the range of 1 MHz to 10 MHz. The acoustic pressure was then varied from 0 kPa to 100 kPa in 10 kPa increments, for the selected frequency. This defines the standard pressure range. For specifically selected frequencies, the pressure range was increased to as high as 800 kPa. This defines the extended pressure range. The results are categorised according to these defined standard and extended pressure ranges.

Samples of hydrophobic carbon black microparticles were subsequently exposed to these ultrasound regimes. The hydrophobicity of the microparticle suspension was measured using the octanol-water partition coefficient method, and their value was calculated with colourimetric methods.

These experiments involve the three-dimensional (3D) space of controlled-variable acoustic frequency, controlled-variable acoustic pressure, and the dependent-variable partition coefficient, measured from the ultrasonically exposed microparticles. These experiments were repeated such that there were five results for each experimental point for statistical

analysis.

The partition values of the 0 kPa unsonicated hydrophobic carbon black microparticles were used as the null experiment reference. These null samples were used to evaluate any relative change in the partition values of the sonicated samples. The partitioned samples were imaged at 2.5 min, 5 min and 7.5 min. The inherent stability of the change in hydrophobicity caused by ultrasound was evaluated by comparing the results from the 2.5 min and 5 min images. At the 5 min interval, and after the samples were imaged for the 5 min set, the samples were manually reshaken for 10 s. This enables the stability over the 2.5, 5 min time interval to be compared to the reshaken samples imaged at 7.5 min. The results of the experiments for the standard and extended pressure ranges are further grouped according to these time intervals.

The samples were imaged and processed using DIP. Colourimetric measurements of the samples were then used to calculate the partition coefficient. The measured partition coefficients were further processed using statistical and linear regression methods. The results of those methods are presented below in Section 4.3.

4.1 Transducer acoustic calibration and characteristics

The experimental results depend on acoustic frequency and pressure amplitude control variables. The validation of the quality of the acoustic regime characteristics is important for any relationship that is concluded between the control variables and the dependent variable. The experimental control variables were measured with the hydrophone system as explained in Subsection 3.3.1. The transducer's detailed acoustic calibration results can be seen in Appendix A. The time-domain signal of the signal generator voltage and measured acoustic signal of the hydrophone, as well as the frequency-domain spectrum of the signals are shown therein. The pressure amplitude of the acoustic signal was directly validated with the oscilloscope in the time domain, and need not be discussed further. The frequency of the acoustic signal, and any harmonics present at a selected acoustic pressure amplitude, are determined from the frequency-domain spectrum. The transducer exhibited acoustic amplitude-dependent harmonic behaviour at 1 MHz, 2 MHz, 3 MHz and 4 MHz. These results are summarised in the tables below. For all other frequencies

and acoustic pressures, there are no noticeable harmonics present nor any significant acoustic signal distortions.

Table 4.1: Transducer harmonic characteristics for a fundamental frequency of 1 MHz

Acoustic Amplitude [kPa]	Harmonic Frequency [MHz]	Harmonic Amplitude [% fundamental]
50	3	< 10
100	2	20
	3	50
	5	50
	7	40

The transducer has numerous harmonic behaviours at 1 MHz as seen in Table 4.1. The transducer starts to exhibit harmonic behaviour for acoustic pressure amplitudes $\geq$50 kPa. The harmonics become significant at the maximum experimental control acoustic pressure amplitude of 100 kPa. The effective acoustic signal can be better approximated qualitatively as a 1 MHz positive and negative pulse train with down-ringing. See Figure A.3 for the graphed details. Note the harmonics are still <10 MHz.

Table 4.2: Transducer harmonic characteristics for a fundamental frequency of 2 MHz

Acoustic Amplitude [kPa]	Harmonic Frequency [MHz]	Harmonic Amplitude [% fundamental]
50	6	< 5
100	6	75
	8	10

At 2 MHz, the transducer has some harmonic behaviour seen in Table 4.2. The transducer starts to exhibit harmonic behaviour for acoustic pressure amplitudes >50 kPa. The harmonics become significant at the maximum experimental control acoustic pressure amplitude of 100 kPa. The effective acoustic signal can be better approximated qualitatively as a 2 MHz triangular-like waveform. See Figure A.6 for further details. Again, the harmonics are still <10 MHz.

At 3 MHz, the transducer has some harmonic behaviour seen in Table 4.1. The transducer only exhibits harmonic behaviour for an acoustic pressure amplitude of 100 kPa. The

Table 4.3: Transducer harmonic characteristics for a fundamental frequency of 3 MHz

Acoustic Amplitude [kPa]	Harmonic Frequency [MHz]	Harmonic Amplitude [% fundamental]
100	6	< 5
	9	20

harmonics are also relatively weak, and there is no significant signal distortion. See Figure A.9 for the graphed results. The harmonic is still <10 MHz.

Table 4.4: Transducer harmonic characteristics for a fundamental frequency of 4 MHz

Acoustic Amplitude [kPa]	Harmonic Frequency [MHz]	Harmonic Amplitude [% fundamental]
100	6	< 5

The transducer has limited harmonic behaviour at 4 MHz as seen in Table 4.1. The transducer only exhibits harmonic behaviour for an acoustic pressure amplitude of 100 kPa. The harmonics are also relatively negligible, and there is no significant signal distortion. See Figure A.12 for the graphed results. The harmonic is negligible and <10 MHz.

4.2 Experimental results

The complete results from the DIP on all the images and their relevant image sets can be seen in Appendix B. In the graphs of the results provided there, the average partition coefficients of the five experiments are shown with their standard deviation. Although of primary relevance, the results in Appendix B are too extensive for the purpose of general trend analysis here. The following sections provide the results in a more concise and generalised format. The purpose is catered specifically to determine the investigated parameters' quantified effect on hydrophobicity, with the goal of finding a suitable linear regression fit and corresponding regression parameter values. These findings are supplemented by the complete results in Appendix B. The statistical and regression analysis methods used to generate these concise and generalised findings were covered in Section 3.6 before.

4.3 Experimental results of the standard pressure range

The results of the experiments for the standard acoustic pressure amplitudes are presented in the relevant tables below. The results are grouped according to the experimental 2.5 min, 5 min and 7.5 min imaging times. The tables represent the results for the specific imaging time in each respective section. Each entry represents the partition coefficient for the relevant acoustic frequency and pressure in the standard pressure range. The value in the entry was obtained from the mean and standard deviation of the partition coefficient from the five samples measured.

The averages of the partition coefficients for each controlled pressure are calculated and seen in the bottom row of the respective tables. This averages out the effect of the varying frequencies along the contours of constant pressure. Subsequently, this isolates the average effect of varying pressure on the partition coefficient, as explained in Section 3.6. Similarly, the average of the partition coefficients for each controlled frequency is calculated and seen in the rightmost column of the respective tables. This averages out the effect of the varying pressures along the contours of constant frequency. Subsequently, this isolates the average effect of varying the frequency on the partition coefficient. When averaging along the frequency contours, the null values in the left column are excluded as this would directly interfere with the results. The mean of all the actively exposed samples (excluding nulls) is seen in the bottom right cell of the relevant table. The mean of the nulls is seen in the bottom left cell, under the null values of the relevant table.

The average effect of varying controlled frequencies on the partition coefficient, and the average effect of varying controlled pressures on the partition coefficient, are graphed. Each graph includes the partition coefficient of the null experiment for comparison with the sonicated sample data (seen explicitly on the y-axis and as a horizontal dotted line). The graph is complemented with the two regression analysis equations of frequency and pressure on the partition coefficient. The 3D surface plot of the dataset in the relevant table is also provided thereafter. This surface plot is the visual representation of the table, and any trends or outliers are more easily visible. This is done for each pressure category and sectioned imaging times below.

4.3.1 Results from samples imaged at 2.5 min

The mean partition coefficients calculated with the DIP code from the images taken at 2.5 min, for each controlled variable combination of acoustic frequency and acoustic pressure, is shown in Table 4.5.

The average effect of varying controlled frequencies on the partition coefficient (right column entries of Table 4.5), and the average effect of varying controlled pressures on the partition coefficient (bottom row entries of Table 4.5), are graphed in Figure 4.1a and Figure 4.1b respectively. Each graph includes the average partition coefficient of the null experiment (the left bottom cell of Table 4.5) for comparison, seen explicitly on the y-axis and as a horizontal dotted line.

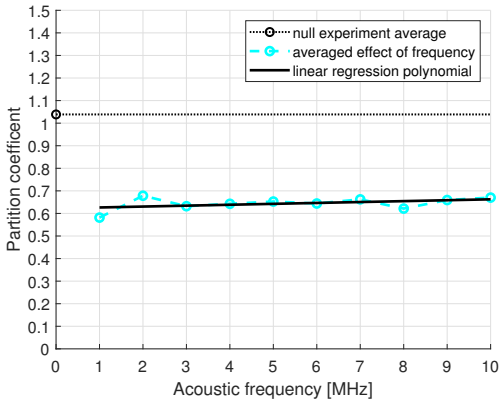

(a) Average effect of the different controlled frequencies

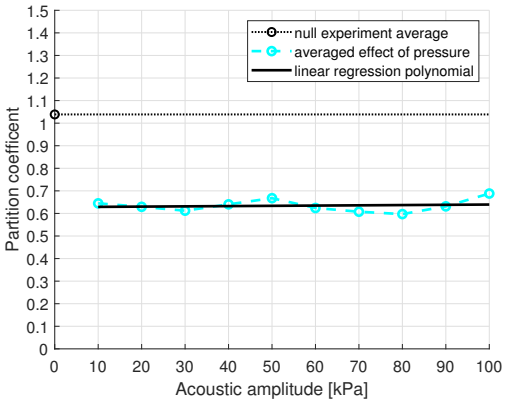

(b) Average effect of the different controlled pressures

Figure 4.1: The averaged effects of the controlled variables on the partition coefficient from images taken at 2.5 min

The graphs have a general horizontal linear trend. The linear regression analysis as covered in Section 3.6 was performed on the average frequency and pressure data. The resultant linear polynomials of variable frequency f and pressure p on the partition coefficient $\log_{10}(P)$ is given in Equation 4.1 and Equation 4.2 respectively.

$$\log_{10}(P) = 0.0040f + 0.6224 \pm 0.10 \tag{4.1}$$

$$\log_{10}(P) = 0.0001p + 0.6279 \pm 0.10 \tag{4.2}$$

As mentioned, the trend of the data is linear. The gradients from the linear regression for both frequency and pressure are, for practical purposes, zero. Therefore, the variation of pressure and frequency variables offer no variation in the distribution of the data. The data is fundamentally only predicted by its mean. The resultant mean of all the sonicated samples from Table 4.5 is 0.63 ± 0.10. There is a clear and quantifiable difference when comparing this value with the value of the null samples, 1.05 ± 0.13. Using the largest standard deviation of ± 0.13, the relative statistical difference in these values is 3.23σ, and is statistically significant. The normal statistical error and standard deviation cannot account for the difference between the null and sonicated sample means alone. Table 4.5 is on the next page.

Table 4.5: Mean partition coefficients of the microparticles imaged at 2.5 min for all controlled acoustic frequencies and standard pressure amplitudes

		(null)	Acoustic Pressure [kPa]										Frequency
		0	10	20	30	40	50	60	70	80	90	100	Averages
Acoustic Frequency [MHz]	1	1.03±0.12	0.65±0.09	0.54±0.11	0.51±0.16	0.56±0.10	0.58±0.12	0.55±0.14	0.53±0.12	0.56±0.16	0.62±0.13	0.71±0.10	0.58±0.13
	2	1.04±0.18	0.65±0.04	0.67±0.06	0.66±0.12	0.69±0.11	0.65±0.08	0.66±0.07	0.73±0.10	0.62±0.07	0.72±0.12	0.73±0.13	0.68±0.10
	3	1.16±0.11	0.61±0.07	0.60±0.05	0.59±0.08	0.64±0.04	0.69±0.04	0.63±0.08	0.62±0.12	0.60±0.11	0.62±0.04	0.72±0.06	0.63±0.07
	4	1.16±0.08	0.64±0.06	0.65±0.12	0.66±0.12	0.62±0.07	0.65±0.09	0.67±0.16	0.65±0.14	0.64±0.17	0.60±0.12	0.64±0.14	0.64±0.12
	5	0.95±0.06	0.65±0.07	0.64±0.07	0.61±0.07	0.62±0.09	0.69±0.09	0.64±0.09	0.60±0.10	0.60±0.13	0.62±0.09	0.73±0.09	0.64±0.09
	6	1.09±0.10	0.65±0.10	0.61±0.09	0.54±0.05	0.62±0.09	0.66±0.09	0.59±0.07	0.60±0.13	0.59±0.12	0.62±0.13	0.69±0.09	0.62±0.10
	7	0.96±0.19	0.66±0.12	0.74±0.10	0.66±0.10	0.72±0.08	0.69±0.11	0.66±0.09	0.62±0.14	0.63±0.09	0.63±0.08	0.63±0.06	0.67±0.10
	8	0.99±0.10	0.63±0.14	0.58±0.11	0.60±0.14	0.65±0.15	0.65±0.16	0.58±0.17	0.52±0.11	0.53±0.10	0.59±0.13	0.67±0.08	0.60±0.13
	9	1.08±0.12	0.65±0.06	0.61±0.08	0.64±0.07	0.60±0.12	0.73±0.10	0.61±0.13	0.56±0.09	0.60±0.07	0.60±0.08	0.72±0.08	0.63±0.09
	10	1.05±0.19	0.64±0.09	0.64±0.01	0.67±0.03	0.69±0.02	0.68±0.10	0.67±0.10	0.65±0.09	0.60±0.07	0.69±0.05	0.67±0.08	0.66±0.07
Pressure Averages		1.05±0.13	0.64±0.09	0.63±0.09	0.61±0.10	0.64±0.09	0.67±0.10	0.62±0.12	0.61±0.11	0.60±0.11	0.63±0.10	0.69±0.09	0.63±0.10

For visualisation, the results from Table 4.5 of this imaging time set are presented as 3D surface plot in Figure 4.2. The horizontal axes are the controlled frequency and controlled acoustic pressure amplitude, and the vertical axis is the partition coefficient of the acoustically exposed microparticles. The surface has no noticeable peak; however, there is a clear offset between the null and actively exposed samples. This is supported by the results of the statistical analysis of the frequency and pressure average data seen above. The broader context of these results discussed further in Subsection 5.1.1.

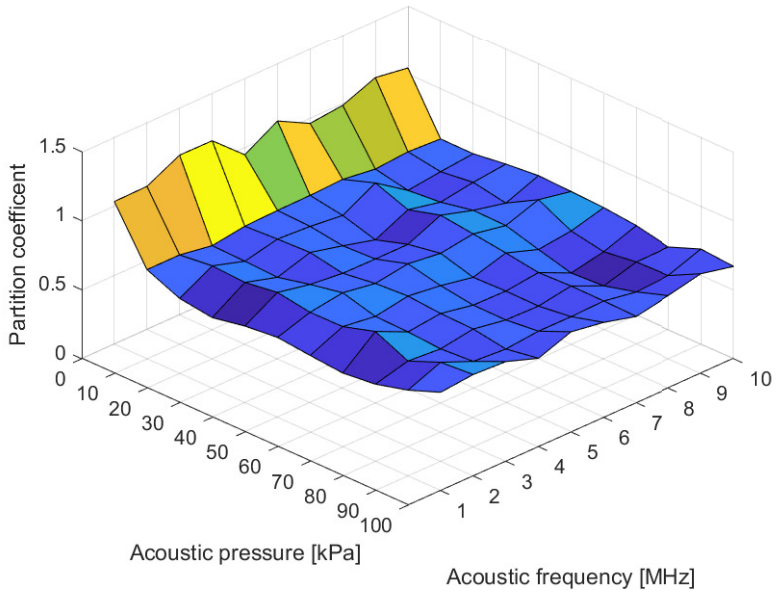

Figure 4.2: The surface plot of the partition coefficients of the microparticles imaged at 2.5 min vs the controlled acoustic frequency and acoustic pressure amplitude of the acoustic regimes.

Figure description: The yellow surface indicates the comparatively large change in hydrophobicity of the acoustically exposed microparticles, compared to the null samples (on the top back edge along an acoustic pressure contour of 0 kPa). The blue surface of the actively exposed samples is relatively flat and consistently below the values of the nulls. The nulls have a mean value of $\log_{10}(P)$ =1.05. The mean of the blue surface is at $\log_{10}(P)$ =0.63.

4.3.2 Results from samples imaged at 5 min

The mean partition coefficients calculated with the DIP code from the images taken at 5 min, for each controlled variable combination of acoustic frequency and acoustic pressure, is shown in Table 4.6.

The average effect of varying controlled frequencies on the partition coefficient (right column entries of Table 4.6), and the average effect of varying controlled pressures on the partition coefficient (bottom row entries of Table 4.6), are graphed in Figure 4.3a and Figure 4.3b respectively. Each graph includes the average partition coefficient of the null experiment (the left bottom cell of Table 4.6) for comparison, seen explicitly on the y-axis and as a horizontal dotted line.

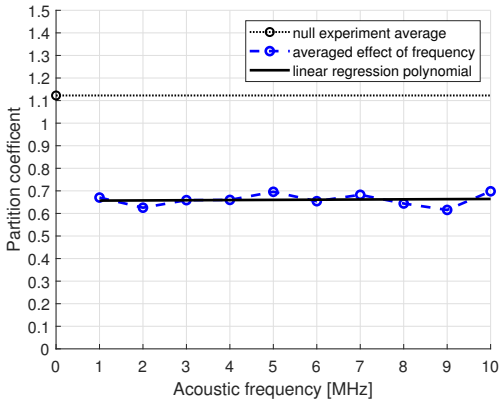

(a) Average effect of the different controlled frequencies

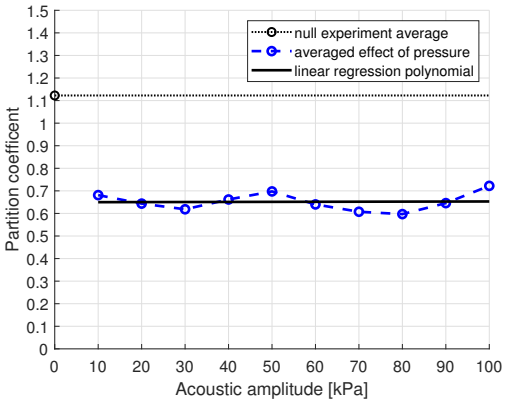

(b) Average effect of the different controlled pressures

Figure 4.3: The averaged effects of the controlled variables on the partition coefficient from images taken at 5 min.

The graphs are linear and horizontal. Linear regression analysis is performed on each of the averages. The linear polynomials of variable frequency f and pressure p on the partition coefficient $\log_{10}(P)$ is given in Equation 4.3 and Equation 4.4 respectively.

$$\log_{10}(P) = 0.0008f + 0.6561 \pm 0.13 \tag{4.3}$$

$$\log_{10}(P) = 0.0000p + 0.6496 \pm 0.13 \tag{4.4}$$

This trend is similar to the trend seen from the results in the 2.5 min results. Similarly, the gradient values seen here are also negligible. I.e. the variation in acoustic frequency and pressure offer no variation in the values of the partition coefficient measured. Again the data is only predicted by its mean. This is also consistent with the results seen previously in the 2.5 min results, Subsection 4.3.1. From Table 4.6, the total mean of the sonicated samples is 0.65 ± 0.13, and the mean of the null samples is 1.12 ± 0.15. This is a clear and quantifiable difference, with the two values relatively separated by 3.13σ and is statistically significant. The statistical variation of either cannot account for the difference alone. These results are consistent with those found in Subsection 4.3.1. The only difference is a slight increase in the partition coefficient values compared to those in Subsection 4.3.1.

Table 4.6: Mean partition coefficients of the microparticles imaged at 5 min for all controlled acoustic frequencies and standard pressure amplitudes

		(null)	Acoustic Pressure [kPa]										Frequency
		0	10	20	30	40	50	60	70	80	90	100	Averages
Acoustic Frequency [MHz]	1	1.05±0.11	0.75±0.08	0.67±0.17	0.61±0.21	0.65±0.09	0.72±0.12	0.59±0.14	0.63±0.15	0.61±0.13	0.68±0.07	0.81±0.08	0.67±0.13
	2	1.04±0.18	0.63±0.12	0.67±0.11	0.63±0.17	0.60±0.22	0.61±0.22	0.62±0.16	0.60±0.13	0.57±0.13	0.66±0.16	0.68±0.14	0.63±0.16
	3	1.19±0.13	0.69±0.10	0.68±0.09	0.60±0.04	0.68±0.10	0.72±0.12	0.65±0.11	0.57±0.07	0.58±0.08	0.63±0.10	0.79±0.13	0.66±0.10
	4	1.16±0.18	0.64±0.19	0.67±0.12	0.65±0.18	0.62±0.12	0.64±0.14	0.69±0.15	0.66±0.11	0.64±0.13	0.65±0.13	0.73±0.14	0.66±0.14
	5	1.04±0.17	0.73±0.15	0.68±0.14	0.70±0.17	0.69±0.14	0.78±0.12	0.68±0.17	0.65±0.13	0.64±0.13	0.65±0.06	0.74±0.11	0.69±0.14
	6	1.20±0.11	0.65±0.14	0.54±0.19	0.55±0.06	0.62±0.12	0.71±0.13	0.64±0.11	0.62±0.14	0.59±0.08	0.66±0.12	0.74±0.13	0.63±0.13
	7	1.12±0.19	0.75±0.14	0.71±0.09	0.58±0.16	0.78±0.08	0.72±0.08	0.68±0.06	0.66±0.16	0.61±0.19	0.65±0.22	0.63±0.16	0.68±0.14
	8	1.10±0.15	0.64±0.13	0.65±0.17	0.63±0.12	0.67±0.14	0.73±0.16	0.59±0.14	0.55±0.06	0.58±0.07	0.62±0.10	0.72±0.13	0.64±0.13
	9	1.13±0.12	0.65±0.07	0.49±0.28	0.58±0.13	0.56±0.19	0.62±0.12	0.54±0.11	0.51±0.07	0.50±0.08	0.54±0.09	0.73±0.11	0.57±0.14
	10	1.19±0.16	0.67±0.10	0.68±0.07	0.65±0.06	0.74±0.06	0.75±0.05	0.72±0.08	0.63±0.08	0.63±0.10	0.73±0.10	0.72±0.09	0.69±0.08
Pressure Averages		1.12±0.15	0.68±0.13	0.64±0.15	0.62±0.14	0.66±0.14	0.70±0.13	0.64±0.13	0.61±0.12	0.60±0.12	0.65±0.12	0.73±0.12	0.65±0.13

For visualisation, the results from Table 4.6 of this imaging time set are presented as 3D surface plot in Figure 4.4. The horizontal axes are the controlled frequency and controlled acoustic pressure amplitude, and the vertical axis is the partition coefficient of the acoustically exposed microparticles (as before). The surface has no noticeable peak in the sonicated samples. There is a clear offset between the null and the sonicated samples. The linear regression results support the visual interpretation of the 3D plot. The broader context of these results is discussed further in Subsection 5.1.2.

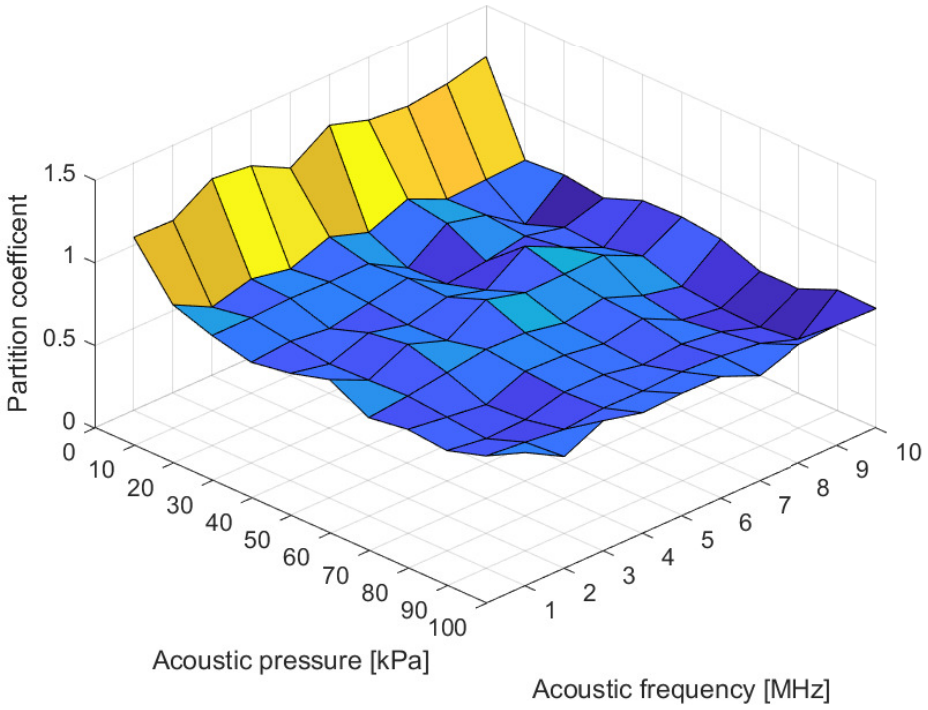

Figure 4.4: The surface plot of the partition coefficients of the microparticles imaged at 5 min vs the controlled acoustic frequency and acoustic pressure amplitude of the acoustic regimes.

Figure description: The yellow surface indicates the comparatively large change in hydrophobicity of the acoustically exposed microparticles compared to the null samples (on the top back edge along an acoustic pressure contour of 0 kPa). The blue surface of the actively exposed samples is relatively flat and consistently below the values of the nulls. The nulls have a mean value of $\log_{10}(P)$ =1.12. The mean of the blue surface is at $\log_{10}(P)$ =0.65.

4.3.3 Results from samples imaged at 7.5 min

The mean partition coefficients calculated with the DIP code from the images taken at 7.5 min, for each controlled variable combination of acoustic frequency and acoustic pressure, is shown in Table 4.7.

The average effect of varying controlled frequencies on the partition coefficient (right column entries of Table 4.7), and the average effect of varying controlled pressures on the partition coefficient (bottom row entries of Table 4.7), are graphed in Figure 4.5a and Figure 4.5b respectively. Each graph includes the average partition coefficient of the null experiment (the bottom left cell of Table 4.7) for comparison, seen explicitly on the y-axis and as a horizontal dotted line.

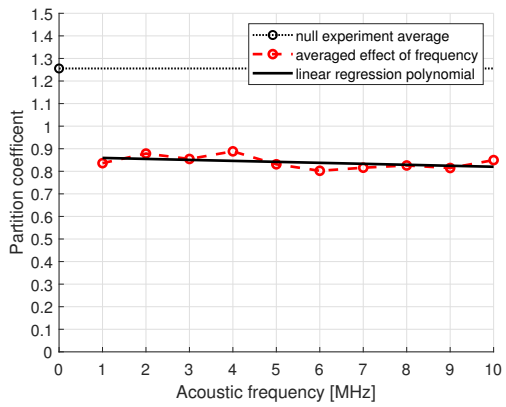

(a) Average effect of the different controlled frequencies

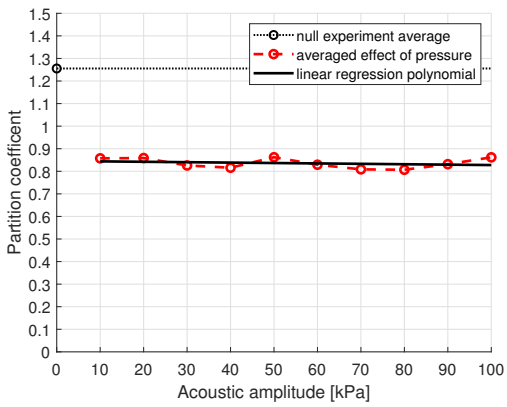

(b) Average effect of the different controlled pressures

Figure 4.5: The averaged effects of the controlled variables on the partition coefficient from images taken at 7.5 min

The graphs are linear and horizontal. Linear regression analysis is performed on each of the averages to evaluate a linear polynomial approximation of the results. The linear polynomials of variable frequency f and pressure p on the partition coefficient $\log_{10}(P)$ is given in Equation 4.5 and Equation 4.6.

$$\log_{10}(P) = -0.0043f + 0.8635 \pm 0.09 \tag{4.5}$$

$$\log_{10}(P) = -0.0002p + 0.8457 \pm 0.09 \tag{4.6}$$

The trend is linear and similar to the results seen in Subsection 4.3.1 and Subsection 4.3.2. The gradients here, although explicitly negative, are still negligible. The acoustic frequency and pressure again have no variation effect on the partition coefficient values, and the data is again only predicted by its mean. However, there is a clear and diccernable difference between these results and the results of the 2.5 min and 5 min results (which were similar to each other). Here, the means of the sonicated samples is 0.84 ± 0.09. Compared with the mean of the sonicated samples measured previously, 0.63 ± 0.10 and 0.65 ± 0.13, there is an apparent increase in the measured partition value. This increase cannot be attributed to the statistical error and standard deviation, or at least not strongly. The previous two set measurements are well within their standard deviations. However, the value measured here for this 7.5 min data set is at least 1.46σ away from the other two sets.

Finally, the measured partition coefficient values between the sonicated and null samples for this 7.5 min data are compared with each other. The values of the sonicated and null samples are 0.84 ± 0.09 and 1.26 ± 0.15 respectively. These values are again different from one another. However, the standard deviation separation of $\sigma = 2.8$ is less compared to the previous results. Table 4.7 is seen on the next page.

Table 4.7: Mean partition coefficients of the microparticles reshaken and imaged at 7.5 min for all controlled acoustic frequencies and standard pressure amplitudes

		(null)	Acoustic Pressure [kPa]										Frequency
		0	10	20	30	40	50	60	70	80	90	100	Averages
Acoustic Frequency [MHz]	1	1.19±0.05	0.81±0.08	0.81±0.16	0.79±0.13	0.85±0.12	0.82±0.08	0.81±0.08	0.82±0.05	0.81±0.12	0.85±0.04	0.98±0.12	0.84±0.10
	2	1.24±0.20	0.87±0.04	0.94±0.12	0.92±0.09	0.83±0.10	0.88±0.11	0.87±0.04	0.92±0.03	0.83±0.07	0.84±0.05	0.88±0.08	0.88±0.08
	3	1.42±0.18	0.94±0.06	0.95±0.04	0.81±0.04	0.82±0.06	0.85±0.06	0.82±0.03	0.80±0.07	0.78±0.07	0.82±0.08	0.95±0.03	0.85±0.06
	4	1.31±0.12	0.96±0.11	0.87±0.08	0.84±0.12	0.84±0.13	0.92±0.12	0.91±0.13	0.88±0.13	0.90±0.11	0.89±0.09	0.87±0.18	0.89±0.12
	5	1.17±0.13	0.86±0.08	0.83±0.08	0.86±0.08	0.80±0.11	0.87±0.03	0.84±0.08	0.77±0.05	0.81±0.05	0.86±0.03	0.87±0.10	0.84±0.07
	6	1.26±0.13	0.83±0.11	0.81±0.08	0.71±0.07	0.74±0.07	0.81±0.18	0.82±0.18	0.73±0.15	0.72±0.06	0.77±0.09	0.84±0.17	0.78±0.13
	7	1.20±0.16	0.85±0.06	0.83±0.04	0.77±0.07	0.75±0.05	0.80±0.10	0.81±0.04	0.80±0.12	0.86±0.11	0.81±0.05	0.82±0.08	0.81±0.08
	8	1.29±0.13	0.85±0.13	0.85±0.14	0.84±0.11	0.81±0.11	0.85±0.11	0.78±0.05	0.75±0.07	0.78±0.06	0.79±0.09	0.86±0.13	0.82±0.10
	9	1.26±0.14	0.82±0.07	0.74±0.00	0.86±0.00	0.89±0.00	1.04±0.00	0.72±0.00	0.73±0.00	0.68±0.00	0.78±0.00	0.87±0.09	0.81±0.04
	10	1.29±0.18	0.86±0.14	0.90±0.07	0.88±0.06	0.89±0.06	0.93±0.10	0.85±0.07	0.84±0.06	0.82±0.05	0.87±0.06	0.82±0.08	0.87±0.08
Pressure Averages		1.26±0.15	0.87±0.09	0.85±0.09	0.83±0.09	0.82±0.09	0.88±0.10	0.82±0.09	0.80±0.09	0.80±0.08	0.83±0.06	0.88±0.11	0.84±0.09

For visualisation, the results of this image set are presented as 3D surface plot in Figure 4.6. The horizontal axes are the controlled frequency and controlled acoustic pressure amplitude, and the vertical axis is the partition coefficient of the acoustically exposed microparticles. Again, and consistent with the previous results, there is no peak or outlier in the sonicated samples. The nulls produce a clear ridge and different value compared to all the sonicated samples. The broader context of these results are covered in Subsection 5.1.3.

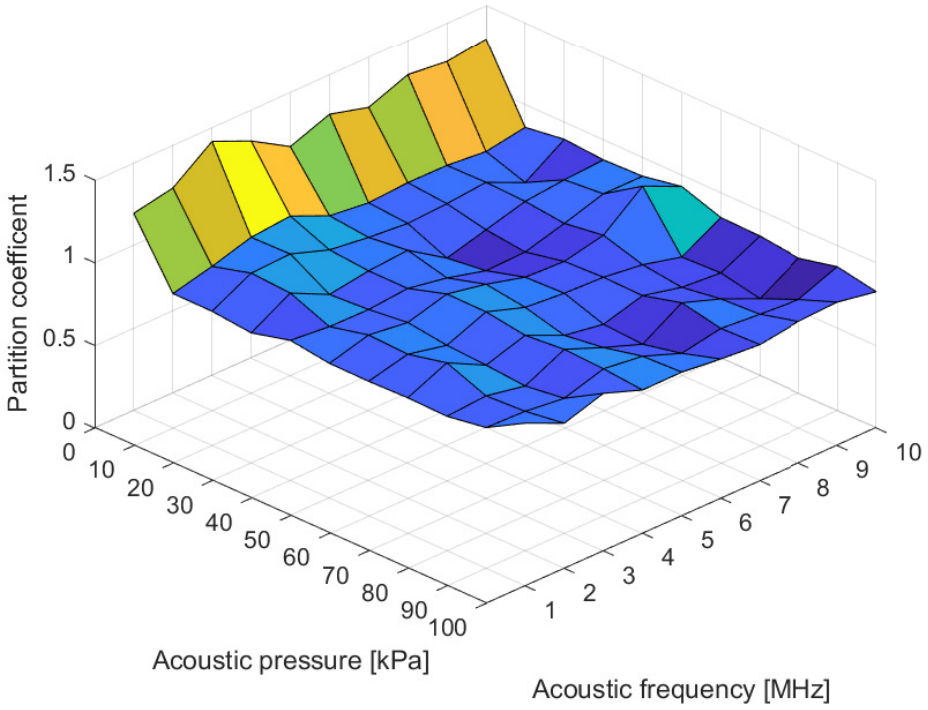

Figure 4.6: The surface plot of the partition coefficients of the microparticles, reshaken at 5 min and imaged at 7.5 min vs the controlled acoustic frequency and acoustic pressure amplitude of the acoustic regimes.

Figure description: The yellow gradient surface indicates the comparatively large change in hydrophobicity compared to the null samples (on the top back edge along an acoustic pressure contour of 0 kPa). The blue surface of the actively exposed samples is relatively flat and consistently below the values of the nulls. The nulls have a mean value of $\log_{10}(P)$ =1.26. The mean of the blue surface is at $\log_{10}(P)$ =0.83.

4.4 Experimental results of the extended pressure range

The results of the experiments of the extended acoustic pressure amplitudes for selected acoustic frequencies are presented below. The results are grouped according to the experimental imaging times 2.5 min, 5 min and 7.5 min, similarly to Section 4.3. The data are tabled according to these corresponding imaging times and sections.

A brief recap on the procedure of statistical analysis is now covered. Each sample point of acoustic frequency and pressure has five measured partition coefficients (all the nulls compound, thus having more total samples). The mean partition coefficient is calculated for each sample point and tabulated with their respective standard deviation. The results of the sonicated samples are combined along constant frequency contours and separately along constant pressure contours. This generates an average result along these contours, with the frequency contour averages in the right-most column and pressure contour averages in the bottom-most row. This individually isolates the average effect of frequency and pressure for linear regression analysis. The overall mean is also provided in the bottom-right cell of the table.

However, the tables have data points that are not filled due to the experimental procedure and limits on the transducer. Thus the constant pressure contours are not all represented by the same number of sample points. The lack of these points is compensated for by adjusting the mean and standard deviation to their relevant weighted equivalents. The same weighted average standard deviation is used as discussed and seen in Section 3.6, with the relevant n_i weighting. Lastly, the mean of the null samples is seen in the bottom-left cell of the tables.

As will be seen, the averages still follow a linear trend, similar to the standard pressure range results seen above in Section 4.3. The effects of the isolated frequency and pressure changes on the partition coefficient are quantified with linear regression equations, of the form seen in Section 3.6.

Additionally, the 3D bi-variate surface plot of the partition coefficient is also generated. However, here the surface is represented slightly differently. The pressures here extend across two orders of magnitude; therefore, the pressure axis is on a logarithmic scale.

This allows for better viewing of the difference in the order of magnitude between the low pressure to the higher pressure results. However, this also artificially removes the null samples from the surface (as they are at $-\infty$). The comparison to the null samples is thus implicit on the surface plot, and caution must be exercised in its interpretation.

4.4.1 Results from the extended pressure range samples imaged at 2.5 min

The mean partition coefficients calculated with the DIP code from the images taken at 2.5 min, for each controlled variable combination of acoustic frequency and acoustic pressure, is shown in Table 4.8.

The average effect of varying controlled frequencies on the partition coefficient (right column entries of Table 4.8), and the average effect of varying controlled pressures on the partition coefficient (bottom row entries of Table 4.8), are graphed in Figure 4.7a and Figure 4.7b respectively. Each graph includes the average partition coefficient of the null experiment (the bottom-left cell of Table 4.8) for comparsion, seen explicitly on the y-axis and as a horizontal dotted line. Note that the pressure graph is plotted on a semi-logarithmic x-axis. The smallest and largest pressures from the standard range, 10 kPa and 100 kPa, are directly adopted here for continuity and comparison.

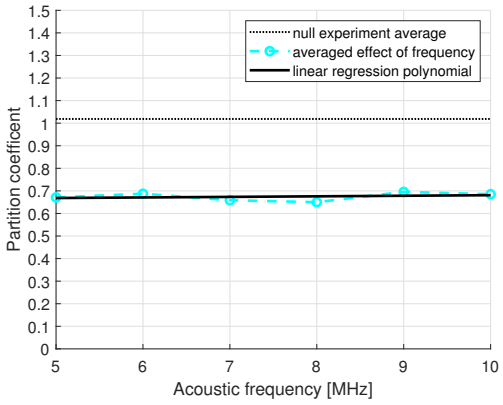

(a) Average effect of the different controlled frequencies

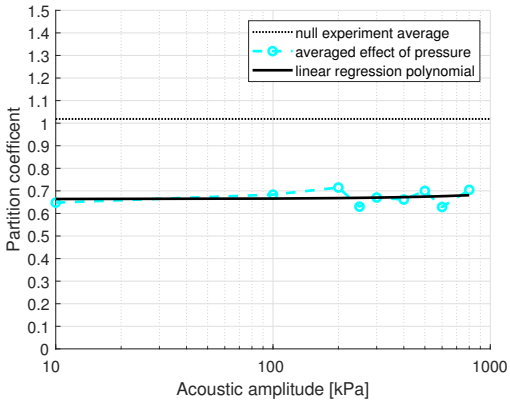

(b) Average effect of the different controlled pressures

Figure 4.7: The averaged effects of the controlled variables on the partition coefficient from images taken at 2.5 min for the extended pressure range.

Figure description: The average effect of the different controlled pressures is graphed on a logarithmic scale to show more easily the widely distributed experimental control pressures used.

The graphs have a general horizontal linear shape. Linear regression analysis is performed on each of the averages to evaluate a linear polynomial approximation of the results. The linear polynomials of variable frequency f and pressure p on the partition coefficient $\log_{10}(P)$ is given in Equation 4.7 and Equation 4.8 respectively.

$$\log_{10}(P) = 0.0025f + 0.6559 \pm 0.10 \tag{4.7}$$

$$\log_{10}(P) = 0.0000p + 0.6638 \pm 0.10 \tag{4.8}$$

The trend is clearly linear for both. The mean value of the sonicated samples is 0.67 ± 0.10 and the mean of the null samples is 1.02 ± 0.13. The gradients are clearly negligible in comparison to the mean, and the values are separated by at least 2.69σ. Table 4.8 is seen on the next page.

Table 4.8: Mean partition coefficients of the microparticles imaged at 2.5 min for all controlled acoustic frequencies and extended pressure amplitudes

		null	Acoustic Pressure [kPa]									Frequency
		0	10	100	200	250	300	400	500	600	800	Averages
Frequency [MHz]	5	0.95 ±0.06	0.65 ±0.07	0.73 ±0.09	0.76 ±0.05	0.63 ±0.11	0.60 ±0.13	0.66 ±0.06				0.67 ±0.09
	6	1.09 ±0.10	0.65 ±0.10	0.69 ±0.09	0.73 ±0.08		0.68 ±0.07	0.66 ±0.12	0.71 ±0.09			0.69 ±0.10
	7	0.96 ±0.19	0.66 ±0.12	0.63 ±0.06	0.69 ±0.08			0.67 ±0.06		0.62 ±0.10	0.68 ±0.09	0.66 ±0.09
	8	0.99 ±0.10	0.63 ±0.14	0.67 ±0.08	0.69 ±0.08			0.61 ±0.11		0.61 ±0.10	0.68 ±0.10	0.65 ±0.10
	9	1.08 ±0.12	0.65 ±0.06	0.72 ±0.08	0.70 ±0.06			0.69 ±0.10		0.66 ±0.12	0.75 ±0.14	0.70 ±0.10
	10	1.05 ±0.19	0.64 ±0.09	0.67 ±0.08	0.72 ±0.03		0.72 ±0.10	0.67 ±0.14	0.69 ±0.12			0.69 ±0.10
Pressure Averages		1.02 ±0.13	0.65 ±0.10	0.68 ±0.08	0.71 ±0.07	0.63 ±0.11	0.67 ±0.10	0.66 ±0.10	0.70 ±0.11	0.63 ±0.10	0.70 ±0.11	0.67 ±0.10

For visualisation, the results of this image set are presented as a 3D surface plot in Figure 4.10. The horizontal axes are the controlled frequency and controlled acoustic pressure amplitude. The vertical axis is the partition coefficient of the acoustically exposed microparticles. The controlled acoustic pressure amplitude axis is a logarithmic scale to show the full extent of the pressures more practically, as discussed previously. For this reason, the null experiments at 0 kPa are not shown (since they are at $-\infty$ as mentioned before). The surface plot indicates no prominent peaks that were averaged out by the linear regression analysis methods. These results are discussed firther and in a broader context in Subsection 5.1.1

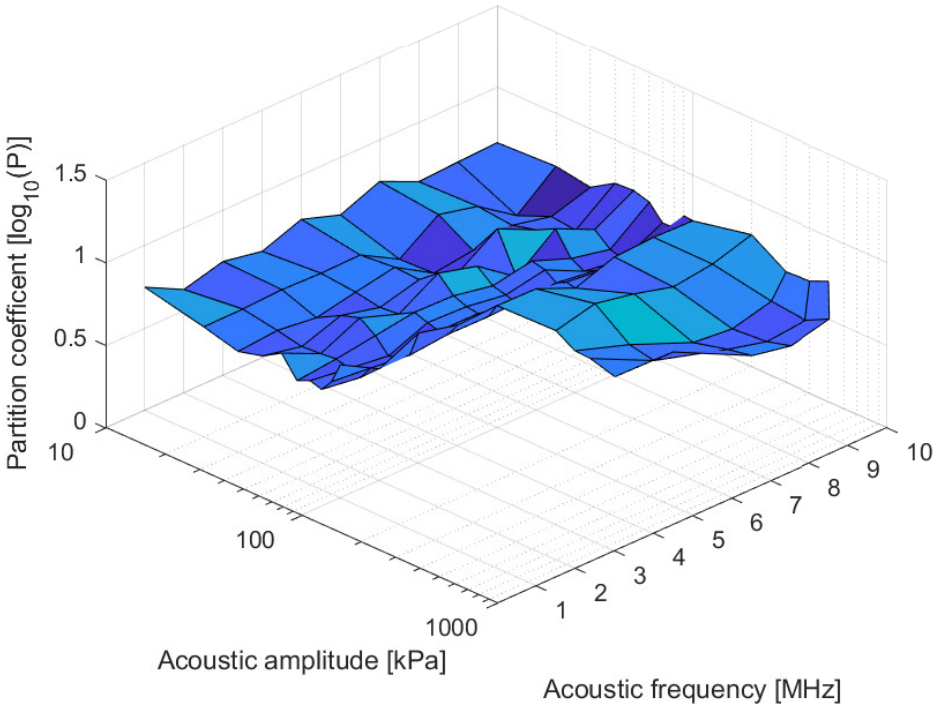

Figure 4.8: The surface plot of the partition coefficients of the microparticles imaged at 2.5 min vs the controlled acoustic frequency and acoustic pressure amplitude of the extended pressure range experiments.

Figure description: The blue surface of the actively exposed samples is relatively flat and consistently below the values of the nulls (not seen in the graph, have a mean value of $\log_{10}(P)$ =1.02). The mean of the blue surface for the extended pressure range only is at $\log_{10}(P)$ =0.67.

4.4.2 Results from the extended pressure range samples imaged at 5 min

The mean partition coefficients calculated with the DIP code from the images taken at 5 min, for each controlled variable combination of acoustic frequency and acoustic pressure, is shown in Table 4.9. The structure of how the results are presented is similar to Subsection 4.4.1.

The average effect of varying controlled frequencies on the partition coefficient (right column entries of Table 4.9), and the average effect of varying controlled pressures on the partition coefficient (bottom row entries of Table 4.9), are graphed in Figure 4.9a and Figure 4.9b respectively. Each graph includes the average partition coefficient of the null experiment (the bottom-left cell of Table 4.9) for comparsion, seen explicitly on the y-axis and as a horizontal dotted line. Note the pressure graph is plotted on a semi-log x-axis. The smallest and largest pressures from the standard range, 10 kPa and 100 kPa, are directly adopted here for continuity and comparison.

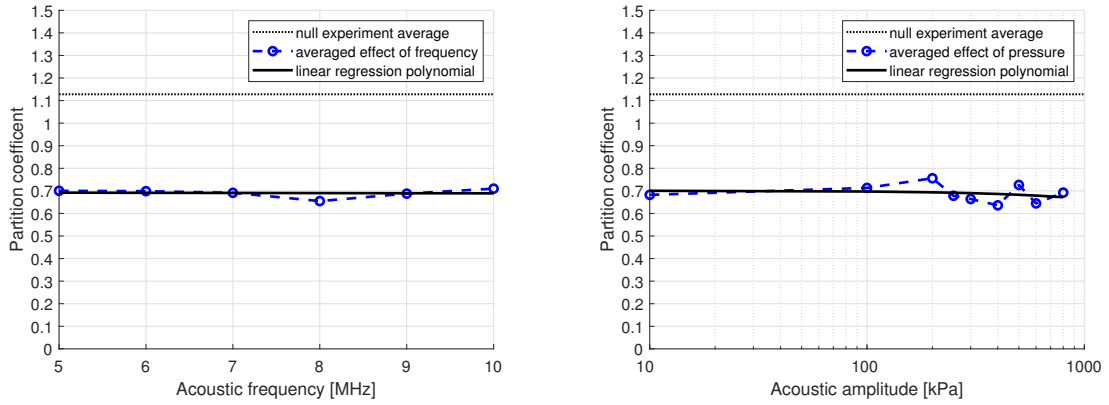

(a) Average effect of the different controlled frequencies

(b) Average effect of the different controlled pressures

Figure 4.9: The averaged effects of the controlled variables on the partition coefficient from images taken at 5 min for the extended pressure range.

Figure description: The average effect of the different controlled pressures is graphed on a logarithmic scale to show more easily the widely distributed experimental control pressures used.

The graphs have a linear and horizontal shape. Linear regression analysis is performed on each of the averages to evaluate a linear polynomial approximation of the results. The linear polynomials of variable frequency f and pressure p on the partition coefficient $\log_{10}(P)$ is given in Equation 4.9 and Equation 4.10.

$$\log_{10}(P) = -0.0006f + 0.6951 \pm 0.10 \tag{4.9}$$

$$\log_{10}(P) = -0.0000p + 0.7007 \pm 0.10 \tag{4.10}$$

The trend is linear for both. The gradients are again negligible in comparison to the mean. Therefore the data is mean-dominated, and the variation in frequency and pressure do not contribute meaningfully to any change in the partition coefficient. The total mean of the sonicated samples is 0.69 ± 0.10 and the mean of the null samples is 1.13 ± 0.15. The difference between the null and sonicated samples cannot be attributed to any statistical phenomenon, as the relative difference is at least 2.93σ. Table 4.9 is seen on the next page.

Table 4.9: Mean partition coefficients of the microparticles imaged at 5 min for all controlled acoustic frequencies and extended pressure amplitudes

		null	Acoustic Pressure [kPa]									Frequency
		0	10	100	200	250	300	400	500	600	800	Averages
Frequency [MHz]	5	1.04 ±0.17	0.73 ±0.15	0.74 ±0.11	0.75 ±0.07	0.68 ±0.11	0.67 ±0.08	0.63 ±0.06				0.70 ±0.10
	6	1.20 ±0.11	0.65 ±0.14	0.74 ±0.13	0.81 ±0.11		0.65 ±0.04	0.62 ±0.08	0.72 ±0.10			0.70 ±0.11
	7	1.12 ±0.19	0.75 ±0.14	0.63 ±0.16	0.76 ±0.05			0.62 ±0.05		0.68 ±0.13	0.70 ±0.06	0.69 ±0.11
	8	1.10 ±0.15	0.64 ±0.13	0.72 ±0.13	0.70 ±0.08			0.60 ±0.08		0.62 ±0.06	0.66 ±0.05	0.65 ±0.09
	9	1.13 ±0.12	0.65 ±0.07	0.73 ±0.11	0.73 ±0.09			0.66 ±0.08		0.64 ±0.07	0.71 ±0.08	0.69 ±0.08
	10	1.19 ±0.16	0.67 ±0.10	0.72 ±0.09	0.80 ±0.07		0.67 ±0.04	0.68 ±0.09	0.73 ±0.06			0.71 ±0.08
Pressure Averages		1.13 ±0.15	0.68 ±0.12	0.71 ±0.12	0.76 ±0.08	0.68 ±0.11	0.66 ±0.06	0.64 ±0.07	0.73 ±0.08	0.64 ±0.09	0.69 ±0.06	0.69 ±0.10

For visualisation, the results of this image set are presented as a 3D surface plot in Figure 4.10. The horizontal axes are the controlled frequency and controlled acoustic pressure amplitude. The vertical axis is the partition coefficient of the acoustically exposed microparticles. The controlled acoustic pressure amplitude axis is a logarithmic scale to show the full extent of the pressures more practically. For this reason, the null experiments at 0 kPa are not shown (since they are at $-\infty$, as mentioned previously). Again, there are no noticeable peaks or outliers on the surface. These results are discussed firther and in a broader context in Subsection 5.1.2.

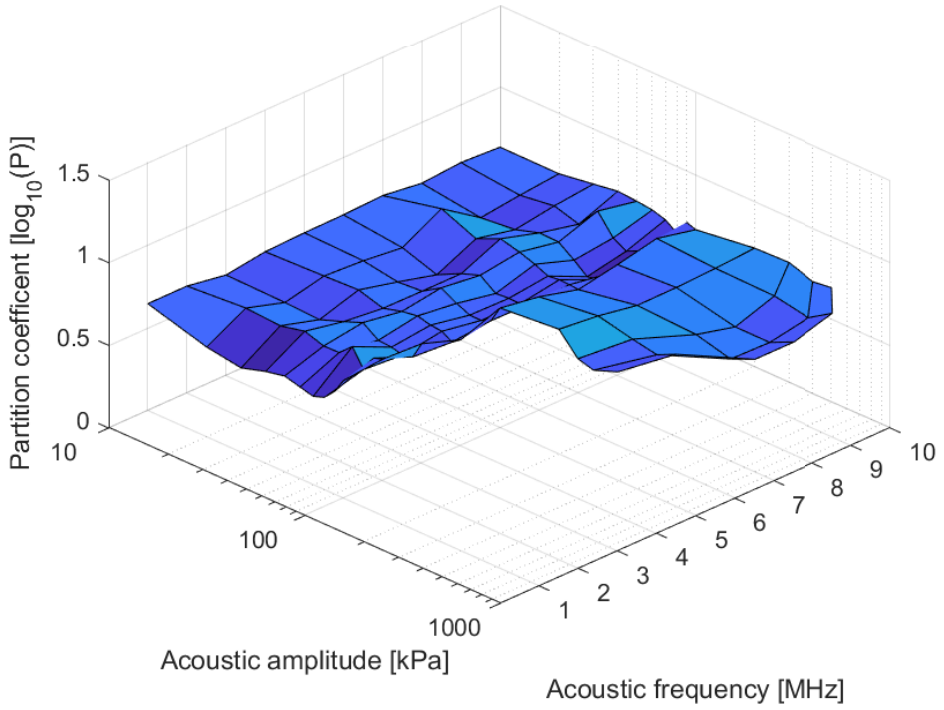

Figure 4.10: The surface plot of the partition coefficients of the microparticles imaged at 5 min vs the controlled acoustic frequency and acoustic pressure amplitude of the extended pressure range experiments.

Figure description: The blue surface of the actively exposed samples is relatively flat and consistently below the values of the nulls (not seen in the graph, have a mean value of $\log_{10}(P)$ =1.13). The mean of the blue surface for the extended pressure range only is at $\log_{10}(P)$ =0.69.

4.4.3 Results from the extended pressure range samples imaged at 7.5 min

The mean partition coefficients calculated with the DIP code from the images taken at 7.5 min, for each controlled variable combination of acoustic frequency and acoustic pressure, is shown in Table 4.10. The structure of how the results are presented is similar to Subsection 4.4.1.

The average effect of varying controlled frequencies on the partition coefficient (right column entries of Table 4.10), and the average effect of varying controlled pressures on the partition coefficient (bottom row entries of Table 4.10), are graphed in Figure 4.11a and Figure 4.11b respectively. Each graph includes the average partition coefficient of the null experiment (the bottom-left cell of Table 4.10) for comparsion, seen explicitly on the y-axis and as a horizontal dotted line. Note the pressure graph is plotted on a semi-log x-axis. The smallest and largest pressures from the standard range, 10 kPa and 100 kPa, are directly adopted here for continuity and comparison.

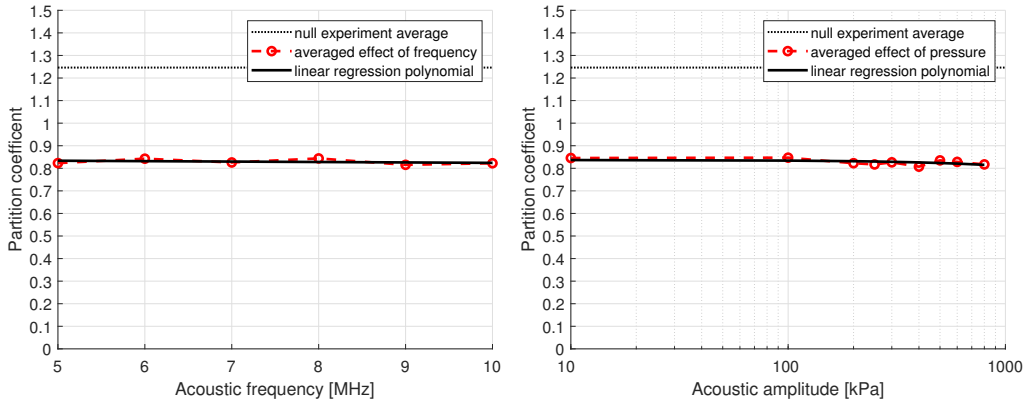

(a) Average effect of the different controlled frequencies

(b) Average effect of the different controlled pressures

Figure 4.11: The averaged effects of the controlled variables on the partition coefficient from images taken at 7.5 min for the extended pressure range.

Figure description: The average effect of the different controlled pressures is graphed on a logarithmic scale to show more easily the widely distributed experimental control pressures used.

The graphs are linear and horizontal. Linear regression analysis is performed on each of the averages to evaluate a linear polynomial approximation of the results. The linear polynomials of variable frequency f and pressure p on the partition coefficient $\log_{10}(P)$ is given in Equation 4.11 and Equation 4.12.

$$\log_{10}(P) = -0.0019f + 0.8431 \pm 0.11 \tag{4.11}$$

$$\log_{10}(P) = -0.0000p + 0.8368 \pm 0.11 \tag{4.12}$$

The regression clearly shows the data is mean-dominated again. Although the gradients here are explicitly negative, they are negligible in both frequency and pressure on the measured partition coefficient values. The mean of the sonicated samples is 0.83 ± 0.11 and the mean of the null samples is 1.25 ± 0.15. The means are also relatively separated by 2.8σ and again cannot be accounted for pure statistical variance and are distinct. The only difference is in the comparison of the sonicated sample's partition coefficient with those from Subsection 4.4.1 and Subsection 4.4.2.

The means of the sonicated samples are clearly different. Respectively, they are 0.67 ± 0.10, 0.69 ± 0.10 and 0.83 ± 0.11. The previous two values are almost identical and are well within their statistical deviations. However, they are both noticeably different from the result here, with a difference of at least 1.45σ. The null samples across the different imaging-time sets are comparable and within their standard deviations. Table 4.10 is seen on the next page.

Table 4.10: Mean partition coefficients of the microparticles reshaken and imaged at 7.5 min for all controlled acoustic frequencies and extended pressure amplitudes

		null	Acoustic Pressure [kPa]									Frequency
		0	10	100	200	250	300	400	500	600	800	Averages
Frequency [MHz]	5	1.17 ±0.13	0.86 ±0.08	0.87 ±0.10	0.80 ±0.09	0.82 ±0.06	0.81 ±0.07	0.79 ±0.08				0.82 ±0.08
	6	1.26 ±0.13	0.83 ±0.11	0.84 ±0.17	0.82 ±0.12		0.87 ±0.13	0.83 ±0.11	0.86 ±0.13			0.84 ±0.13
	7	1.20 ±0.16	0.85 ±0.06	0.82 ±0.08	0.82 ±0.17			0.81 ±0.15		0.84 ±0.11	0.81 ±0.08	0.83 ±0.12
	8	1.29 ±0.13	0.85 ±0.13	0.86 ±0.13	0.84 ±0.02			0.84 ±0.12		0.87 ±0.14	0.82 ±0.10	0.84 ±0.11
	9	1.26 ±0.14	0.82 ±0.07	0.87 ±0.09	0.80 ±0.10			0.80 ±0.07		0.78 ±0.11	0.82 ±0.10	0.82 ±0.09
	10	1.29 ±0.18	0.86 ±0.14	0.82 ±0.08	0.86 ±0.11		0.80 ±0.06	0.78 ±0.07	0.81 ±0.07			0.82 ±0.09
Pressure Averages		1.25 ±0.15	0.85 ±0.10	0.85 ±0.11	0.82 ±0.11	0.82 ±0.06	0.83 ±0.09	0.81 ±0.10	0.84 ±0.10	0.83 ±0.12	0.82 ±0.09	0.83 ±0.11

For visualisation, the results of this image set are presented as a 3D surface plot in Figure 4.12. The horizontal axes are the controlled frequency and controlled acoustic pressure amplitude. The vertical axis is the partition coefficient of the acoustically exposed microparticles. The controlled acoustic pressure amplitude axis is a logarithmic scale to show the full extent of the pressures more practically. For this reason, the null experiments at 0 kPa are not shown (since they are at $-\infty$). Again, there is no peak or outlier in the surface plot. The results are further contexutalised in Subsection 5.1.3.

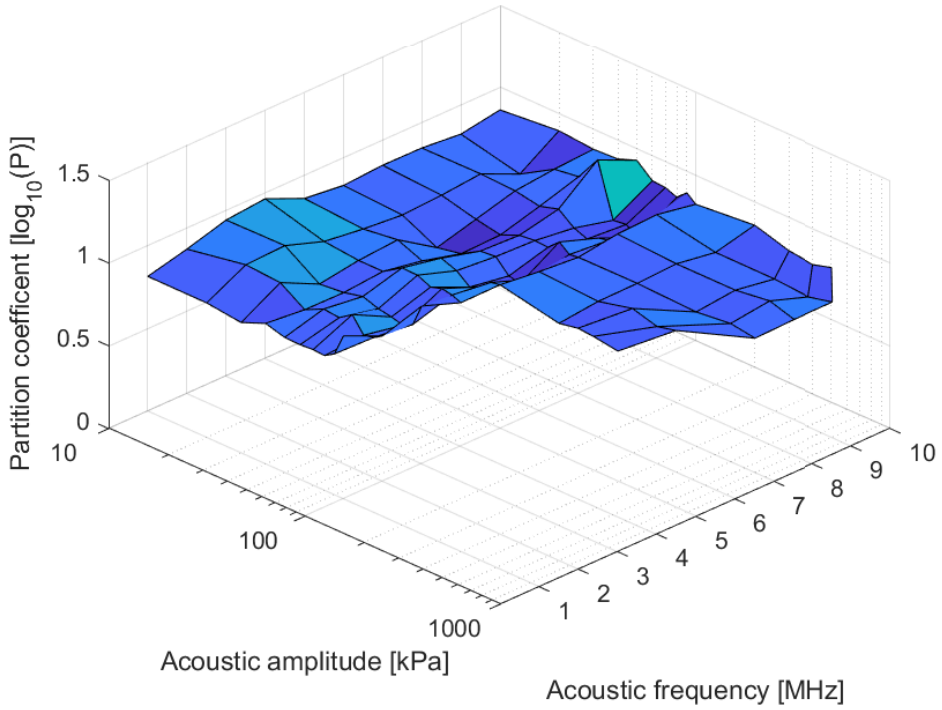

Figure 4.12: The surface plot of the partition coefficients of the microparticles, reshaken at 5 min and imaged at 2.5 min vs the controlled acoustic frequency and acoustic pressure amplitude of the extended pressure range experiments.

Figure description: The blue surface of the actively exposed samples is relatively flat and consistently below the values of the nulls (not seen in the graph). The nulls have a mean value of $\log_{10}(P)$ =1.25. The mean of the blue surface for the extended pressure range only is at $\log_{10}(P)$ =0.83.

4.5 Summary

The results of the experiments are presented in the above sections. The results are separated into the standard and extended pressure ranges and into chronological order of the imaging times. These are 2.5 min, 5 min and 7.5 min. Comparison between these times' results is used to quantify the time stability of any change in the partition coefficients of hydrophobic microparticles caused by ultrasound. The regression gradients of the frequency- and pressure-dependent partition coefficient functions are approximately zero. The data for all the sonicated hydrophobic microparticles are only predicted by their mean. The mean of the sonicated samples is also quantifiably different from that of the null samples.

The difference is statistically significant with a standard deviation of about $\approx 3\sigma$ across all the results. Additionally, there is a quantifiable change in the samples measured at 7.5 min for both the standard and extended pressure ranges. This difference is $\approx 1.5\sigma$ between both the 2.5 min and 5 min groups, and the 7.5 min group (which are images of the samples after manual reshaking at 5 min). The results clearly indicate an overall effect of ultrasound on the hydrophobicity of microparticles from a statistical analysis viewpoint. The underlying reasons for this in the context of these results are discussed further in Chapter 5. The average results from each pressure range and subsequent imaging times can be seen in Table 4.11.

Table 4.11: Average partition coefficient values for all experimental categories

(a) Standard pressure range 10 kPa to 100 kPa (1 MHz to 10 MHz)

	partition coefficients	
image time	null samples	sonicated samples
2.5 min	1.05±0.13	0.63±0.10
5 min	1.12±0.15	0.65±0.13
7.5 min	1.26±0.15	0.84±0.09

(b) Extended pressure range 100 kPa to 800 kPa (5 MHz to 10 MHz)

	partition coefficients	
image time	null samples	sonicated samples
2.5 min	1.02±0.13	0.67±0.10
5 min	1.13±0.15	0.69±0.10
7.5 min	1.25±0.15	0.83±0.11

Chapter 5

Discussion on results

The results were previously provided as is, with very little explanation or comparison between them. In this chapter, the results are more holistically compared. First, the experimental results from subsets are unpacked further in terms of what is being implied. A comparison of the pressure range subset is then given.

The technical aspects of this research are also drawn to a close. The objectives are restated, and the results are contextualised to indicate these objectives' completion. Following this, the research question is restated and finally answered. A general discussion on the interpretation of the results and the implicit findings are unpacked further.

5.1 Results overview

For the convenience of the discussion herein, the results from the standard and extended pressure sets are combined for each imaging time. There is no significant difference in the results between the standard and extended pressure range sets. However, there is a worthwhile discussion on the relative comparison between each of the imaging times results'. The specific case outcome of the linear regression analysis from Table 3.3 is also discussed.

5.1.1 Results from the 2.5 min imaging time

The partition coefficient of the null sample is 1.05 ± 0.13 (and 1.02 ± 0.13 for the extended pressure set, with negligible difference). The mean of the exposed samples is 0.63 ± 0.10 (and 0.67 ± 0.10 for the extended pressure set). The statistical regression parameters for frequency and pressure are $\log_{10}(P) = 0.0040f + 0.6224 \pm 0.10$ and $\log_{10}(P) = 0.0001p + 0.6279 \pm 0.10$ for the standard pressure range. The extended pressure range parameters are $\log_{10}(P) = 0.0025f + 0.6559 \pm 0.10$ and $\log_{10}(P) = 0.0000p + 0.6638 \pm 0.10$. It is noted that these parameters are slightly different; however, they are well within 1σ of each other and, therefore, negligible.

The gradients are approximately zero, and thus the change in each of these parameters does not have any change in the change in magnitude of the microparticle hydrophobicity. The mean of the sonicated samples is also comparable to the y-intercept of the regression equations. The null mean is clearly different to both of these values and separated by approximately 3σ, which is statistically significant. This analysis outcome fits best with the third case of Table 3.3. This is true for both frequency and pressure. Therefore, ultrasound does induce an overall change in microparticle hydrophobicity, but the change is not linked to the acoustic frequency and pressure of the field. Instead, the effect is through some unknown parameter of ultrasound.

The premise of this research was based on qualitative observation from previous literature. These results already clarify this research's attempt to quantify the change. The qualitative observations were based both on bulk suspension observations and observations on nucleation itself. The bulk observations are verified. The link to nucleation can only be implied from these results and is covered in Section 5.3.

5.1.2 Results from the 5 min imaging time

In a similar vein to the 2.5 min results, the results from the 5 min images share the same story. To recap, the mean partition coefficient of the null samples is 1.12 ± 0.15 (1.13 ± 0.15 for the extended pressure range) and the sonicated samples is 0.65 ± 0.13 (0.69 ± 0.10 for the extended pressure range). The statistical regression parameters for frequency and

pressure are $\log_{10}(P) = 0.0008f + 0.6561 \pm 0.13$ and $\log_{10}(P) = 0.0000p + 0.6496 \pm 0.13$. The extended pressure range parameters are $\log_{10}(P) = -0.0006f + 0.6951 \pm 0.10$ and $\log_{10}(P) = -0.0000p + 0.7007 \pm 0.10$.

The gradients are approximately zero. The sonicated samples' mean is comparable to the regression analysis y-intercept. Therefore the data is only predicted by its mean. The mean is different to that of the null mean and separated by approximately 3σ as well. The third case of Table 3.3 best describes the regression analysis outcome. This is true for both frequency and pressure. The change is comparable to the values from the 2.5 min results. Importantly this means that the change in hydrophobicity is time-stable for the total 5 min time interval. Additionally, the same conclusion is drawn. Ultrasound affects microparticle hydrophobicity through an unknown parameter

This observation needs to be contextualised with the known acoustic behaviour of hydrophobic microparticles. Importantly why, after exposure, the particles maintain their hydrophobicity. This finding fundamentally needs to be linked with the known phenomenon of acoustic nucleation of microparticles. Importantly the process of nucleation changes the state of the microparticle hydrophobicity. This is distinguished from the presence and subsequent absence during and after ultrasound exposure. These details are unpacked further in Section 5.3.

5.1.3 Results imaged at 7.5 min

The results imaged at 7.5 min show an important result on the stability of the change in hydrophobicity. These samples were reshaken at 5 min and then image at 7.5 min. The partition coefficient measured was 0.84 ± 0.09 (0.83 ± 0.11 for the extended pressure range). The regression parameters for frequency and pressure are $\log_{10}(P) = -0.0043f + 0.8635 \pm 0.09$ and $\log_{10}(P) = -0.0002p + 0.8457 \pm 0.09$. The extended pressure range parameters are $\log_{10}(P) = -0.0019f + 0.8431 \pm 0.11$ and $\log_{10}(P) = -0.0000p + 0.8368 \pm 0.11$ The parameters again indicate no relation between frequency and pressure on the magnitude of the change, and the third case of Table 3.3 best describes the regression analysis outcome. This is consistent with the other two conclusions drawn from the regression analysis outcomes.

However, the relative change in the sonicated partition coefficients after reshaking is self-evident. The sonicated samples' mean of the 2.5 min and 5 min results, and the 7.5 min results here, are separated by approximately 1.5σ. This separation means that the change in microparticle hydrophobicity caused by ultrasound is to some degree reversible, at least through the action of reshaking. This, again, needs to be linked to the acoustics of nucleation. Specifically, the act of reshaking causes some recovery process on nucleation and the acoustic effect of nucleation related to hydrophobicity. Ultrasound is a form of mechanical disturbance and can be similarly categorised with the act of reshaking the samples. The question then is, what is specifically different between ultrasound and the act of manual reshaking?

How are these two processes different regarding their effect on nucleation? The fact is that the reshaking is quite violent in that it completely mixes the air and the partitioning liquids in the sample cuvettes, whereas the ultrasound did not. Additionally, manual reshaking is of a significantly lower, even negligible, frequency compared to the ultrasound frequencies used. Therefore there is something inherently different between these two processes. It is unclear whether ultrasound can be used to reverse the effect if it were to have parameters that exhibit similar mixing behaviour. These differences are further discussed in Section 5.3.

5.1.4 Results summary

Collectively, the results from the standard pressure range indicate one core conclusion. Ultrasound does affect the hydrophobicity of microparticles. This finding is consistent with recent literature. The caveat is that the parameters of ultrasound that were investigated in this research, frequency and pressure, did not appreciably affect the magnitude of this change. More specifically, this is for the acoustic pressure range 10 kPa to 100 kPa (in steps of 10 kPa) and the frequencies 1 MHz to 10 MHz (in steps of 1 MHz) investigated. It is indicated that another uninvestigated parameter of ultrasound affects microparticle hydrophobicity.

This is significant in the context of the existing literature. The results here support and are supported by the previous literature, particularly on the nucleation of hydrophobic

microparticles. This means the nucleation phenomenon and the acoustics of nucleation can be directly compared with the quantified change measured here. The fundamental acoustic behaviour of a hydrophobic microparticle can be linked to the change in hydrophobicity. Specifically, the resonant frequency of microparticles, the primary and secondary radiation forces, and the duration of exposure are all linked to the nucleation. Therefore these are linked to the measured hydrophobicity.

The core questions that need to be unpacked and answered are; Why do these results indicate no causal relationship to the frequency and pressure parameters investigated, besides the constant relative change? What is the possible "unknown" parameter that causes this constant relative change? How is this reconciled with the stability and recovery processes? This is unpacked further in the general discussion in Section 5.3.

5.2 Research outcomes

5.2.1 To objective 1: The effect of ultrasound acoustic frequency on microparticle hydrophobicity

The dependence of microparticle hydrophobicity on ultrasound acoustic frequency can be directly inferred from the linear regressions in the results. All of the averaged partition coefficients over contours of constant frequency were not strongly correlated with the controlled frequency. This is indicated by the gradients of the linear regression polynomials. The gradients of all experimental sets are considerably small, in the order of ± 0.01. This is expected as the data are relatively flat. Therefore, the variation in frequencies between 1 MHz to 10 MHz has no quantifiable effect on the magnitude of the change in microparticle hydrophobicity for hydrophobic carbon black microparticles ($<1\,\mu m$).

5.2.2 To objective 2: The effect of ultrasound acoustic pressure on microparticle hydrophobicity

The dependence of microparticle hydrophobicity on ultrasound acoustic pressure amplitude can also similarly be inferred from the linear regressions of the results. All of the averaged partition coefficients over contours of constant pressure were not strongly correlated with the controlled pressure. The gradients are all considerably small, in the order of ± 0.01 as well. Therefore, the variation in acoustic pressure up to 800 kPa has no quantifiable effect on the magnitude of the change in microparticle hydrophobicity for hydrophobic carbon black microparticles (<1 µm).

5.2.3 To objective 3: The time stability of the change in hydrophobicity

In order to determine the baseline time stability, the samples from the experiments imaged at 2.5 min and 5 min are compared. The comparison of the measured partition coefficients between these two different time intervals indicates the stability of the hydrophobicity. The null samples partition coefficients for the two time intervals are 1.05 and 1.12 with standard deviations of 0.15 and 0.14. These values are accommodated within their standard deviation and thus considered stable through time. This is expected for the null experiment samples. The acoustically exposed samples average partition coefficients at 2.5 min and 5 min are 0.63 ± 0.10 and 0.65 ± 0.13. These values indicate that the partition coefficient did not change over the total 5 min interval. Additionally, these values are significantly different from the null samples with a relative difference of $\approx 3\sigma$.

It is concluded that ultrasound does quantitatively change microparticle hydrophobicity. This change is time-stable over at least a 5 min interval for the sonicated hydrophobic carbon black microparticles (<1 µm).

The stability of the change can also be reset. After 5 min, the samples are reshaken by hand. The null samples have a partition coefficient of 1.26 ± 0.15.This differs from the previous results but is still well within the expected standard deviation. The average partition coefficient of the exposed samples is 0.84 ± 0.09 and 0.83 ± 0.11.This value is outside of the expected deviation from the measurements of the exposed samples above.

Therefore, the act of reshaking the sample can partly recover the hydrophobicity of the microparticles.

5.2.4 Research question

To what extent does ultrasound quantitatively change the hydrophobicity of hydrophobic microparticles?

The research question can finally be answered. Not only is it quantitatively verifiable that ultrasound does cause a change in microparticle hydrophobicity, but there is a decrease of ≈40% in the microparticle hydrophobicity caused by ultrasound. More precisely, the relative difference between the quantified hydrophobicity of the null samples and sonicated samples is $\approx 3\sigma$. This change is statistically significant.

The change is also not permanent, as reshaking of the sonicated samples caused the difference to reduce. The reshaken samples' standard deviation difference is $\approx 1.5\sigma$. This is half the relative standard deviation difference of the originally sonicated samples compared to the null partition coefficient.

5.3 General discussion

The results from this research need to be discussed in the context of the existing research. There is a recap on the important acoustic behaviour of hydrophobic microparticles. The specific parameters of this research follow, with a contextual connection with existing literature. The results from this research are then explained in the context of the acoustic behaviour, the parameters, and existing literature. A discussion on how these results support and are supported by previous literature on hydrophobic microparticle acoustics follows. Finally, the limitations of this research are discussed.

Hydrophobic microparticles behave as acoustically active antibubbles. The incompressible core of antibubbles causes their acoustic behaviour to be highly nonlinear, especially when compared to ordinary microbubbles. The subsequent resonant frequency is much higher,

the radial excursion of the bubble is highly nonlinear, the threshold radius of nucleation is much lower, and the acoustic pressure required to induce these effects is much lower. These nonlinear characteristics result in hydrophobic microparticles nucleating more easily. The explosive nucleation of hydrophobic microparticles leads to the stripping of their gaseous shell. Subsequent renucleation does not occur due to the resulting wetting of the particle. Therefore, the particle is qualitatively observed as having its hydrophobicity changed.

Antibubbles also translate in acoustic fields due to their acoustic activity. A hydrophobic microparticle as an antibubble has an associated resonant frequency (as described by Equation 2.7). If the acoustic frequency is higher than the resonant frequency of the antibubble, then the particle translates to the nodes or away from the acoustic focus. I.e. towards the least dynamic pressure changes in the acoustic field. If the acoustic frequency is lower than the resonant frequency of the antibubble, then the particle translates to the antinodes or towards the acoustic focus. I.e. towards the most dynamic pressure changes in the sound field. The acoustic force on the bubble is from an external sound field and is called the primary radiation force, which spatially translates the microbubble. Antibubbles also attract or repel one another if they are oscillating in phase or antiphase, respectively. This is due to the re-radiation of the antibubble's sound field, called secondary radiation forces.

This research used Zuper Black pigment dispersion. This consists of hydrophobic carbon black microparticles with a size range between 0.2 µm to 1.2 µm. These particles behave as acoustically active antibubbles. Therefore, a microparticle suspension of this pigment experiences all the nonlinear acoustic effects mentioned previously. These carbon black microparticles have the following properties as determined from previous research; their resonant frequency is >15 MHz for 5% and >40 MHz for 95% of the particles, their core to outer radius ratio is 0.8, their nucleation threshold radius ratio is 1.3, their nucleation threshold pressure is at most 200 MPa. Additionally, as with any random distribution of particles in suspension, particles will oscillate in phase or antiphase with the ultrasound field and attract or repel one another due to their relative secondary radiation forces. Therefore, some particles undergo explosive nucleation, while others simply oscillate in antiphase and maintain their gaseous shell. This research investigated the ultrasound parameters of frequency and pressure. The frequencies investigated were 1 MHz to

10 MHz in 1 MHz intervals. The pressure ranges were 0 kPa to 100 kPa in steps of 10 kPa, with selected frequencies having pressures as high as 800 kPa. The available transducers limited these parameters. Samples of suspended hydrophobic microparticles were exposed to these regimes for five minutes. The samples were partitioned under the defined methodology of the octanol-water partition coefficient to quantify the hydrophobicity. The concentration measurements were made using colourimetric digital image processing.

From all the collective results, it is clear that ultrasound does quantitatively change the hydrophobicity of microparticles. The caveat is that the tested frequency and pressure ranges in the scope of this research had no significant nor measurable effect on the magnitude of this change. The underlying question is why? How can ultrasound, simply by its presence, affect microparticle hydrophobicity, but changes in the frequency and pressure parameters do nothing to the magnitude of this change? The answer is hidden in the existing literature on known acoustic effects of microparticles and is unpacked further.

Firstly and most importantly is that a quantifiable change has occurred. This quantitative observation supports the qualitative observation that the microparticle hydrophobicity is changed by ultrasound. The most important parameter and feature of an antibubble that determines its acoustic behaviour is its resonant frequency. I.e. if the ultrasound field is going to do anything to an antibubble, the specific effect is primarily dependent on the relation of the ultrasound frequency and antibubble's resonant frequency. The antibubble resonant frequency highly depends on the microparticle size and subsequent core-to-bubble radius. Looking back at Equation 2.7, this equation's high nonlinearity of the resonant frequency and subsequent antibubble dynamics are dominated by these two parameters. The resonant frequency of the microparticles is >15 MHz, with most >40 MHz.

This resonant frequency is significantly larger than the frequencies investigated here. Therefore, all the particles are expected to move to the antinodes or acoustic focus, where the largest dynamic pressure differences in the acoustic field occur. The only parameter that can be expected to affect the magnitude of the change in hydrophobicity is the acoustic pressure. Another important consideration is that because the resonant frequency is significantly higher, the particles are all under quasi-isostatic pressure changes. I.e. the

entire antibubble is relatively undergoing a uniform dynamic pressure change. Therefore, the resonant and acoustic frequency relationship predetermined ultrasound's effect on microparticle hydrophobicity.

This research has quantitatively determined that acoustic frequencies from 1 MHz to 10 MHz have no effect on the magnitude of the change of microparticle hydrophobicity, because these frequencies are all well below the resonance frequencies of the microparticles. Therefore the dominant nonlinear frequency behaviour is the same for all the experiments. The microparticles as antibubbles are all exposed to maximal quasi-isostatic dynamic pressure changes of the ultrasound field.

The hydrophobicity measured of the sonicated samples ≈0.69 is between 30 % and 40 % lower compared to the null samples ≈1.10. This is a significant change. However, if the hydrophobic microparticles are experiencing maximal quasi-isostatic dynamic pressure changes due to their resonance, why is the measurement not completely changed hydrophilic? If explosive nucleation is expected to occur and therefore, the microparticles experience complete wetting and no subsequent renucleation, then it should be expected that the measured partition coefficient should be in the hydrophilic range, $log_{10}(P) < 0$. This is clearly not what has been quantitatively observed in this research.

The partition coefficient of the sonicated samples is ≈0.69, which is still positive. Although the relative accuracy of the measurement is not a core objective of this research (rather just the precision of the relative quantifiable difference), the value is significant enough to be considered positive. There is an explanation as to why this may be the case. The partition coefficient method does not, and fundamentally cannot, quantify the hydrophobicity of a single particle. Instead, it quantifies the ratio of the distribution of particles between the two octanol and water phases as a result of the chemical thermodynamic phenomenon of hydrophobicity. Partitioning operates on the bulk biphasic suspension. It quantifies hydrophobicity as an emergent statistical distribution between the phases governed by the underlying thermodynamics.

The assumption is that all the particles have changed hydrophobicity as a result of ultrasound exposure. This would then lead to a specific statistical distribution and thermodynamic balance, which is expected to produce a negative partition coefficient.

What is indicated by the results is that some particles have changed hydrophobicity (becoming more hydrophilic), and others have remained hydrophobic (at the same value). This would lead to a distribution with more hydrophobic particles, therefore resulting in a higher concentration in the octanol phase, leading to a positive partition coefficient. The question is, why do only some particles change in hydrophobicity while others remain hydrophobic?

Again this can be interpretively explained by the known acoustic behaviour of antibubbles. All the bubbles are in the maximal quasi-isostatic dynamic pressure changes regions of the acoustic field, but not all will exhibit the same secondary radiation forces. Some particles will exhibit oscillations that are in phase with the sound field. These particles have been observed to undergo explosive nucleation. However, some particles will oscillate in antiphase. These particles do not nucleate at all. In other words, the secondary radiation forces govern the total available microparticles that can undergo a change in hydrophobicity.

The last thing to consider from the ultrasound signal is the effect of acoustic pressure on the microparticle's hydrophobicity, or specifically, the lack thereof. The pressures tested here, 0 kPa to 100 kPa and up to 800 kPa for certain frequencies, span below and above the expected upper bound of the threshold nucleating pressure of 200 kPa from previous research. However, all these tested pressures exhibited the same change in microparticle hydrophobicity. These results indicate that variations in pressure do not affect the magnitude of the change in microparticle hydrophobicity. Therefore, the results indicate that the upper bound of the threshold nucleating pressure is significantly lower than 200 kPa. This argument is inconsistent with previous literature; however, this conclusion is also unlikely, as another more plausible explanation exists.

Nucleation of hydrophobic microparticles occurs relatively quickly. Microparticles oscillating in phase with the sound field undergo explosive nucleation within a few cycles of ultrasound. The time of one cycle is the associated period of the ultrasound signal. The longest period tested here and equivalently tested in previous literature is 1 µs. The duration of exposure was eight cycles in previous literature. Therefore, the difference of eight cycles of a 1 µs period with the exposure time of 5 min is eight orders of magnitude. Previous literature exposed microparticles to short cycles of ultrasound to prevent the

generation of standing waves. On a side note, the ultrasound parameter that affected microparticle hydrophobicity is likely time-related. The duration of exposure is a natural and almost obvious conclusion to draw because no ultrasound, i.e. zero time duration of exposure, has no effect on microparticle hydrophobicity, whereas 5 min clearly does. This parameter was kept constant for this research and thus could only exhibit an offset in the quantified hydrophobicity.

This is a crucial difference between this research's experiments and the imaged microparticles from previous literature. Therefore, standing waves, and the associated increase in acoustic amplitude from reflections within the exposure cuvette, are expected. This increase was not explicitly measured due to the physical size limitations of the equipment. Therefore, it is unclear what the actual acoustic amplitude within the cuvet was. The results do indicate that the changes occurred and that the magnitude was not affected by the acoustic pressure. This is most likely due to the four compounding effects of secondary radiation forces, increased pressure due to reflected and standing waves, the nonlinearity of the antibubble oscillations, and the extreme difference in exposure duration.

However, the results are similar to what is qualitatively observed in the literature that utilised an ultrasound bath, the starting point and motivation of this research. There, samples were sonicated for 5 min in the bath at 45 kHz, a significantly lower frequency, and at an unspecified acoustic amplitude. These samples exhibited neither nucleation nor acoustic activity when pre-exposed to the ultrasound bath, because the particles were already stripped of their gaseous shell. Therefore the results pertaining to pressure should not simply be dismissed but should be considered in context. Even though the effects of acoustic pressure on microparticle hydrophobicity are inconclusive, the results validate the nuance of acoustic pressure's complex role on microparticle hydrophobicity.

The last outcome of this research that needs to be considered is the act of reshaking the exposed and partitioned samples, and subsequent remeasurement of the partition coefficient. This tests the stability of the change in microparticle hydrophobicity caused by ultrasound. The inherent stability is self-evident from the quantifiable difference of sonicated and null samples over the initial 2.5 min timeframe. This is further reinforced by the quantifiable difference from the 5 min timeframe. There is no appreciable difference in the measurements between the 2.5 min and 5 min results, and they are correspondingly

similar. This similarity indicates that the change is stable for at least 5 min.

However, the reshaking at 5 min and subsequent reimaging and partition measurement at 7.5 min also indicate that the change is not permanent. The act of reshaking by hand effectively introduces high impulse, extremely low-frequency pressure variations. Additionally, this introduces turbulence in the solution and increases the concentration of dissolved gasses in the phases through mixing. These conditions increase the likelihood of the microparticles spontaneously renucleating and regassing, thereby restoring their hydrophobicity. These conditions would not significantly affect particles that remained hydrophobic. This argument is consistent with the results as the increase in the bulk hydrophobicity of the sonicated samples after manual reshaking is statistically significant compared to before reshaking. This observation opens the door to the possible manipulation of microparticle hydrophobicity. Suitable parameters for the renucleation of hydrophobic microparticles need to be found. Low-frequency, high-pressure impulses forcing explosive renucleation on a completely wet microparticle is a possible mechanism for microparticle hydrophobicity recovery.

The limitations of the research are now covered to close off this discussion. The limitations are ordinarily prescribed by the scope of the parameters and their values investigated in the experiments. These limitations also have their important contexts.

The frequencies investigated from 1 MHz to 10 MHz are limited by the available transducers that were used. Additionally, the bandwidth of the acoustic measurement system, particularly the hydrophone, limits the ability to verify the acoustic frequency. The ultrasonic transducer-measurement systems limit one another for quantitative investigation. The frequencies tested here were well below the modal resonant frequency of the microparticles. The minimum resonant frequency at 15 MHz may be attainable; however, the experiments may still be impractical as only 5% of the particles at most have this resonance. Since the partition coefficient acts as a bulk averaging measurement, any effect at resonance may be drowned out by the signal from the majority of the other particles not at resonance. The alternative is to use transducers that can produce ultrasound with frequencies >40 MHz. These are either non-existent or too expensive at this time.

An alternative that may be readily available also addresses another limitation of this

research. Only one microparticle material was investigated in this research, hydrophobic carbon black microparticles. There is no reason to assume that other microparticle materials with different nominal hydrophobicities will behave the same as observed in this research. Previous literature on ultrasound's qualitative effects on zinc-oxide microparticle hydrophobicity has already indicated such a difference.

Back to the limitation on frequency, the microparticle has a resonant frequency predetermined by its size and core-to-bubble ratio. Choosing a different material can also be coupled with choosing a different-sized particle. However, there is a caveat. The relation between particle size and core-to-bubble ratio greatly affect the resonant frequency in Equation 2.7. The particle's size primarily determines the resonant frequency and is inversely proportional to the resonant frequency. However, the core ratio has an extremely nonlinear effect on the resonant frequency the closer the ratio is to unity. Unlike the particle size, the core ratio is proportional to the resonant frequency. These two parameters compete with one another in determining the resonant frequency.

Microparticles can be selected so that the modal particle size is larger than those used here. Then the resonance can even be "selected" to be within the 1 MHz to 10 MHz used in this research. However, the core ratio can be expected to increase towards unity. This assumption can be justified with the following argument. A hydrophobic particle of sub-millimetre scale will also have a thin gaseous shell around it. As per previous literature, this shell is expected to be on the nanometer scale. The core-to-bubble ratio is therefore approaching unity.

As an example, consider an ordinary microbubble 100 µm in radius. A microparticle 99.8 µm in size is assumed to have a similar gaseous shell thickness of 200 nm. The core-to-bubble ratio of the microparticle is 0.998. The resonant frequency of the ordinary bubble is ≈32 kHz, just within the ultrasonic range. The resonant frequency of the microparticle is ≈900 kHz or 0.9 MHz. This is realistically attainable and could be investigated if the size of the microparticles could be controlled. Additionally, this opens up investigation for the opposite effect, i.e. when the acoustic frequency is higher than the resonant frequency. The only limitation is sourcing appropriately sized microparticles, of the desired material(s), within a practical tolerance.

The final and possibly the more important limitation is that of direct microparticle observation, or rather the lack thereof in this research. Importantly the context of this research matters. This research aimed to lay the foundation for quantifying the difference in microparticle hydrophobicity caused by ultrasound. This has been achieved. The methodological definition of the partition coefficient was employed. This is a bulk quantitative measurement of the hydrophobicity of microparticles. This is arguably an emergent property of many microparticles that are partitioned. No single microparticle was directly measured in this research. The results from this research are implicitly linked with the results from the background literature, particularly on hydrophobic microparticle nucleation. However, the links are still implicit. An emergent property here is compared with direct observations elsewhere. The quantitative partitioning method should be combined with the direct single particle imaging method from the literature to directly justify this link. This is undoubtedly going to have various practical issues. For the reader's interest, a possible experimental setup and methodology are provided in Appendix H.

5.4 Summary

Regardless of the limitations, this research has laid the foundation for quantitative analysis of the effect of ultrasound on microparticle hydrophobicity.

The three objectives of the research have been successfully completed. Firstly, the effect of a controlled acoustic frequency on the change in hydrophobicity of a sonicated microparticle has been quantified. Secondly, the effect of a controlled acoustic pressure on the change in hydrophobicity of a sonicated microparticle has been quantified. Thirdly, the time stability of the changes induced has been assessed and quantified.

These results have quantified the extent to which ultrasound changes hydrophobic microparticle hydrophobicity, and subsequently, the research question is answered. Yes, ultrasound does cause a measurable time-stable change in microparticle hydrophobicity; however, it is not related to the frequency or pressure parameters of the regime. More precisely, variations in these parameters investigated, 1 MHz to 10 MHz and 0 kPa to 100 kPa, do not affect the magnitude of the change in hydrophobicity. This is likely due

to the nonlinear frequency behaviour of the microparticle antibubbles, which dominates the acoustic behaviour. Any variation in acoustic frequency below resonance has no measurable effect on the magnitude of the change in hydrophobicity. The underlying nature behind the pressure variation not inducing a change is suspected to be caused by the extreme duration of exposure (of 5 min). However, there is no definitive evidence to support this conclusion.

Additionally, there is an uninvestigated ultrasound parameter that does affect microparticle hydrophobicity. It is theorised that the most likely and natural parameter is ultrasound exposure duration. However, other time-related parameters may also be causally connected.

Chapter 6

Conclusions

In previous literature, ultrasound was qualitatively observed to affect the hydrophobicity of carbon black microparticles. No quantitative description exists that describes the effect of ultrasound on microparticle hydrophobicity. This research identifies the lack of a quantitative description relating ultrasound to microparticle hydrophobicity as an opportunity. The central question of this research is, "*to what extent does ultrasound quantitatively change the hydrophobicity of hydrophobic microparticles?*" In answering this question, the research lays the foundation of a quantitative description and provides potential mechanisms for applications in ultrasound-guided therapeutics, amongst many other applications involving hydrophobic microparticles and their manipulation using ultrasound.

The effect of ultrasound on microparticle hydrophobicity has been quantified in this research with the following method. The octanol-water partition coefficient was used as the defining metric for quantifying hydrophobicity. The partition coefficient is defined as the ratio of a test species' concentration in octanol to that of water in a biphasic immiscible mixture. Practically, the partition coefficient is reported in the base ten logarithm form. The concentrations in each phase were measured in this research with image colourimetry and digital image processing. A custom equation and subsequent MATLAB script were developed for the colourimetric partition coefficient measurement. The colourimetric partition coefficient measurement method is novel. The absolute accuracy of the method is not of importance in this research; only the relative quantified difference between sonicated and null sample hydrophobicity is important. However, the satistical analysis

of the results justifies the basic validity of the novel colourimetric partition coefficient measurement method. Samples of hydrophobic carbon black microparticles were exposed to various ultrasound regimes spanning 1 MHz to 10 MHz and 10 kPa to 800 kPa. The samples were partitioned after exposure and imaged after 2.5 min and 5 min, and the subsequent partition coefficients were calculated.

Statistical and linear regression analyses were used to find parameters that quantitatively describe the effect of ultrasound on microparticle hydrophobicity. Specifically, the difference in the hydrophobicity of the exposed samples compared to the null experiments is highlighted. This difference is justified quantitatively with the standard deviation difference between the measurements. The linear regression gradients for both frequency and pressure were quantified. These gradients quantify the effect of these ultrasound parameters on changes in microparticle hydrophobicity. Further regression analysis determined if an unknown ultrasound parameter also affects microparticle hydrophobicity.

Exposed samples had a significant and measurable change in their hydrophobicity, as quantified through the octanol-water partition coefficient. All the sonicated samples had a consistent change in their hydrophobicity, with a mean partition coefficient of 0.65 ± 0.13. The null samples had a mean partition coefficient of 1.12 ± 0.15. Therefore, ultrasound quantitatively reduced the hydrophobicity by 42% compared to the null hydrophobicity. The relative difference in these measurements is $\approx 3\sigma$ and is statistically significant. The percentage change and standard deviation quantify the extent to which ultrasound changes microparticle hydrophobicity. Thus, the research question has been answered, and the result is desirable.

However, the regression gradients for ultrasonic frequency and pressure parameters on the partition coefficient were both negligibly zero. Therefore, both had no quantifiable effect on the magnitude of the change in microparticle hydrophobicity. However, a change has been quantified; therefore, microparticle hydrophobicity is affected by an unknown/uninvestigated ultrasound parameter. It's suggested that the most likely parameter attributed to this change is the ultrasound exposure duration. In this research, the ultrasound exposure time was kept constant at 5 min.

The change in microparticle hydrophobicity was also stable through time, as indicated

by the mean hydrophobicity measured at 2.5 min and 5 min after exposure, with average partition coefficients of 0.63 ± 0.10 and 0.65 ± 0.13, respectively. The hydrophobicity is also recoverable. When the exposed samples were re-agitated by hand after 5 min and imaged at 7.5 min, the average partition coefficient increased to 0.84 ± 0.09. This is a relative statistical change of $\approx 1.5\sigma$. Although this is not strictly significant, the change is contextually significant when comparing the original 0.65 ± 0.13 value to the null 1.12 ± 0.15 value. This change is still ultrasonic frequency and pressure independent.

The reason for ultrasonic frequency and pressure having no impact on the microparticle hydrophobicity is attributed to the antibubble resonance phenomenon. The carbon black microparticles investigated in this research have a resonance frequency >40 MHz, significantly higher than the largest frequency tested in this research. The resonant frequency determines the fundamental behaviour of the particles in an acoustic field, fundamentally related to both the primary and secondary radiation forces. The nonlinearity of the resonant frequency to the antibubble core ratio, and the previously described nonlinear radial excursion of antibibbles in an acoustic field, dominate their behaviour. The hydrophobic microparticles necessarily move into the antinodes of the acoustic field because the frequencies in this research are below the microparticle-antibubble resonance frequency. Thus, the microparticles experience the largest amplitude changes in the acoustic field. It's thought pressure changes had no effect due to the relatively large exposure time compared to the number of cycles of ultrasound required to nucleate a hydrophobic microparticle and subsequently change its hydrophobicity.

The causal relation between the previously observed nucleation phenomenon of hydrophobic microparticles exposed to ultrasound and the change in microparticle hydrophobicity caused by ultrasound, is only implied by this research. Current practical limitations may make direct observations supporting this causality difficult. An experimental setup that can simultaneously observe the proposed nucleation of an individual hydrophobic microparticle and its transition between an octanol-water partition boundary is required to make the causal relation concrete.

References

[1] N. Kudo *et al.*, 'Asymmetric oscillations of endoskeletal antibubbles,' *Japanese Journal of Applied Physics*, vol. 59, no. SK, SKKE02, Mar. 2020.

[2] M. Postema, A. Novell, C. Sennoga, A. T. Poortinga and A. Bouakaz, 'Harmonic response from microscopic antibubbles,' *Applied Acoustics*, vol. 137, pp. 148–150, Aug. 2018.

[3] S. Kotopoulis, K. Johansen, O. Gilja, A. Poortinga and M. Postema, 'Acoustically active antibubbles,' *Acta Physica Polonica A*, vol. 127, no. 1, pp. 99–102, Jan. 2015.

[4] M. Lengyel, N. Kállai-Szabó, V. Antal, A. J. Laki and I. Antal, 'Microparticles, microspheres, and microcapsules for advanced drug delivery,' *Scientia Pharmaceutica*, vol. 87, no. 3, p. 20, Aug. 2019.

[5] M. Vert *et al.*, 'Terminology for biorelated polymers and applications (IUPAC recommendations 2012),' *Pure and Applied Chemistry*, vol. 84, no. 2, pp. 377–410, Jan. 2012.

[6] M. Postema, *Fundamentals of Medical Ultrasonics*. London: CRC Press, 2011.

[7] P. Attard, 'Nanobubbles and the hydrophobic attraction,' *Advances in Colloid and Interface Science*, vol. 104, no. 1-3, pp. 75–91, Jul. 2003.

[8] P. W. Atkins and J. de Paula, *Atkins' Physical chemistry*. New York: W.H. Freeman, 2006.

[9] T. Brown, H. E. LeMay, B. E. Bursten, C. J. Murphy and P. M. Woodward, *Chemistry : the central science*. Boston: Prentice Hall, 2012.

[10] A. Neumann, R. David and Y. Zuo, Eds., *Applied Surface Thermodynamics*. CRC Press, Oct. 2010.

[11] H.-J. Butt, K. Graf and M. Kappl, *Physics and Chemistry of Interfaces*. Wiley, Sep. 2003.

[12] J. Sangster, 'Octanol-water partition coefficients of simple organic compounds,' *Journal of Physical and Chemical Reference Data*, vol. 18, no. 3, pp. 1111–1229, Jul. 1989.

[13] E. B. Podgorsak, *Radiation Physics for Medical Physicists*. Springer, 2016, ISBN: 9783319253800.

[14] S. K. Kohl, J. D. Landmark and D. F. Stickle, 'Demonstration of absorbance using digital color image analysis and colored solutions,' *Journal of Chemical Education*, vol. 83, no. 4, p. 644, Apr. 2006.

[15] S. Šafranko, P. Živković, A. Stanković, M. Medvidović-Kosanović, A. Széchenyi and S. Jokić, 'Designing ColorX, image processing software for colorimetric determination of concentration, to facilitate students' investigation of analytical chemistry concepts using digital imaging technology,' *Journal of Chemical Education*, vol. 96, no. 9, pp. 1928–1937, Aug. 2019.

[16] C. T. Gee, E. Kehoe, W. C. K. Pomerantz and R. L. Penn, 'Quantifying protein concentrations using smartphone colorimetry: A new method for an established test,' *Journal of Chemical Education*, vol. 94, no. 7, pp. 941–945, May 2017.

[17] D. Mullins, D. Coburn, L. Hannon, E. Jones, E. Clifford and M. Glavin, 'A novel image processing-based system for turbidity measurement in domestic and industrial wastewater,' *Water Science and Technology*, vol. 77, no. 5, pp. 1469–1482, Jan. 2018.

[18] Y. Liu, Y. Chen and X. Fang, 'A review of turbidity detection based on computer vision,' *IEEE Access*, vol. 6, pp. 60 586–60 604, 2018.

[19] M. Kovačić and D. Ašperger, 'Low-cost turbidimeter, colorimeter, and nephelometer for the student laboratory,' *Journal of Chemical Education*, vol. 96, no. 11, pp. 2649–2654, Oct. 2019.

[20] V. I. Golovanov, 'Main factors affecting the photographic determination of the turbidity and chromaticity of water,' *Journal of Analytical Chemistry*, vol. 75, no. 3, pp. 320–329, Mar. 2020.

[21] Y. Wen, Y. Hu and X. Wang, 'Application of a colorimeter for turbidity measurement,' *Journal of Physics: Conference Series*, vol. 679, p. 012 028, Feb. 2016.

[22] M. Postema, S. Kotopoulis and K.-V. Jenderka, 'Physical principles of medical ultrasound,' in *EFSUMB Coursebook on Ultrasound*, EFSUMB, Apr. 2020, pp. 1–23.

[23] J. D. N. Cheeke, *Fundamentals and Applications of Ultrasonic Waves*, J. David and N. Cheeke, Eds. CRC Press, Dec. 2017.

[24] H. Kuttruff, *Ultrasonics: Fundamentals and Applications*. Springer Netherlands, 1991.

[25] T. G. Leighton, A. J. Walton and M. J. W. Pickworth, 'Primary bjerknes forces,' *European Journal of Physics*, vol. 11, no. 1, pp. 47–50, Jan. 1990.

[26] C. S. Carlson, A. Deroubaix, C. Penny and M. Postema, 'On the attenuation of ultrasound by pure black tattoo ink,' *SAIEE Africa Research Journal*, vol. 112, no. 1, pp. 24–31, Mar. 2021. DOI: 10.23919/saiee.2021.9340534.

[27] C. S. Carlson, R. Matsumoto, K. Fushino, M. Shinzato, N. Kudo and M. Postema, 'Nucleation threshold of carbon black ultrasound contrast agent,' *Japanese Journal of Applied Physics*, vol. 60, no. SD, SDDA06, Mar. 2021. DOI: 10.35848/1347-4065/abef0f.

[28] M. Postema, R. Matsumoto, R.-i. Shimizu, A. T. Poortinga and N. Kudo, 'High-speed footage shows transient ultrasonic nucleation of different hydrophobic particles in suspension,' *Japanese Journal of Applied Physics*, vol. 59, no. SK, SKKD07, Mar. 2020.

Appendix A

Acoustic measurement and calibration

This appendix provides the graphs of the measured voltage signals from the signal generator, and the hydrophone measurement system. The time-domain signals are plotted together for comparison. The relative amplitude frequency spectrums of the hydrophone signal and the signal generator voltage are also provided. This enables a comparison of the purity and distortion of the acoustic signal generated by the custom transducer, measured by the hydrophone, and the input signal itself.

These measurements are taken with the standard setup as explained in Section 3.2, using the calibration sample of pure water. In each of the figures, the red plots are of the hydrophone measurement, and the blue plots are of the signal generator input. The left (a)-subfigures are the time-domain signals. The left y-axis of the time domain figures is for the (red) hydrophone signal voltage, and the right y-axis is for the (blue) signal generator input voltage. The hydrophone signal also has the voltage level associated with the desired pressure amplitude. An overview of the measured transducer properties is discussed below. The right (b)-subfigures are the frequency spectrums, with the hydrophone spectrum above the signal generator spectrum.

The time-domain signals are triggered on the hydrophone measurement, and the signals seen in the figures are the start (first 2 µs) of the 100-cycle acoustic pulse used. Noticeably, there is a clear phase delay for frequencies above 5 MHz. This phase delay becomes more pronounced at 10 MHz. Additionally, the transducer takes a couple of cycles to reach its full amplitude. This delay has a negligible effect on the desired experimental acoustic

signal properties.

The frequency spectrum is evaluated using the standard MATLAB fast Fourier Transform (FFT) function `fft()` on the comma-separated values `.csv` data files saved from the oscilloscope. The FFT is performed on the entire 100-cycle pulse of the hydrophone signal and signal generator input.

Noticeable harmonics are present for the 1 MHz and 2 MHz. These start at 50 kPa for both 1 MHz and 2 MHz and become more prevalent the higher the control pressure amplitudes. For 1 MHz at the highest control amplitude of 100 kPa, there are significant harmonics present at 3 MHz, 5 MHz and 7 MHz. The harmonics each have a relative amplitude of about 0.4 times the fundamental 1 MHz amplitude. For 2 MHz at the highest control amplitude of 100 kPa there is one significant harmonic at 6 MHz with a relative amplitude of 0.7 times the fundamental.

For 3 MHz at 100 kPa there is a small harmonic present at 9 MHz with a relative amp of approximately 0.15 times the fundamental. All the remaining experimental control frequencies do not exhibit any significant harmonic distortion at any of the experimental control amplitudes. The measured experimental calibration and verification signals are seen below.

A.1 Measured calibration signals for 1 MHz

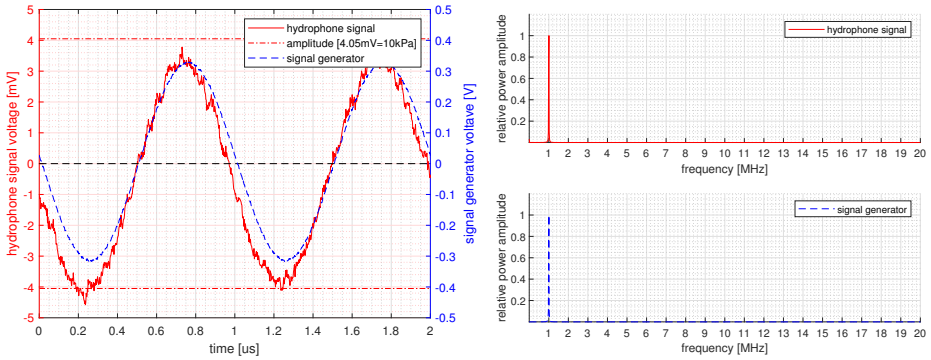

(a) time signal (b) frequency spectrum

Figure A.1:

Figure description: Measured signal voltages for 1 MHz at 10 kPa:

The time-domain signals are seen on the left (a) subfigure. The frequency spectrums are seen on the right (b) subfigure, with the hydrophone spectrum above the signal generator spectrum. The hydrophone voltage is red and signal generator voltage blue. There are no noticeable harmonics and the signal has high purity. (Amplitude level: 4.05 mV = 10 kPa)

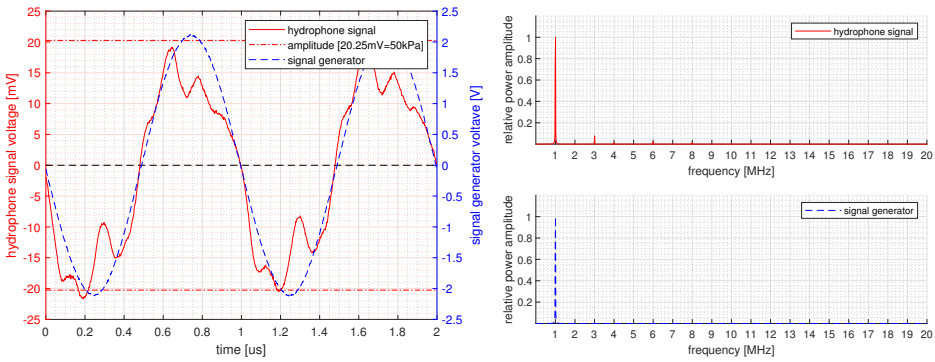

(a) time signal (b) frequency spectrum

Figure A.2:

Figure description: Measured signal voltages for 1 MHz at 50 kPa:

The time-domain signals are seen on the left (a) subfigure. The frequency spectrums are seen on the right (b) subfigure, with the hydrophone spectrum above the signal generator spectrum. The hydrophone voltage is red and signal generator voltage blue. There is a small harmonic present at 3 MHz. This has slightly distorted peak of the 1 MHz signal. (Amplitude level: 20.25 mV = 50 kPa)

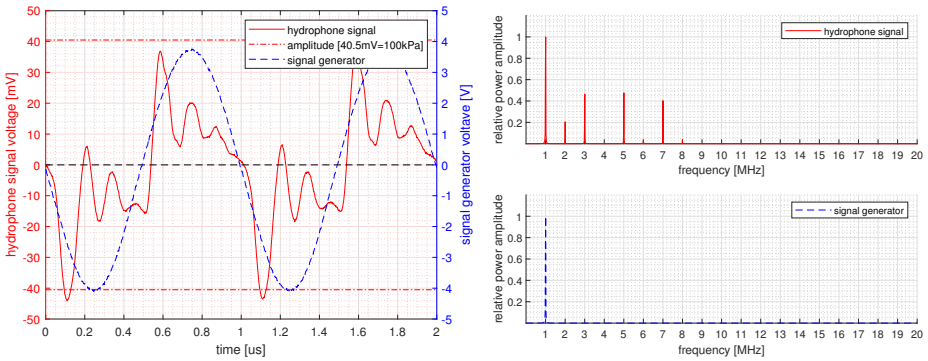

(a) time signal (b) frequency spectrum

Figure A.3:

Figure description: Measured signal voltages for 1 MHz at 100 kPa:

The time-domain signals are seen on the left (a) subfigure. The frequency spectrums are seen on the right (b) subfigure, with the hydrophone spectrum above the signal generator spectrum. The hydrophone voltage is red and signal generator voltage blue. There are multiple harmonics present at 3 MHz, 5 MHz and 7 MHz with a superharmonic at 2 MHz. The signal is heavily distorted. The signal can be considered as a 1 MHz impulse train (positive and negative). (Amplitude level: 40.5 mV = 100 kPa)

A.2 Measured calibration signals for 2 MHz

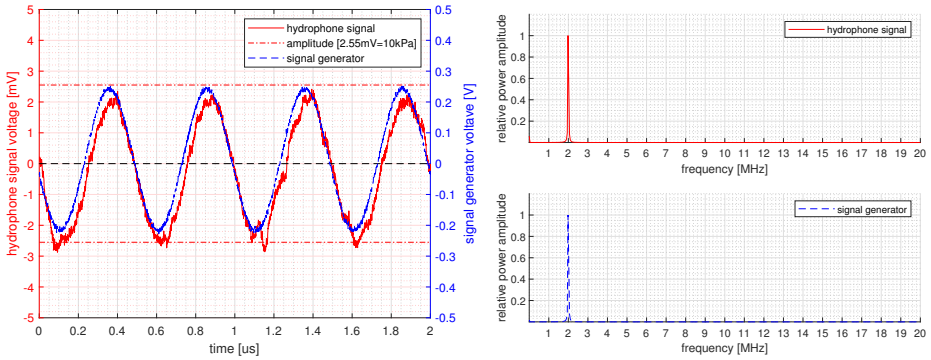

(a) time signal (b) frequency spectrum

Figure A.4:

Figure description: Measured signal voltages for 2 MHz at 10 kPa:

The time-domain signals are seen on the left (a) subfigure. The frequency spectrums are seen on the right (b) subfigure, with the hydrophone spectrum above the signal generator spectrum. The hydrophone voltage is red and signal generator voltage blue. There are no noticeable harmonics and the signal has high purity. (Amplitude level: 2.55 mV = 10 kPa)

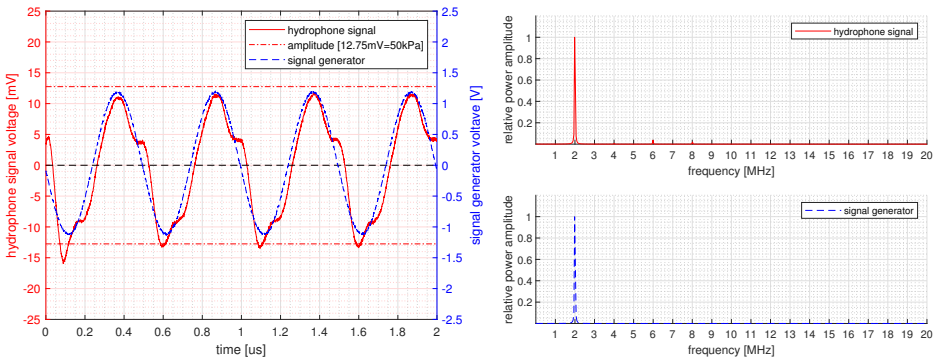

(a) time signal (b) frequency spectrum

Figure A.5:

Figure description: Measured signal voltages for 2 MHz at 50 kPa:

The time-domain signals are seen on the left (a) subfigure. The frequency spectrums are seen on the right (b) subfigure, with the hydrophone spectrum above the signal generator spectrum. The hydrophone voltage is red and signal generator voltage blue. There is a harmonic at 6 MHz, though this is more evident in the time plot. This is however considered negligible. (Amplitude level: 12.75 mV = 50 kPa)

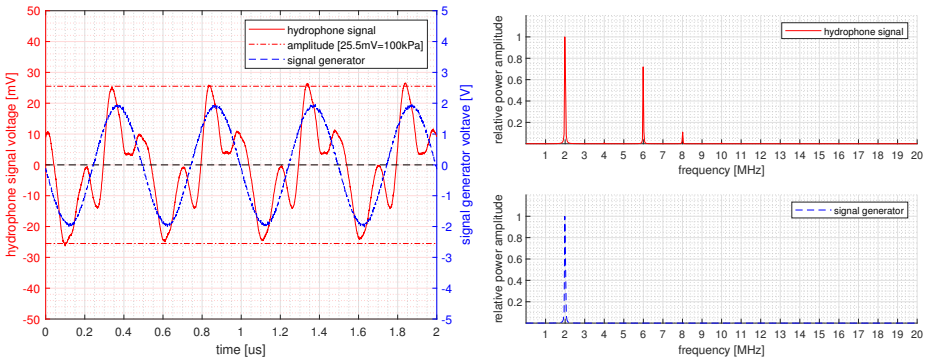

(a) time signal (b) frequency spectrum

Figure A.6:

Figure description: Measured signal voltages for 2 MHz at 100 kPa:

The time-domain signals are seen on the left (a) subfigure. The frequency spectrums are seen on the right (b) subfigure, with the hydrophone spectrum above the signal generator spectrum. The hydrophone voltage is red and signal generator voltage blue. There is a prominent harmonic at 6 MHz (the second harmonic) and a small harmonic at 8 MHz. This has made the signal more triangular-like. Unusually, there is no first harmonic present at 4 MHz. (Amplitude level: 25.5 mV = 100 kPa)

A.3 Measured calibration signals for 3 MHz

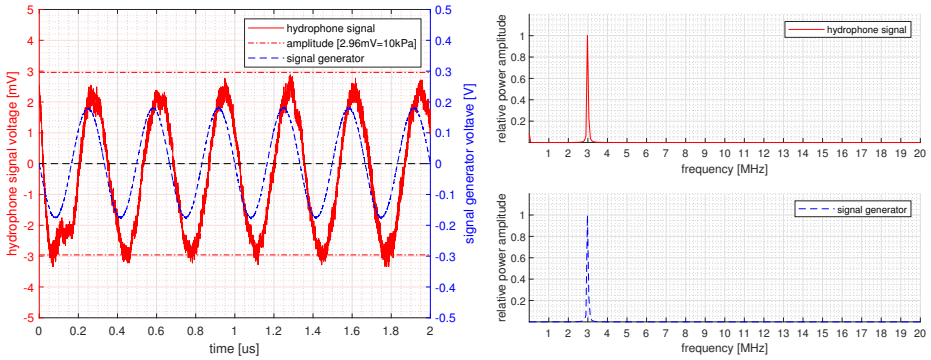

(a) time signal (b) frequency spectrum

Figure A.7:

Figure description: Measured signal voltages for 3 MHz at 10 kPa:

The time-domain signals are seen on the left (a) subfigure. The frequency spectrums are seen on the right (b) subfigure, with the hydrophone spectrum above the signal generator spectrum. The hydrophone voltage is red and signal generator voltage blue. There are no noticeable harmonics and the signal has high purity. (Amplitude level: 2.96 mV = 10 kPa)

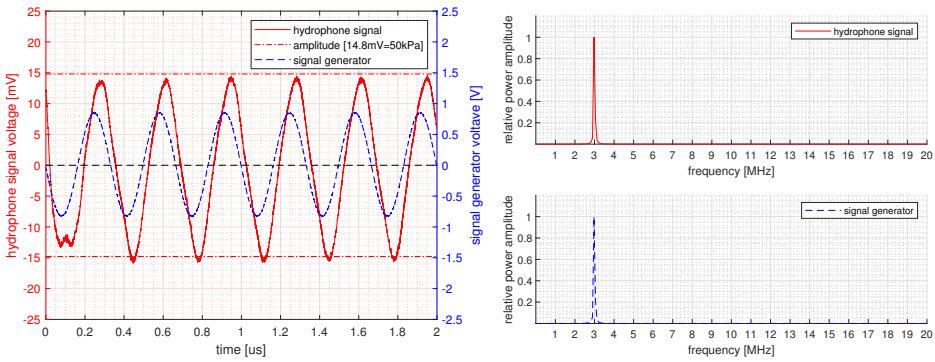

(a) time signal (b) frequency spectrum

Figure A.8:

Figure description: Measured signal voltages for 3 MHz at 50 kPa:

The time-domain signals are seen on the left (a) subfigure. The frequency spectrums are seen on the right (b) subfigure, with the hydrophone spectrum above the signal generator spectrum. The hydrophone voltage is red and signal generator voltage blue. There are no noticeable harmonics and the signal has high purity. (Amplitude level: 14.8 mV = 50 kPa)

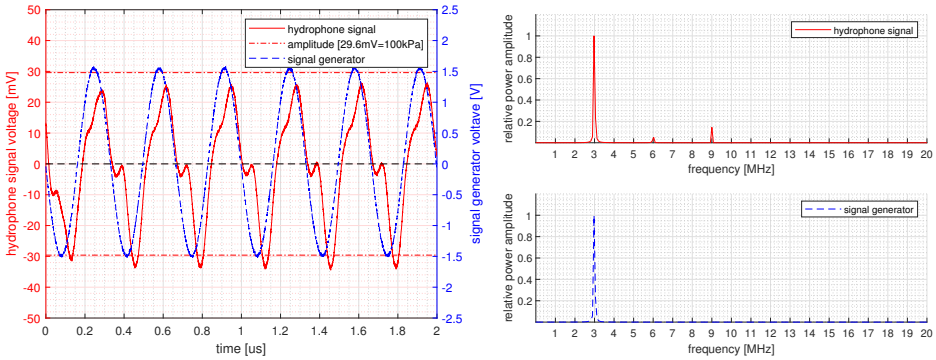

(a) time signal (b) frequency spectrum

Figure A.9:

Figure description: Measured signal voltages for 3 MHz at 100 kPa:

The time-domain signals are seen on the left (a) subfigure. The frequency spectrums are seen on the right (b) subfigure, with the hydrophone spectrum above the signal generator spectrum. The hydrophone voltage is red and signal generator voltage blue. There is a negligible harmonic at 6 MHz and a larger, but still relatively negligible harmonic at 9 MHz. (Amplitude level: 29.6 mV = 100 kPa).

A.4 Measured calibration signals for 4 MHz

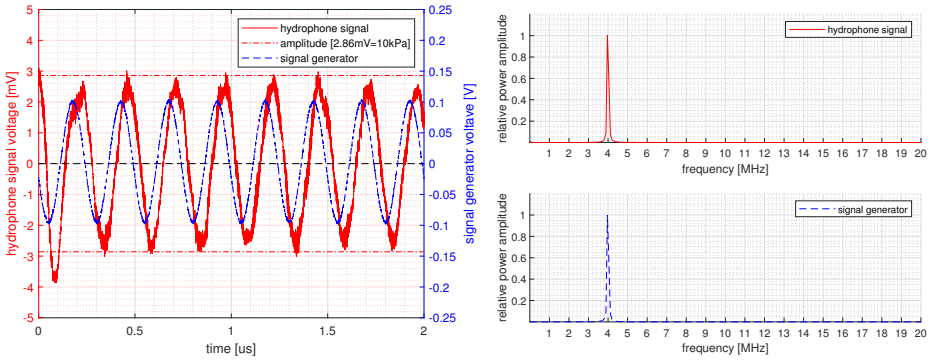

(a) time signal (b) frequency spectrum

Figure A.10:

Figure description: Measured signal voltages for 4 MHz at 10 kPa:

The time-domain signals are seen on the left (a) subfigure. The frequency spectrums are seen on the right (b) subfigure, with the hydrophone spectrum above the signal generator spectrum. The hydrophone voltage is red and signal generator voltage blue. There are no noticeable harmonics and the signal has high purity. (Amplitude level: 2.86 mV = 10 kPa)

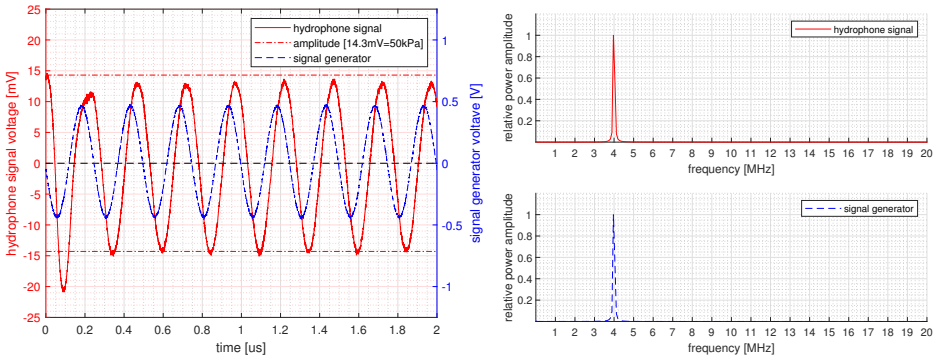

(a) time signal (b) frequency spectrum

Figure A.11:

Figure description: Measured signal voltages for 4 MHz at 50 kPa:

The time-domain signals are seen on the left (a) subfigure. The frequency spectrums are seen on the right (b) subfigure, with the hydrophone spectrum above the signal generator spectrum. The hydrophone voltage is red and signal generator voltage blue. There are no noticeable harmonics and the signal has high purity. (Amplitude level: 14.3 mV = 50 kPa)

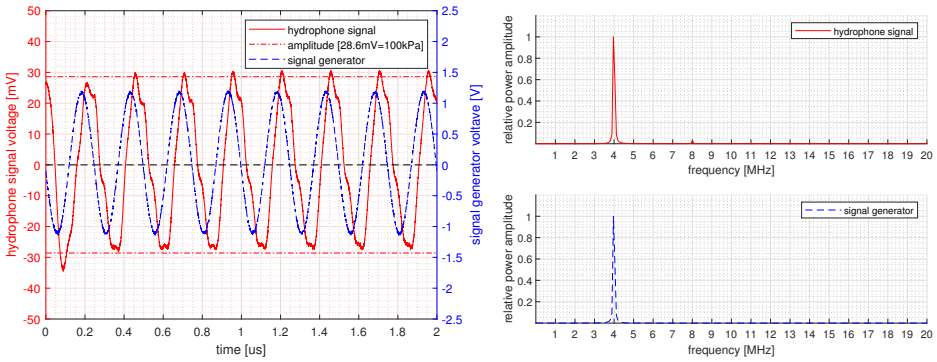

(a) time signal (b) frequency spectrum

Figure A.12:

Figure description: Measured signal voltages for 4 MHz at 100 kPa:

The time-domain signals are seen on the left (a) subfigure. The frequency spectrums are seen on the right (b) subfigure, with the hydrophone spectrum above the signal generator spectrum. The hydrophone voltage is red and signal generator voltage blue. There are no noticeable harmonics and the signal has high purity. There is noticible but negligible distortion that is evident in the time-domain signal. This is generated by a very small 8 MHz harmonic. (Amplitude level: 28.6 mV = 100 kPa)

A.5 Measured calibration signals for 5 MHz

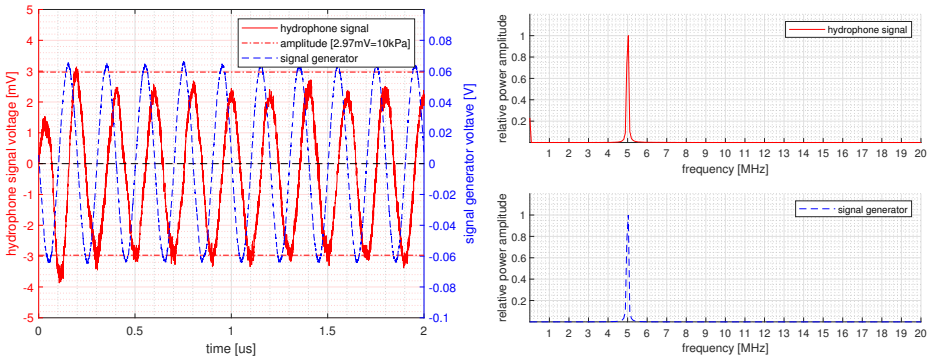

(a) time signal (b) frequency spectrum

Figure A.13:

Figure description: Measured signal voltages for 5 MHz at 10 kPa:

The time-domain signals are seen on the left (a) subfigure. The frequency spectrums are seen on the right (b) subfigure, with the hydrophone spectrum above the signal generator spectrum. The hydrophone voltage is red and signal generator voltage blue. There are no noticeable harmonics and the signal has high purity. (Amplitude level: 2.97 mV = 10 kPa)

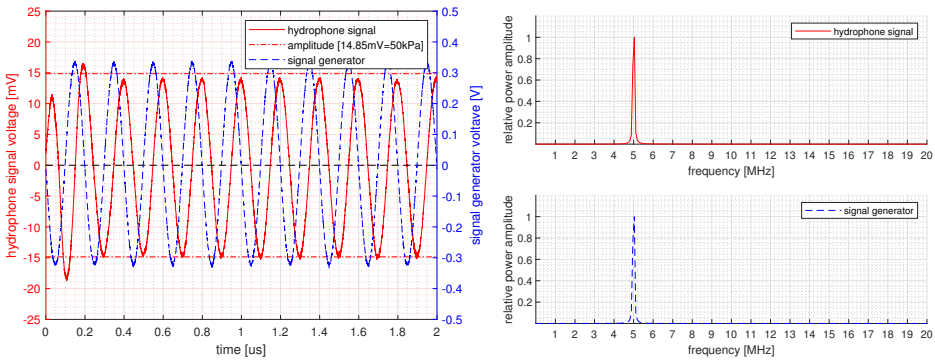

(a) time signal (b) frequency spectrum

Figure A.14:

Figure description: Measured signal voltages for 5 MHz at 50 kPa:

The time-domain signals are seen on the left (a) subfigure. The frequency spectrums are seen on the right (b) subfigure, with the hydrophone spectrum above the signal generator spectrum. The hydrophone voltage is red and signal generator voltage blue. There are no noticeable harmonics and the signal has high purity. (Amplitude level: 14.85 mV = 50 kPa)

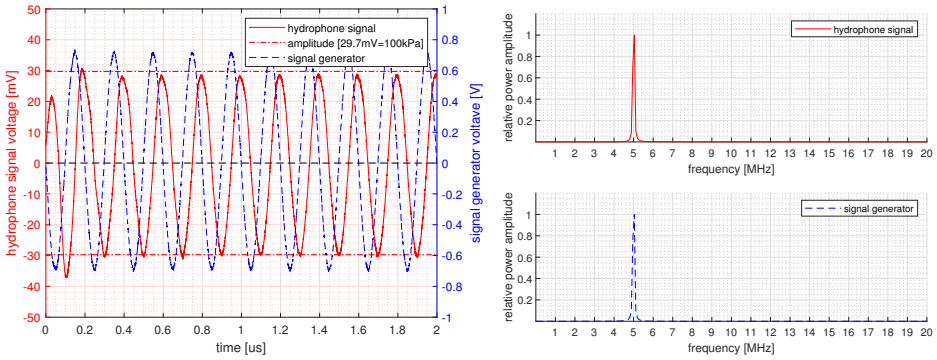

(a) time signal (b) frequency spectrum

Figure A.15:

Figure description: Measured signal voltages for 5 MHz at 100 kPa:

The time-domain signals are seen on the left (a) subfigure. The frequency spectrums are seen on the right (b) subfigure, with the hydrophone spectrum above the signal generator spectrum. The hydrophone voltage is red and signal generator voltage blue. There are no noticeable harmonics and the signal has high purity. (Amplitude level: 29.7 mV = 100 kPa)

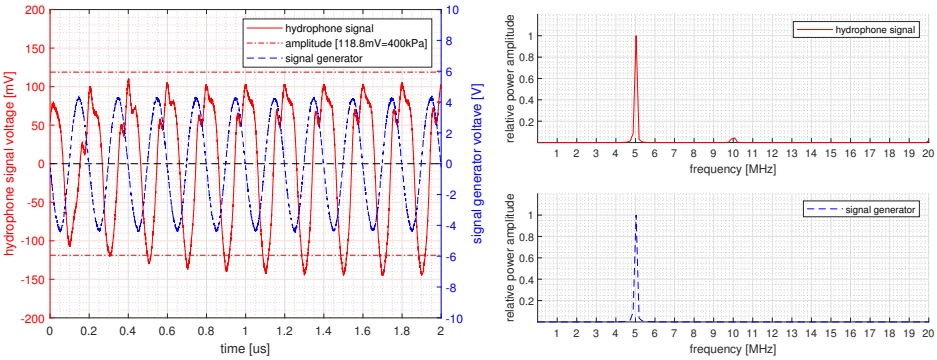

(a) time signal (b) frequency spectrum

Figure A.16:

Figure description: **Measured signal voltages for** 5 MHz **at** 400 kPa:

The time-domain signals are seen on the left (a) subfigure. The frequency spectrums are seen on the right (b) subfigure, with the hydrophone spectrum above the signal generator spectrum. The hydrophone voltage is red and signal generator voltage blue. There are no prominent harmonics. There is only a small and negligible 10 MHz component. (Amplitude level: 118.8 mV = 400 kPa)

A.6 Measured calibration signals for 6 MHz

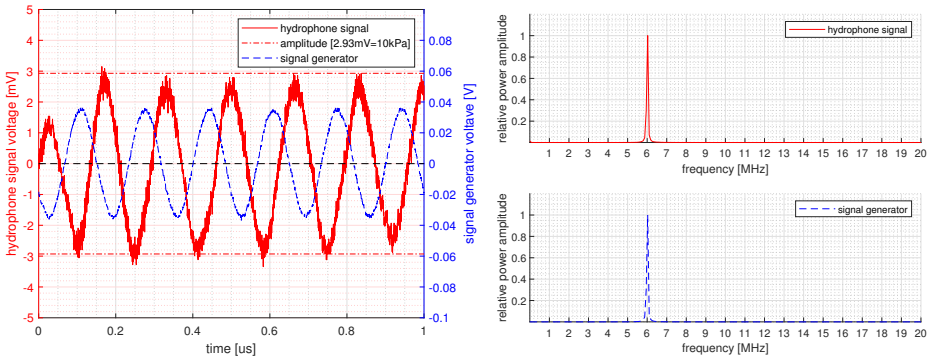

(a) time signal (b) frequency spectrum

Figure A.17:

Figure description: Measured signal voltages for 6 MHz at 10 kPa:

The time-domain signals are seen on the left (a) subfigure. The frequency spectrums are seen on the right (b) subfigure, with the hydrophone spectrum above the signal generator spectrum. The hydrophone voltage is red and signal generator voltage blue. There are no noticeable harmonics and the signal has high purity. (Amplitude level: 2.93 mV = 10 kPa)

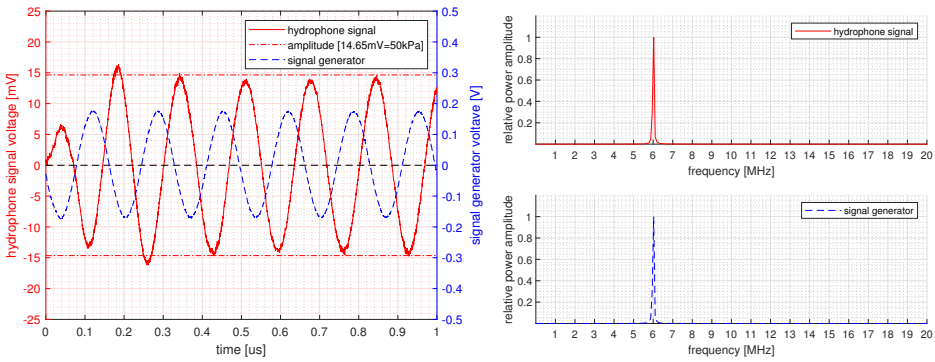

(a) time signal (b) frequency spectrum

Figure A.18:

Figure description: Measured signal voltages for 6 MHz at 50 kPa:

The time-domain signals are seen on the left (a) subfigure. The frequency spectrums are seen on the right (b) subfigure, with the hydrophone spectrum above the signal generator spectrum. The hydrophone voltage is red and signal generator voltage blue. There are no noticeable harmonics and the signal has high purity. (Amplitude level: 14.65 mV = 50 kPa)

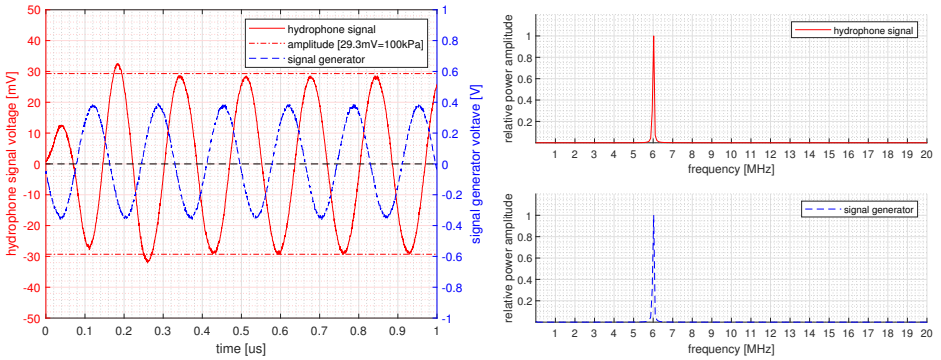

(a) time signal (b) frequency spectrum

Figure A.19:

Figure description: Measured signal voltages for 6 MHz at 100 kPa:

The time-domain signals are seen on the left (a) subfigure. The frequency spectrums are seen on the right (b) subfigure, with the hydrophone spectrum above the signal generator spectrum. The hydrophone voltage is red and signal generator voltage blue. There are no noticeable harmonics or signal distortion. (Amplitude level: 29.3 mV = 100 kPa)

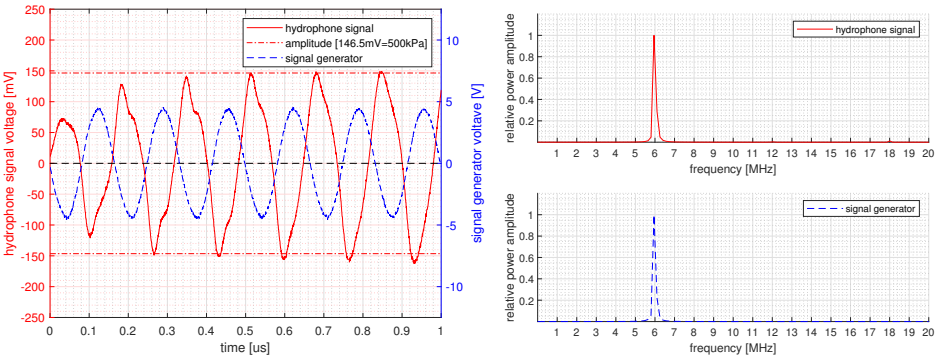

(a) time signal (b) frequency spectrum

Figure A.20:

Figure description: **Measured signal voltages for** 6 MHz **at** 500 kPa:

The time-domain signals are seen on the left (a) subfigure. The frequency spectrums are seen on the right (b) subfigure, with the hydrophone spectrum above the signal generator spectrum. The hydrophone voltage is red and signal generator voltage blue. There is some distortion visible int he time domain however no specific harmonic in the frequency domain. The fundamental at 6 MHz does seem wider than those above. The transducer takes one cycle to reach the desired amplitude. (Amplitude level: 146.5 mV = 500 kPa)

A.7 Measured calibration signals for 7 MHz

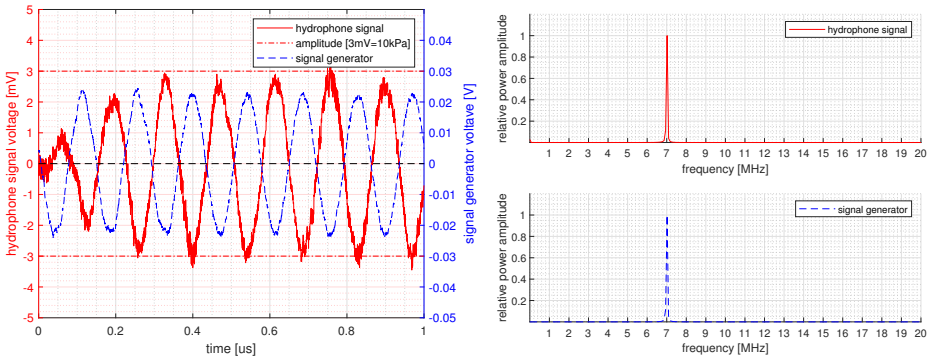

(a) time signal (b) frequency spectrum

Figure A.21:

Figure description: Measured signal voltages for 7 MHz at 10 kPa:
The time-domain signals are seen on the left (a) subfigure. The frequency spectrums are seen on the right (b) subfigure, with the hydrophone spectrum above the signal generator spectrum. The hydrophone voltage is red and signal generator voltage blue. There are no noticeable harmonics or signal distortion. The transducer takes one cycle to reach the desired amplitude. (Amplitude level: 3.0 mV = 10 kPa)

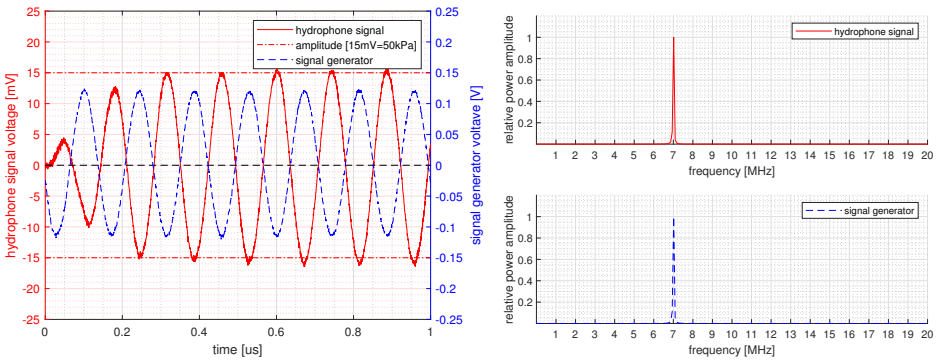

(a) time signal (b) frequency spectrum

Figure A.22:

Figure description: Measured signal voltages for 7 MHz at 50 kPa:
The time-domain signals are seen on the left (a) subfigure. The frequency spectrums are seen on the right (b) subfigure, with the hydrophone spectrum above the signal generator spectrum. The hydrophone voltage is red and signal generator voltage blue. There are no noticeable harmonics or signal distortion. The transducer takes one cycle to reach the desired amplitude. (Amplitude level: 15 mV = 50 kPa)

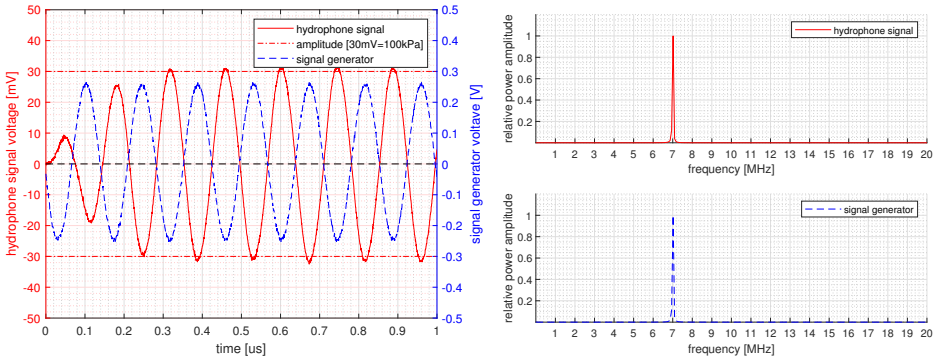

(a) time signal (b) frequency spectrum

Figure A.23:

Figure description: Measured signal voltages for 7 MHz at 100 kPa:

The time-domain signals are seen on the left (a) subfigure. The frequency spectrums are seen on the right (b) subfigure, with the hydrophone spectrum above the signal generator spectrum. The hydrophone voltage is red and signal generator voltage blue. There are no noticeable harmonics or signal distortion. The transducer takes one cycle to reach the desired amplitude. (Amplitude level: 30 mV = 100 kPa)

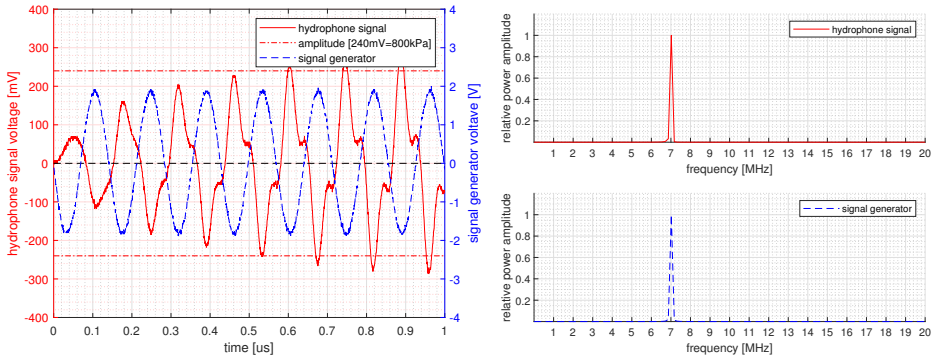

(a) time signal (b) frequency spectrum

Figure A.24:

Figure description: **Measured signal voltages for** 7 MHz **at** 800 kPa:

The time-domain signals are seen on the left (a) subfigure. The frequency spectrums are seen on the right (b) subfigure, with the hydrophone spectrum above the signal generator spectrum. The hydrophone voltage is red and signal generator voltage blue. There is a distortion visible in the time-domain. This is not seen in the frequency domain and is assumed to be at a harmonic not that is of a higher frequency than shown (seemingly 21 MHz). The fundamental is also wider than those seen above. The transducer takes about four cycles to reach the desired amplitude. (Amplitude level: 240 mV = 800 kPa)

A.8 Measured calibration signals for 8 MHz

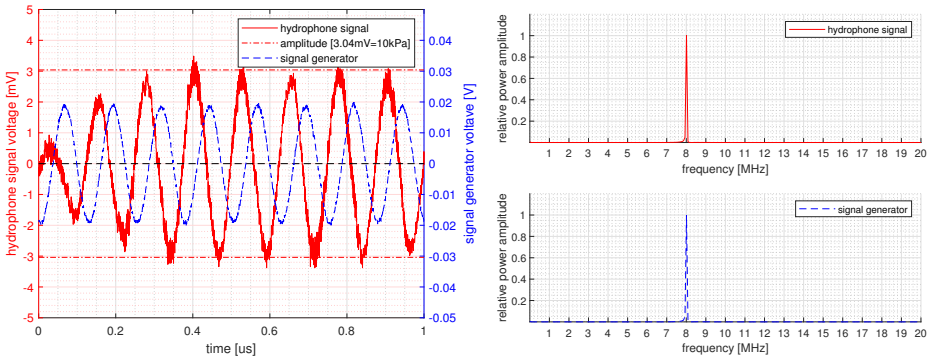

(a) time signal (b) frequency spectrum

Figure A.25:

Figure description: Measured signal voltages for 8 MHz at 10 kPa:

The time-domain signals are seen on the left (a) subfigure. The frequency spectrums are seen on the right (b) subfigure, with the hydrophone spectrum above the signal generator spectrum. The hydrophone voltage is red and signal generator voltage blue. There are no noticeable harmonics or signal distortion. The transducer takes one cycle to reach the desired amplitude. (Amplitude level: 3.04 mV = 10 kPa)

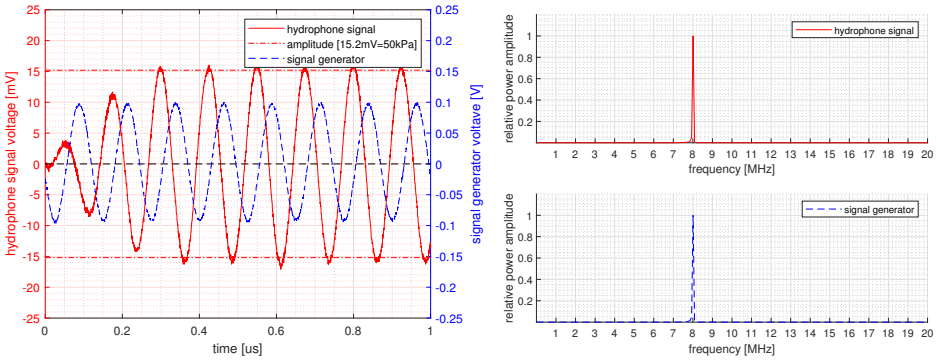

(a) time signal (b) frequency spectrum

Figure A.26:

Figure description: Measured signal voltages for 8 MHz at 50 kPa:
The time-domain signals are seen on the left (a) subfigure. The frequency spectrums are seen on the right (b) subfigure, with the hydrophone spectrum above the signal generator spectrum. The hydrophone voltage is red and signal generator voltage blue. There are no noticeable harmonics or signal distortion. The transducer takes a couple of cycles to reach the desired amplitude. (Amplitude level: 15.2 mV = 50 kPa)

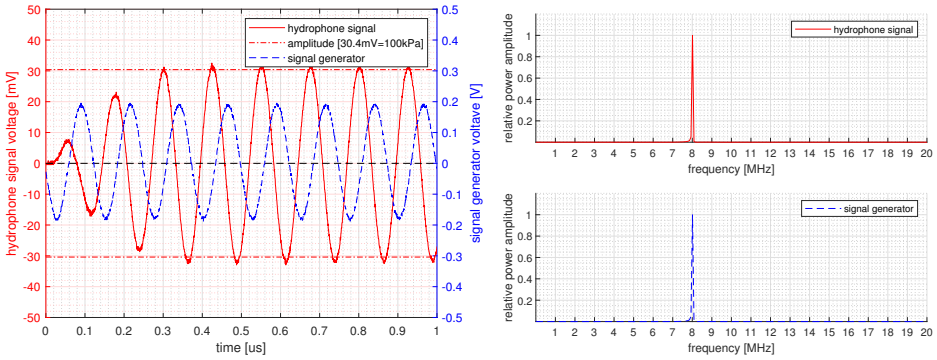

(a) time signal (b) frequency spectrum

Figure A.27:

Figure description: Measured signal voltages for 8 MHz at 100 kPa:
The time-domain signals are seen on the left (a) subfigure. The frequency spectrums are seen on the right (b) subfigure, with the hydrophone spectrum above the signal generator spectrum. The hydrophone voltage is red and signal generator voltage blue. There are no noticeable harmonics or signal distortion. The transducer takes a couple of cycles to reach the desired amplitude level. (Amplitude level: 30.4 mV = 100 kPa)

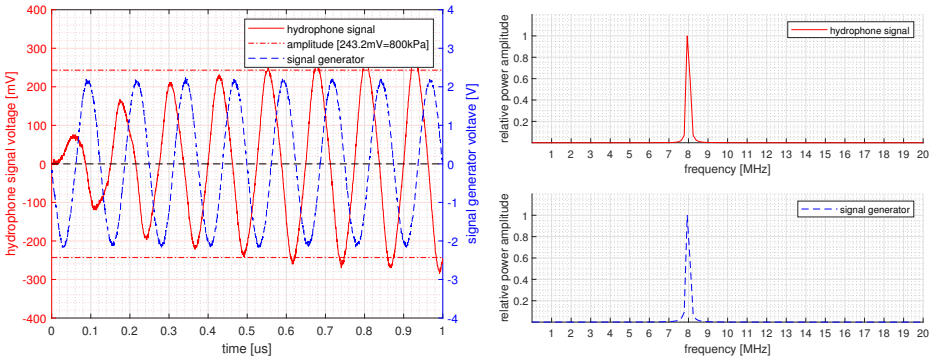

(a) time signal (b) frequency spectrum

Figure A.28:

Figure description: **Measured signal voltages for** 8 MHz **at** 800 kPa:

The time-domain signals are seen on the left (a) subfigure. The frequency spectrums are seen on the right (b) subfigure, with the hydrophone spectrum above the signal generator spectrum. The hydrophone voltage is red and signal generator voltage blue. There are no noticeable harmonics, There is some signal distortion visible in the time domain as the transducer is initially energised. This however seems to stabilise, and the signal then becomes relatively distortionless. The bandwidth of the fundamental is wider than those seen above. (Amplitude level: 243.2 mV = 800 kPa)

A.9 Measured calibration signals for 9 MHz

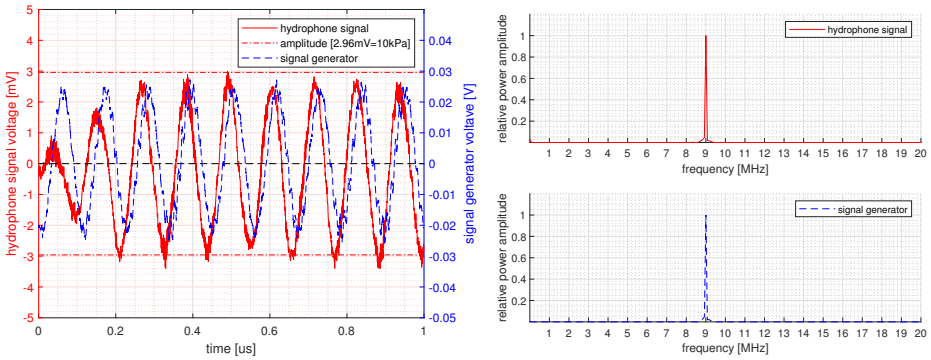

(a) time signal (b) frequency spectrum

Figure A.29:

Figure description: Measured signal voltages for 9 MHz at 10 kPa:

The time-domain signals are seen on the left (a) subfigure. The frequency spectrums are seen on the right (b) subfigure, with the hydrophone spectrum above the signal generator spectrum. The hydrophone voltage is red and signal generator voltage blue. There are no noticeable harmonics or signal distortion. The transducer takes one cycle to reach the desired pressure level. (Amplitude level: 2.96 mV = 10 kPa)

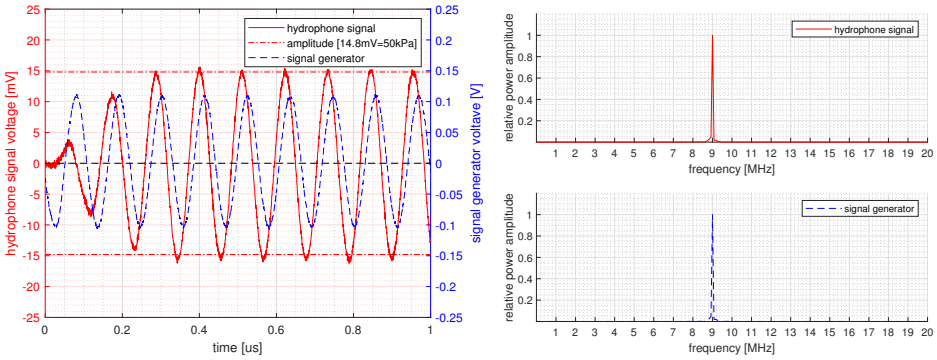

(a) time signal (b) frequency spectrum

Figure A.30:

Figure description: Measured signal voltages for 9 MHz at 50 kPa:

The time-domain signals are seen on the left (a) subfigure. The frequency spectrums are seen on the right (b) subfigure, with the hydrophone spectrum above the signal generator spectrum. The hydrophone voltage is red and signal generator voltage blue. There are no noticeable harmonics or signal distortion. The transducer takes one cycle to reach the desired amplitude. (Amplitude level: 14.8 mV = 50 kPa)

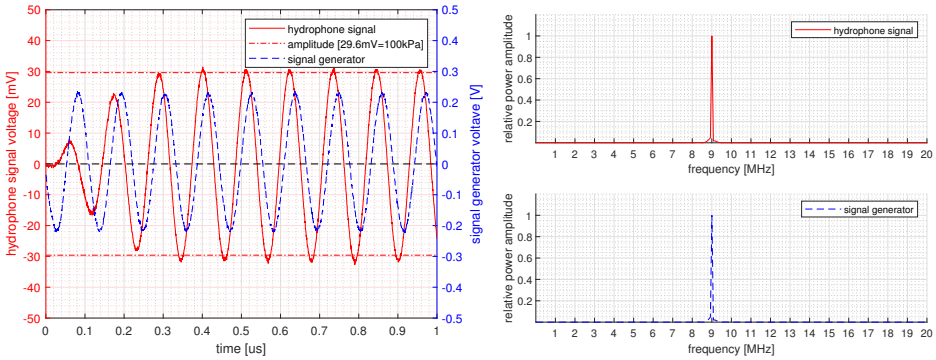

(a) time signal (b) frequency spectrum

Figure A.31:

Figure description: Measured signal voltages for 9 MHz at 100 kPa:

The time-domain signals are seen on the left (a) subfigure. The frequency spectrums are seen on the right (b) subfigure, with the hydrophone spectrum above the signal generator spectrum. The hydrophone voltage is red and signal generator voltage blue. There are no noticeable harmonics or signal distortion. The transducer takes one cycle to reach the desired pressure level. (Amplitude level: 29.6 mV = 100 kPa)

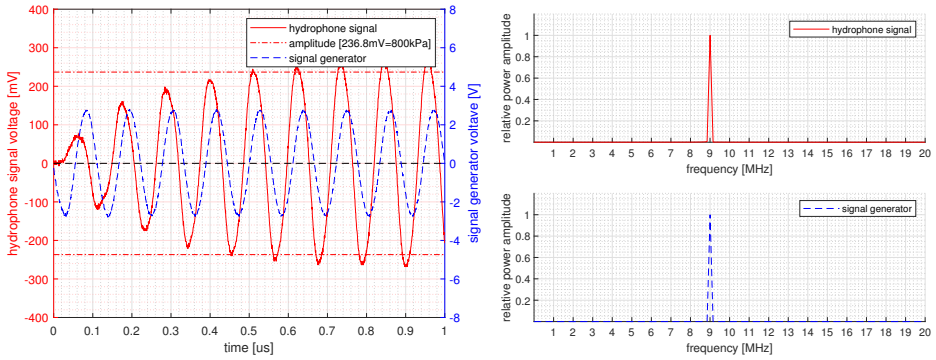

(a) time signal (b) frequency spectrum

Figure A.32:

Figure description: **Measured signal voltages for** 9 MHz **at** 800 kPa:

The time-domain signals are seen on the left (a) subfigure. The frequency spectrums are seen on the right (b) subfigure, with the hydrophone spectrum above the signal generator spectrum. The hydrophone voltage is red and signal generator voltage blue. There are no noticeable harmonics or signal distortion. The transducer takes three cycles to reach the desired pressure amplitude. (Amplitude level: 236.8 mV = 800 kPa)

A.10 Measured calibration signals for 10 MHz

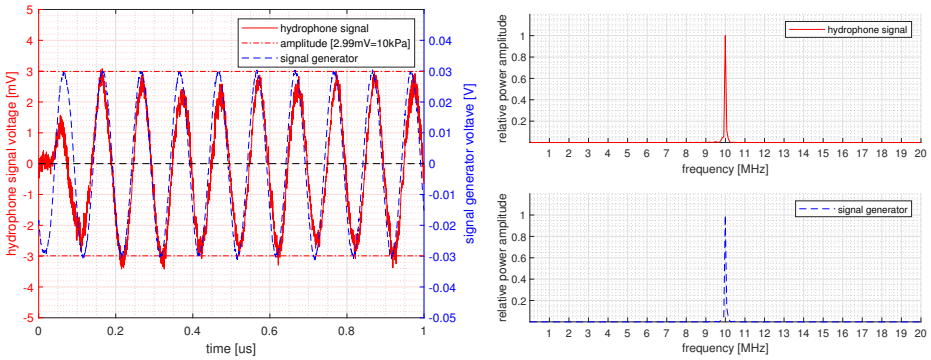

(a) time signal (b) frequency spectrum

Figure A.33:

Figure description: Measured signal voltages for 10 MHz at 10 kPa:

The time-domain signals are seen on the left (a) subfigure. The frequency spectrums are seen on the right (b) subfigure, with the hydrophone spectrum above the signal generator spectrum. The hydrophone voltage is red and signal generator voltage blue. There are no noticeable harmonics or signal distortion.(Amplitude level: 2.99 mV = 10 kPa)

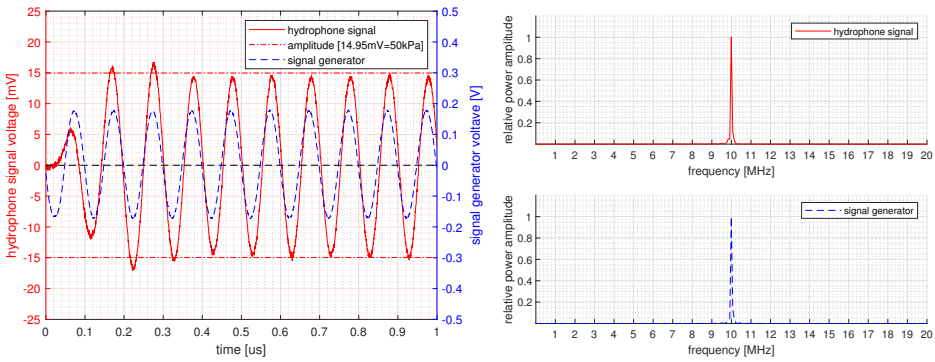

(a) time signal (b) frequency spectrum

Figure A.34:

Figure description: Measured signal voltages for 10 MHz at 50 kPa:

The time-domain signals are seen on the left (a) subfigure. The frequency spectrums are seen on the right (b) subfigure, with the hydrophone spectrum above the signal generator spectrum. The hydrophone voltage is red and signal generator voltage blue. There are no noticeable harmonics or signal distortion. The transducer takes one cycle to reach the desired amplitude. (Amplitude level: 14.95 mV = 50 kPa)

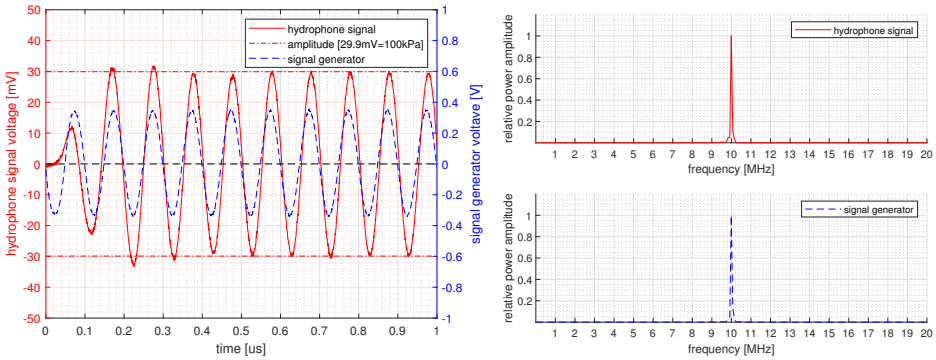

(a) time signal (b) frequency spectrum

Figure A.35:

Figure description: Measured signal voltages for 10 MHz at 100 kPa:

The time-domain signals are seen on the left (a) subfigure. The frequency spectrums are seen on the right (b) subfigure, with the hydrophone spectrum above the signal generator spectrum. The hydrophone voltage is red and signal generator voltage blue. There are no noticeable harmonics or signal distortion. The transducer signal takes one cycle to reach the desired amplitude. (Amplitude level: 29.9 mV = 100 kPa)

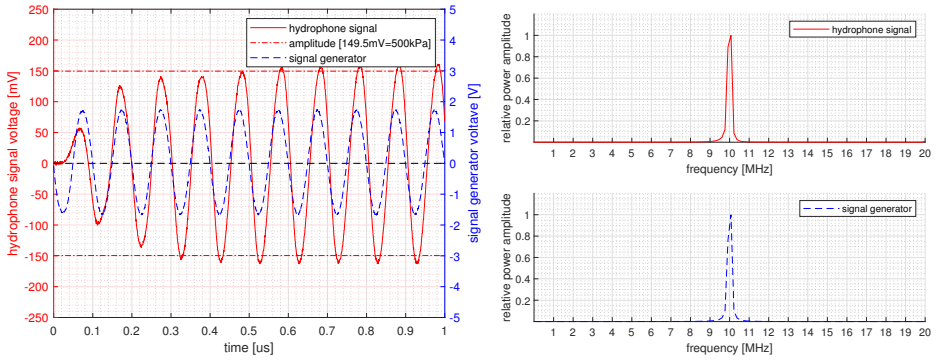

(a) time signal (b) frequency spectrum

Figure A.36:

Figure description: **Measured signal voltages for** 10 MHz **at** 500 kPa:

The time-domain signals are seen on the left (a) subfigure. The frequency spectrums are seen on the right (b) subfigure, with the hydrophone spectrum above the signal generator spectrum. The hydrophone voltage is red and signal generator voltage blue. There are no noticeable harmonics or signal distortion. However, the bandwidth of the fundamental is wider than those above. Additionally the transducer takes a couple of cycles to reach the desired signal amplitude (Amplitude level: 149.5 mV = 500 kPa)

Appendix B

Full experimental results

B.1 Partition coefficient vs acoustic pressure amplitude plots at a set frequency

The full results of the experiments are shown below. The figures are presented according to the experimental procedure; an experimental set at a constant control frequency, with the partition coefficient vs acoustic pressure amplitude. For each figure, there are three subplots. The left plot (a) shows the partition coefficients of the samples imaged at 2.5 min after being shaken. The centre (b) shows the partition coefficients of the samples imaged at 5 min. The right plot (c) shows the partition coefficients of the samples, after being reshaken at 5 min, and then imaged at 7.5 min (after a 2.5 min rest time). The partition coefficient plot points are also accompanied by their standard deviation error bars.

B.1.1 Null and actively exposed samples' differences

In all the resultant figures below, there is a clear difference between the null and actively exposed samples. The null samples collectively have a partition coefficient of 1.12 with a standard deviation of 0.16 (for the centre (b) plots). For each control frequency and control amplitude, the exposed samples have a partition coefficient value consistently

less than the null experiment partition coefficient. There is some variation in the value over the control frequencies and control pressures.

B.1.2 Comparison between the experimental image sets

When comparing the results between the experimental sets (i.e. the different imaging times and the re-shaken sample) there are some apparent features. Firstly, when comparing the results of the samples imaged at 2.5 min and 5 min (left and centre graphs), there is no significant difference in the corresponding pressure values for the given control frequency. However, the results of the reshaken samples (the right graphs) are distinctly different, with a comparatively more positive partition coefficient than the other two. This is a clear and consistent difference between the two 2.5 min and 5 min results, which are just imaged, and the 7.5 min results of the reshaken samples across all the test frequencies and pressures.

B.1.3 Overall shape of the plots

Apart from some specific experimental results in the graphs below, the partition coefficient values are mostly similar. However, there is a noticeable shape of the plots. The partition coefficient vs acoustic amplitude graph has a minima between 10 to 40 kPa, a maxima between 40 to 60 kPa, and another minima again between 60 to 90 kPa, as a general trend. There is also a seemingly steeper positive gradient at 100 kPa. These features are, however, negligible when comparing the values to the global results, and overall the shape follows a horizontal line.

B.1.4 Figures of the standard pressure range

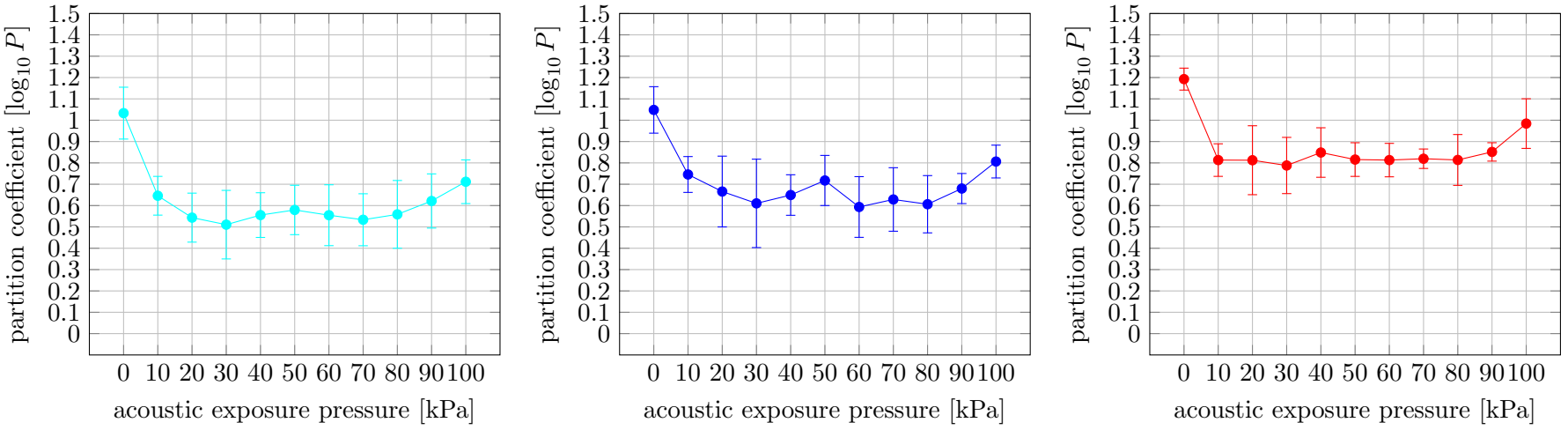

(a) imaged at 2.5 min

(b) imaged at 5 min

(c) imaged at 7.5 min

Figure B.1: Partition coefficients of hydrophobic microparticles exposed to an acoustic frequency of 1MHz

Figure description: The plot follows a general trend as described above in the beginning of this appendix. There is a noticeable peak at 50 kPa and 100 kPa for subfigures (a) and (b). The mean partition coefficient for the actively exposed samples is 0.58 ± 0.14, 0.67 ± 0.15 and 0.84 ± 0.12 for subfigures (a), (b) and (c) respectively.

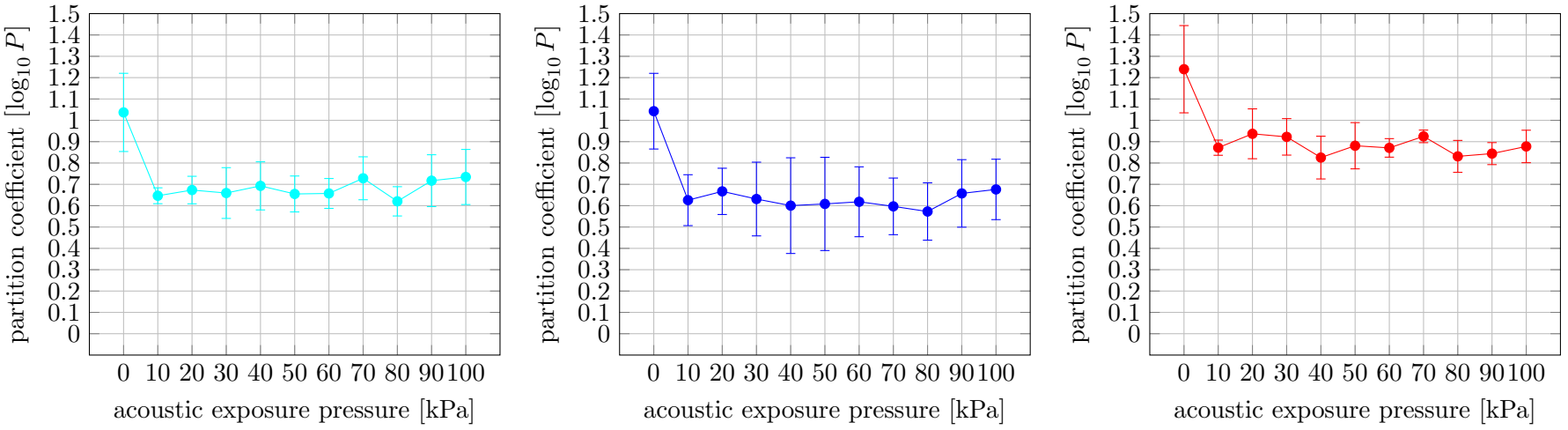

(a) imaged at 2.5 min

(b) imaged at 5 min

(c) imaged at 7.5 min

Figure B.2: Partition coefficients of hydrophobic microparticles exposed to an acoustic frequency of 2MHz

Figure description: The plot follows a general trend as described above in the beginning of this appendix. The only exception is that the shape of the plots here are flatter (compared to other frequencies). There is however a small valley at 80 kPa for all three subfigures. The mean partition coefficient for the actively exposed samples is 0.68 ± 0.10, 0.63 ± 0.16 and 0.88 ± 0.09 for subfigures (a), (b) and (c) respectively.

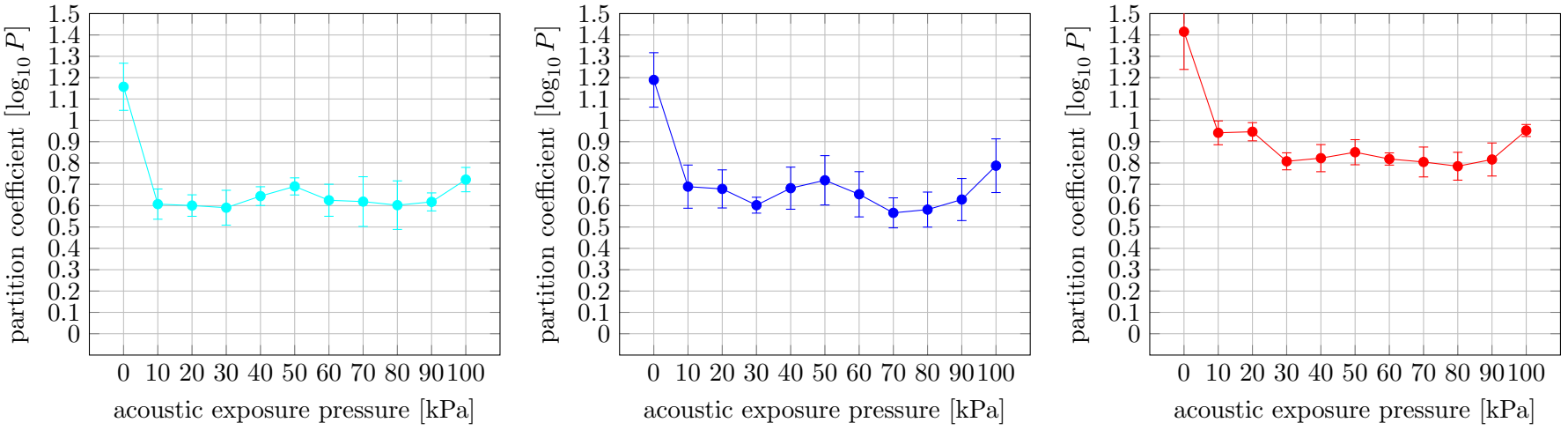

(a) imaged at 2.5 min

(b) imaged at 5 min

(c) imaged at 7.5 min

Figure B.3: Partition coefficients of hydrophobic microparticles exposed to an acoustic frequency of 3MHz

Figure description: The plot follows a general trend as described above in the beginning of this appendix. There is a noticeable peak at 50 kPa and 100 kPa for each of the three subfigures. There is a clear minimum partition coefficient occurring between 70 kPa to 80 kPa in all three subfigures. The the standard deviation is lowest for data in subfigures (a) and (c). The mean partition coefficient for the actively exposed samples is 0.63 ± 0.08, 0.66 ± 0.11 and 0.85 ± 0.08 for subfigures (a), (b) and (c) respectively.

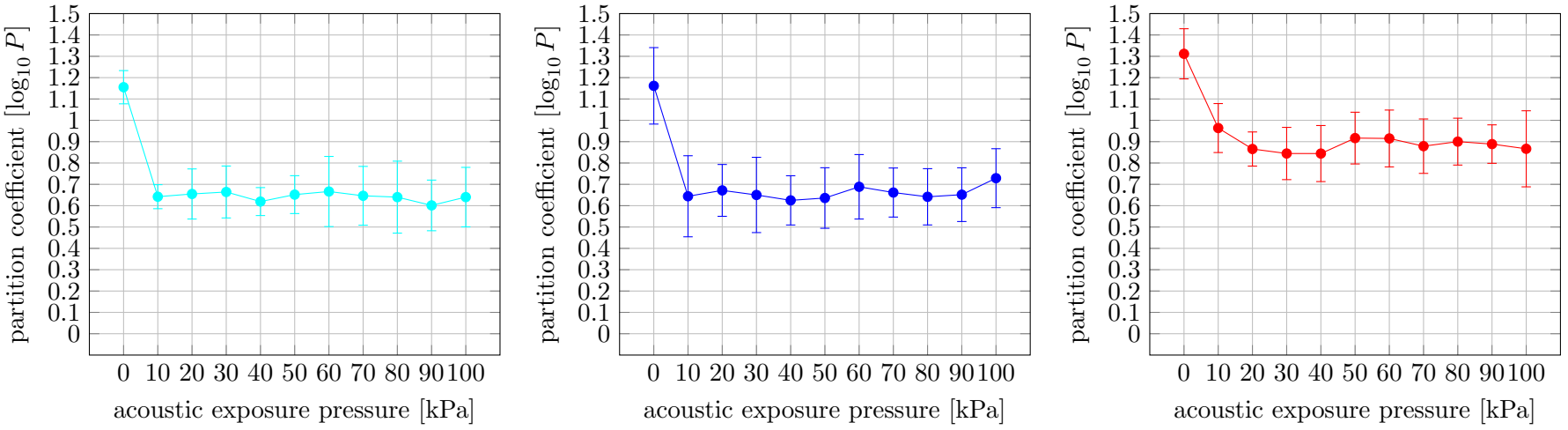

(a) imaged at 2.5 min

(b) imaged at 5 min

(c) imaged at 7.5 min

Figure B.4: Partition coefficients of hydrophobic microparticles exposed to an acoustic frequency of 4MHz

Figure description: The plot follows a general trend as described above in the beginning of this appendix. The only exception is that the shape of the plots here are flatter (compared to other frequencies). There is a perceivable peak occurring at ≈60 kPa, however is not as prominent. Additionally there is a minimum that occurs at 40 kPa though is also not prominent. The mean partition coefficient for the actively exposed samples is 0.64 ± 0.12, 0.66 ± 0.15 and 0.89 ± 0.13 for subfigures (a), (b) and (c) respectively.

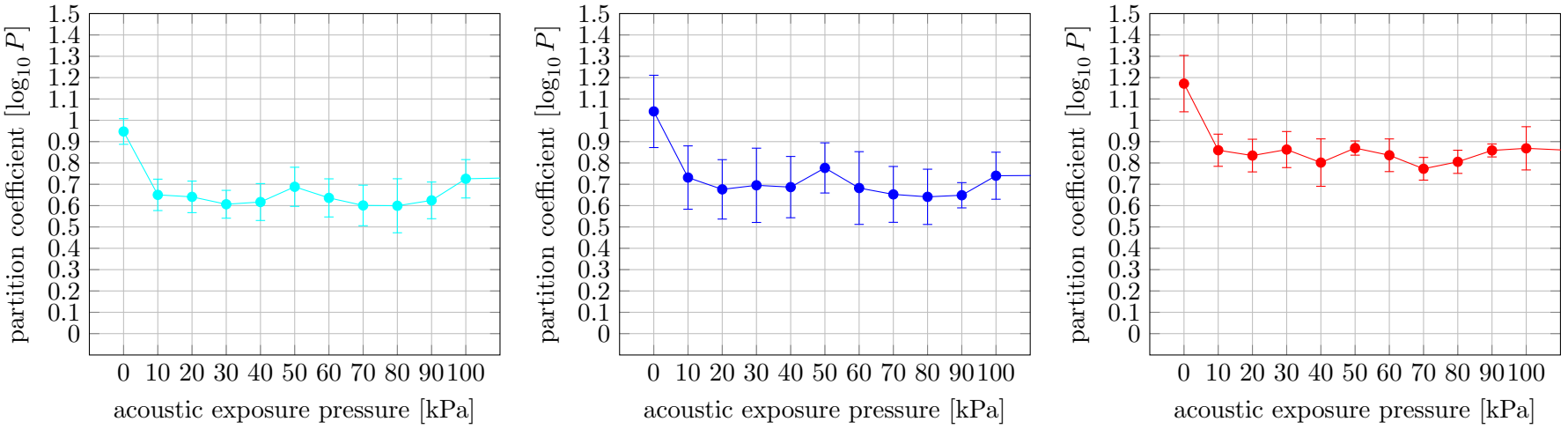

(a) imaged at 2.5 min

(b) imaged at 5 min

(c) imaged at 7.5 min

Figure B.5: Partition coefficients of hydrophobic microparticles exposed to an acoustic frequency of 5MHz

Figure description: The plot follows a general trend as described above in the beginning of this appendix. Noticeably the standard deviations of the data in subfigures (a) and (c) are comparatively smaller than that seen in subfigure (b). There is a perceivable minimum that occurs between 70 kPa and 80 kPa. Additionally there is a peak at 50 kPa. The mean partition coefficient for the actively exposed samples is 0.65 ± 0.10, 0.70 ± 0.13 and 0.83 ± 0.08 for subfigures (a), (b) and (c) respectively.

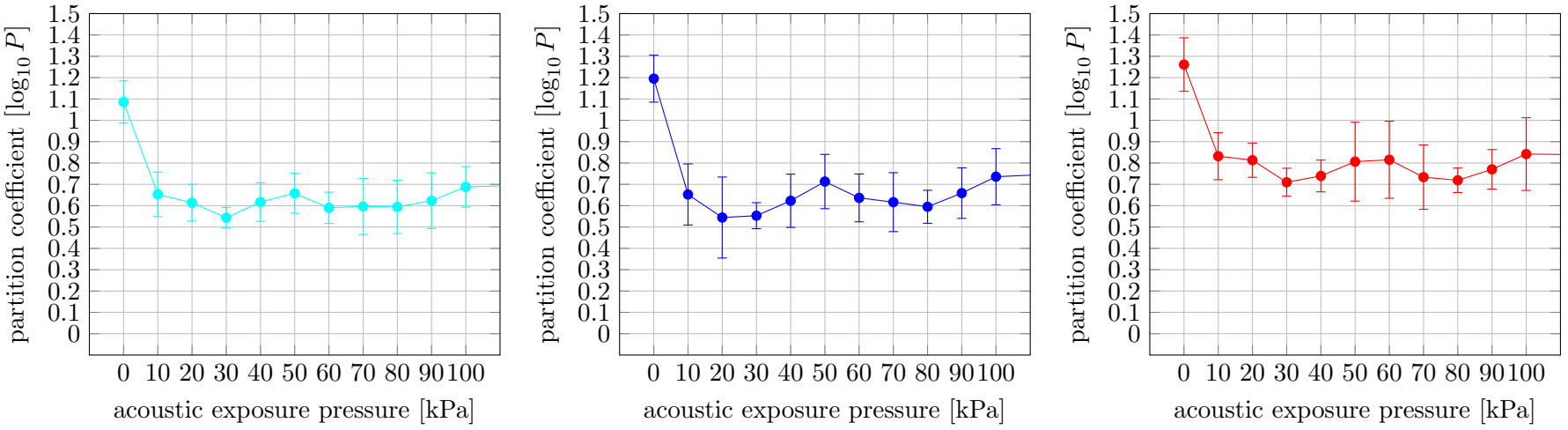

(a) imaged at 2.5 min

(b) imaged at 5 min

(c) imaged at 7.5 min

Figure B.6: Partition coefficients of hydrophobic microparticles exposed to an acoustic frequency of 6MHz

Figure description: The plot follows a general trend as described above in the beginning of this appendix. There is a perceivable peak occurring at 50 kPa in all three subfigures. Additionally there are two minimum values that occur through all three subfigures, at 30 kPa and 70 kPa. The mean partition coefficient for the actively exposed samples is 0.64 ± 0.11, 0.65 ± 0.14 and 0.80 ± 0.14 for subfigures (a), (b) and (c) respectively.

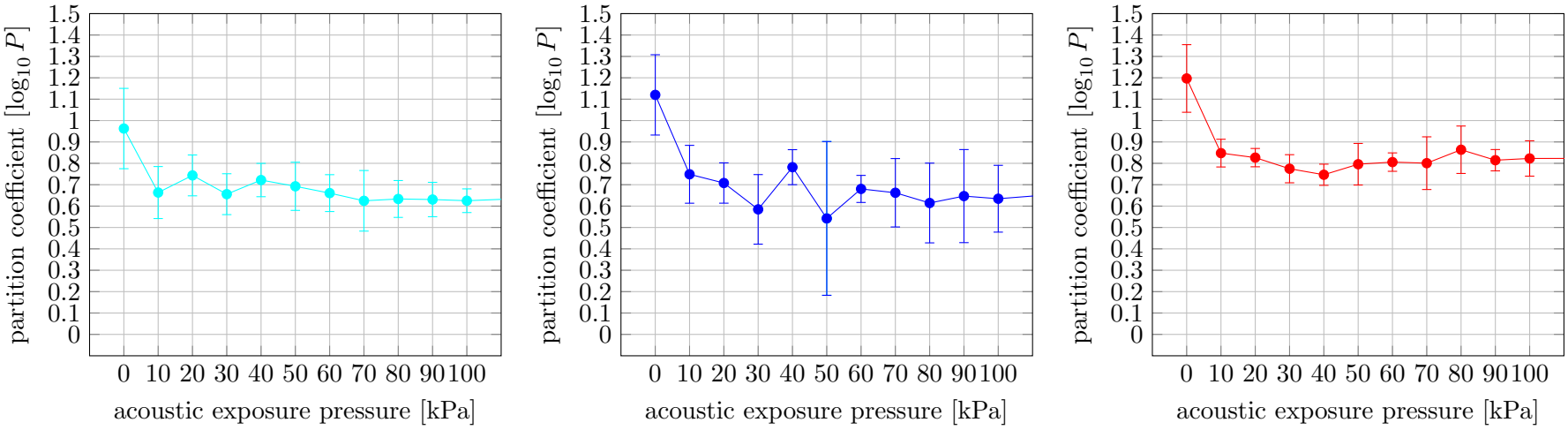

(a) imaged at 2.5 min

(b) imaged at 5 min

(c) imaged at 7.5 min

Figure B.7: Partition coefficients of hydrophobic microparticles exposed to an acoustic frequency of 7MHz

Figure description: The plot follows a general trend as described above in the beginning of this appendix. The only exception is that the shape of the plots here are flatter (compared to other frequencies), particularly for subfigures (a) and (c). There is a perceivable valley at 30 kPa and peak at 40 kPa in subfigure (b). For subfigure (b), there is an outlier correction at 50 kPa (for one of the images, the partition coefficient calculated for 50 kPa was -0.16. This is not consistent with the rest of the data). The outlier's effect on the data is indicated in the plot in cyan as an indicator for justifying its omission for further discussion. The mean partition coefficient for the actively exposed samples is 0.66 ± 0.10, 0.67 ± 0.17 and 0.82 ± 0.10 for subfigures (a), (b) and (c) respectively.

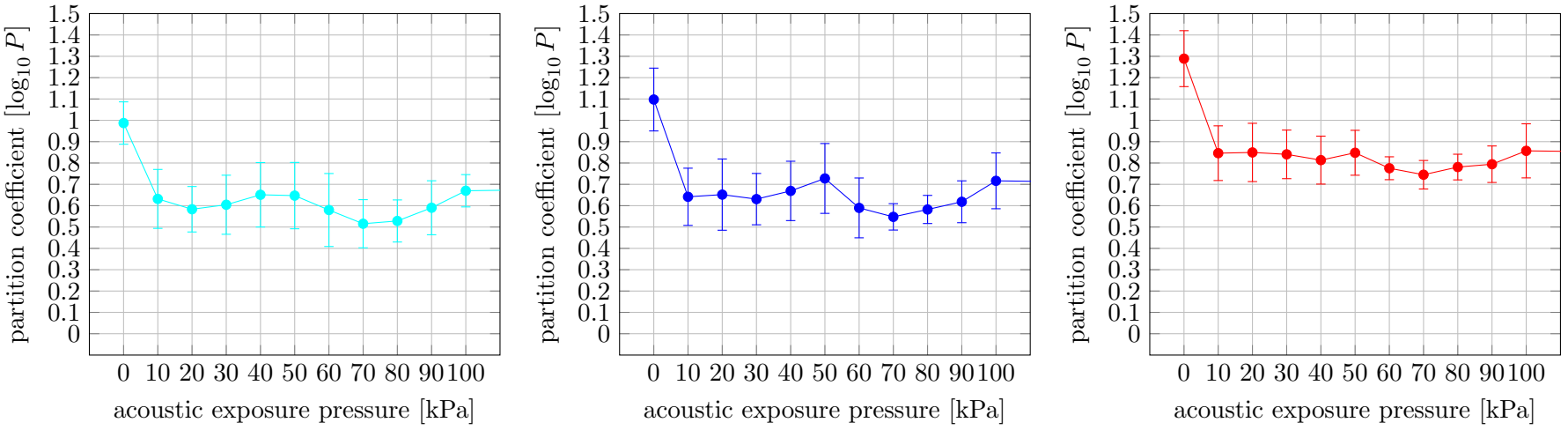

(a) imaged at 2.5 min

(b) imaged at 5 min

(c) imaged at 7.5 min

Figure B.8: Partition coefficients of hydrophobic microparticles exposed to an acoustic frequency of 8MHz

Figure description: The plot follows a general trend as described above in the beginning of this appendix. There is a perceivable minimum that occurs at 70 kPa, additionally there is a peak at 50 kPa, for all three subfigures. The mean partition coefficient for the actively exposed samples is 0.62 ± 0.13, 0.64 ± 0.13 and 0.83 ± 0.11 for subfigures (a), (b) and (c) respectively.

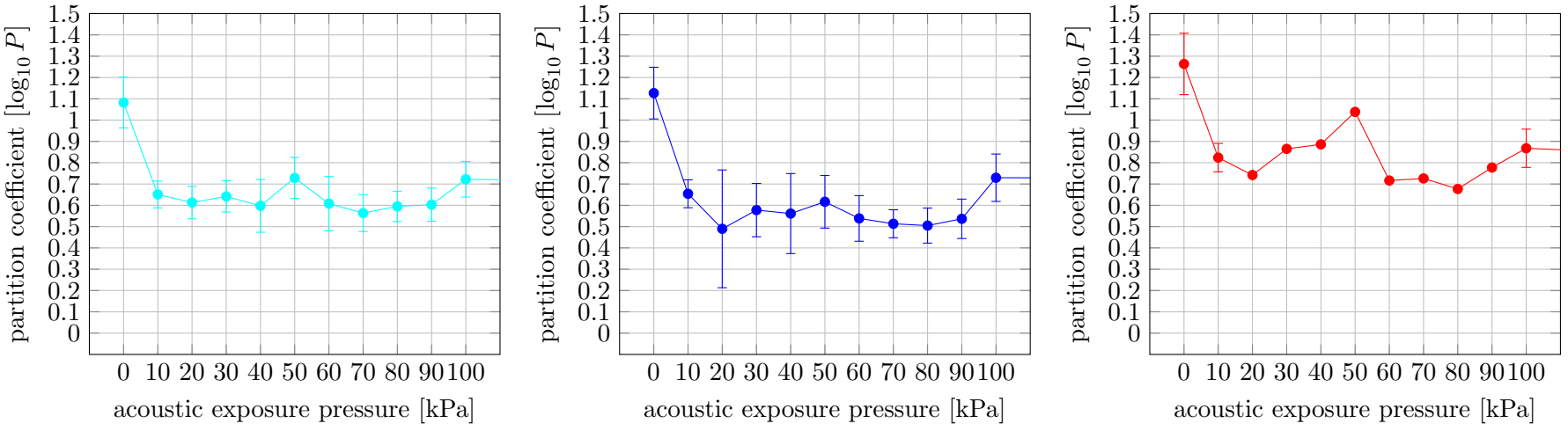

(a) imaged at 2.5 min

(b) imaged at 5 min

(c) imaged at 7.5 min

Figure B.9: Partition coefficients of hydrophobic microparticles exposed to an acoustic frequency of 9MHz

Figure description: The plot follows a general trend as described above in the beginning of this appendix. There is a perceivable minimum that occurs between 70 kPa and 80 kPa. Additionally there is a peak at 50 kPa. The mean partition coefficient for the actively exposed samples is 0.66 ± 0.16, 0.62 ± 0.15 and 0.81 ± 0.10 for subfigures (a), (b) and (c) respectively. The standard deviation is unusually large for 20 kPa but is not detrimental for further analysis.

An important remark is that the data in the range 20 kPa to 90 kPa for subfigure (c) does not have error bars. These experiments unfortunately only had one usable image set. However the data are still used to indicate the general trend, and it loosely fits with the general trend discussed. The data at 0 i, 10 i and 100 is incorporated with the data from the extended pressure experiments to make it more usable here.

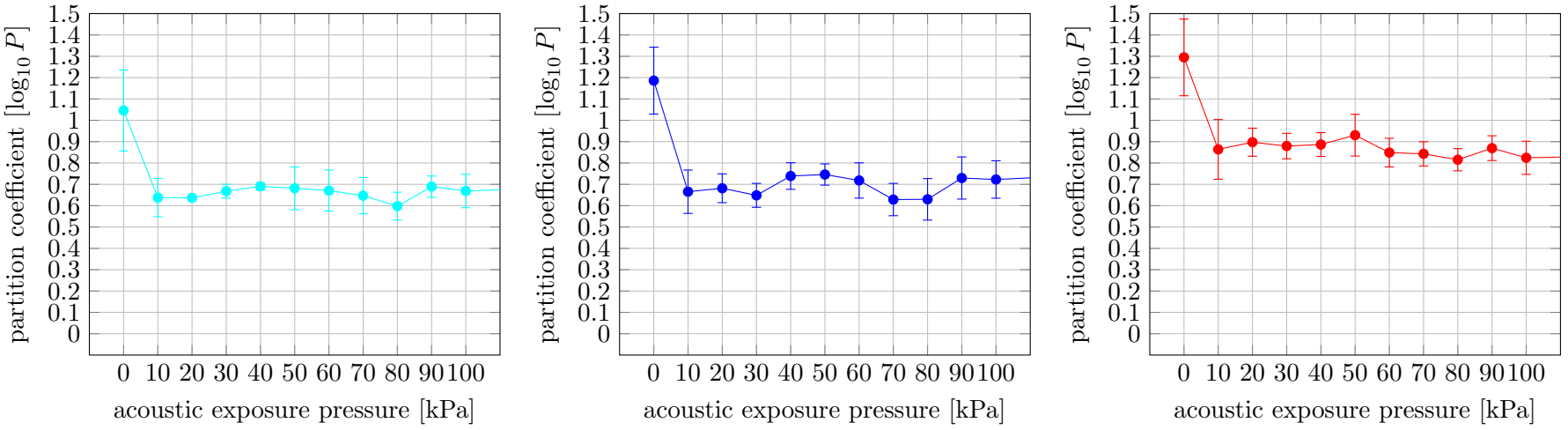

(a) imaged at 2.5 min

(b) imaged at 5 min

(c) imaged at 7.5 min

Figure B.10: Partition coefficients of hydrophobic microparticles exposed to an acoustic frequency of 10MHz

Figure description: The plot follows a general trend as described above in the beginning of this appendix. There is a perceivable minimum that occurs at 80 kPa, additionally there is a peak at 50 kPa, for all three subfigures. The mean partition coefficient for the actively exposed samples is 0.67 ± 0.09, 0.70 ± 0.09 and 0.85 ± 0.09 for subfigures (a), (b) and (c) respectively.

B.1.5 Figures of the extended pressure range

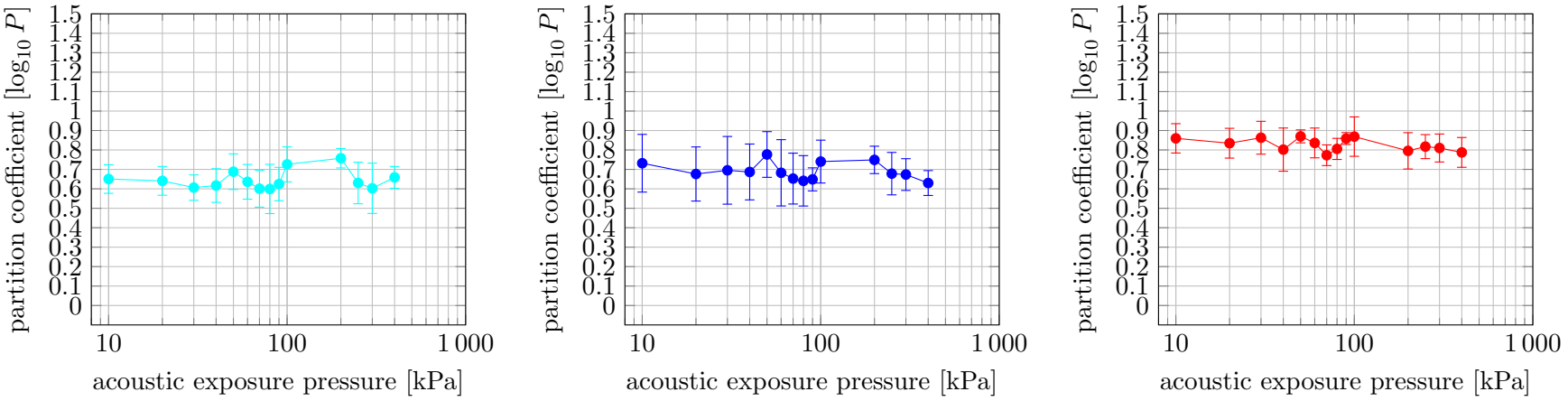

(a) imaged at 2.5 min

(b) imaged at 5 min

(c) imaged at 7.5 min

Figure B.11: Partition coefficients of hydrophobic microparticles exposed to an acoustic frequency of 5MHz at pressures >100 kPa

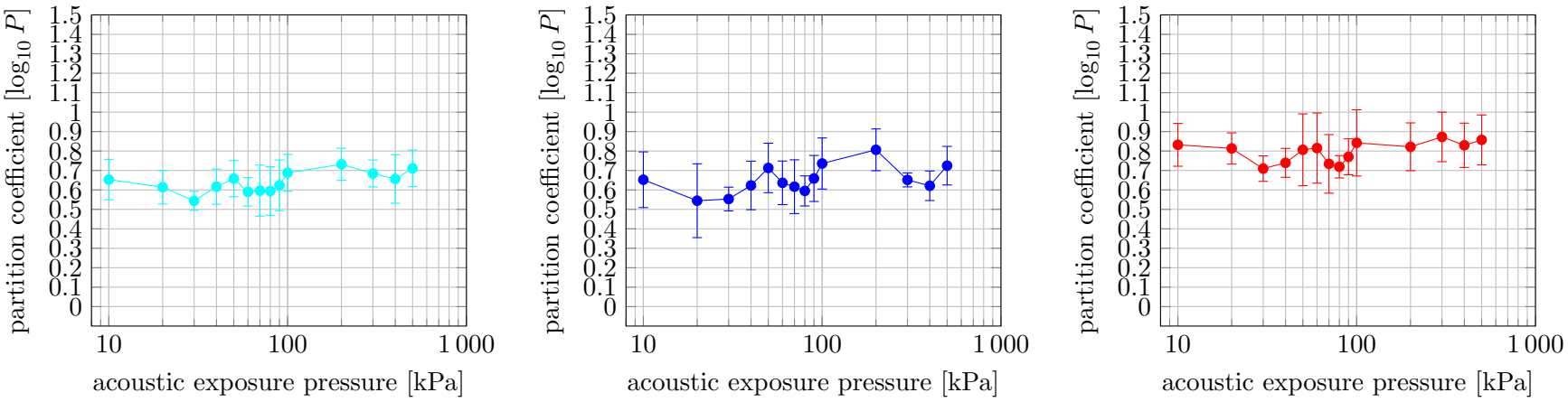

(a) imaged at 2.5 min (b) imaged at 5 min (c) imaged at 7.5 min

Figure B.12: Partition coefficients of hydrophobic microparticles exposed to an acoustic frequency of 6MHz at pressures >100 kPa

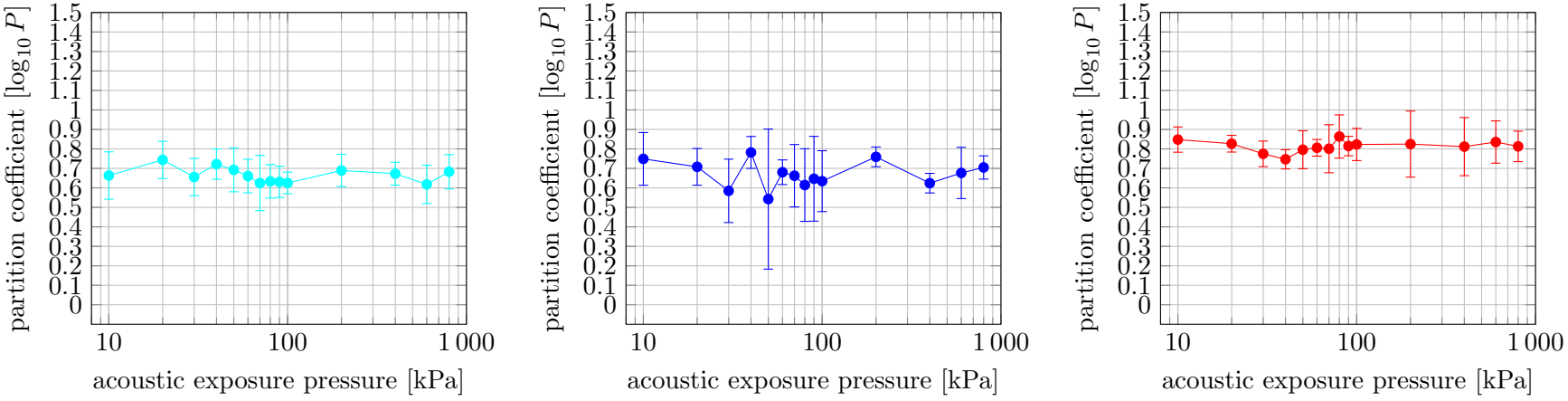

(a) imaged at 2.5 min (b) imaged at 5 min (c) imaged at 7.5 min

Figure B.13: Partition coefficients of hydrophobic microparticles exposed to an acoustic frequency of 7MHz at pressures >100 kPa

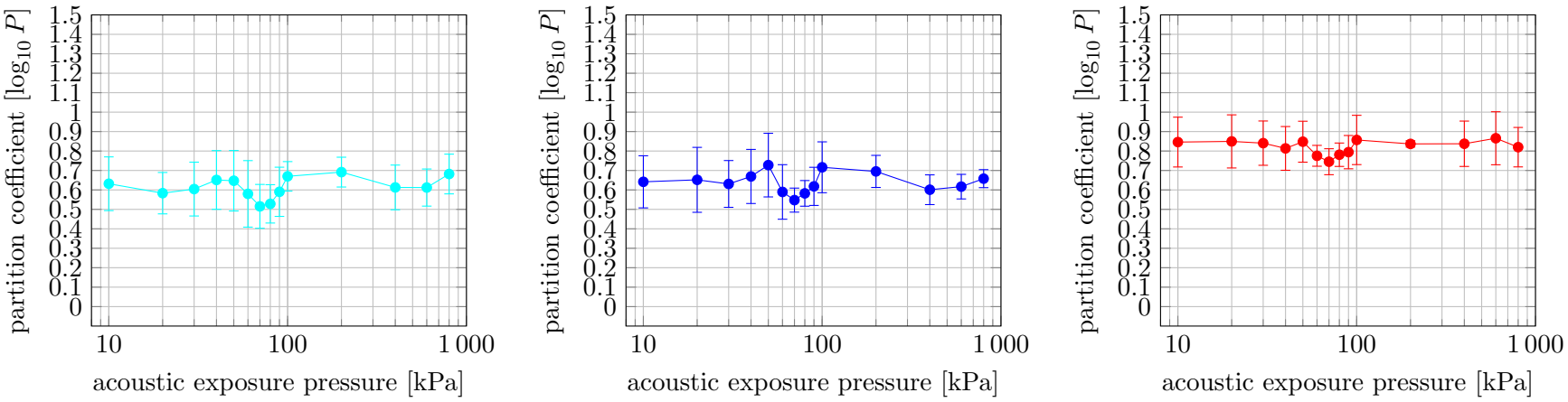

(a) imaged at 2.5 min (b) imaged at 5 min (c) imaged at 7.5 min

Figure B.14: Partition coefficients of hydrophobic microparticles exposed to an acoustic frequency of 8MHz at pressures >100 kPa

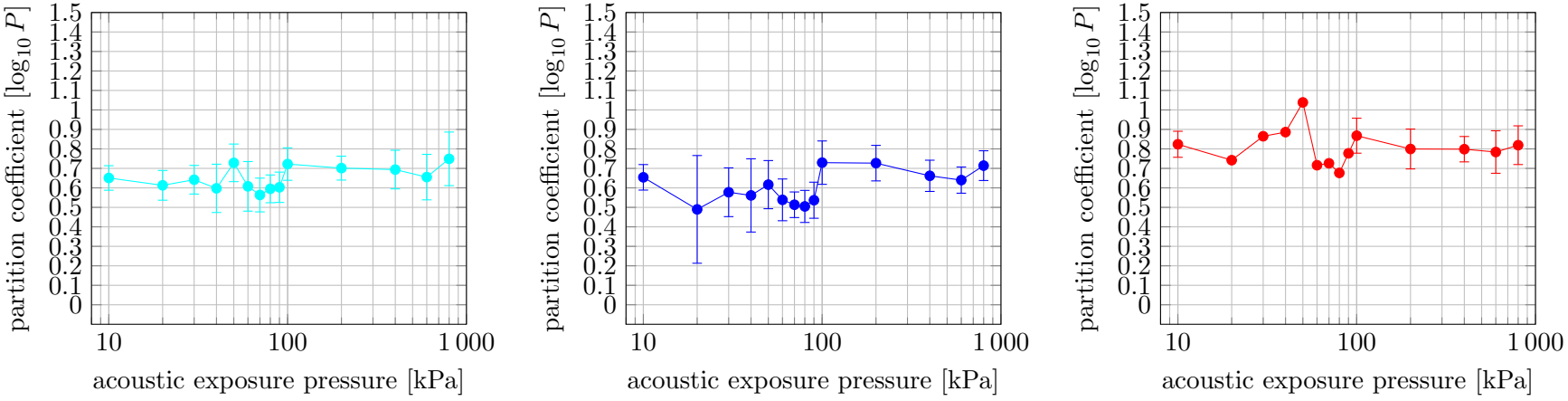

(a) imaged at 2.5 min (b) imaged at 5 min (c) imaged at 7.5 min

Figure B.15: Partition coefficients of hydrophobic microparticles exposed to an acoustic frequency of 9MHz at pressures >100 kPa

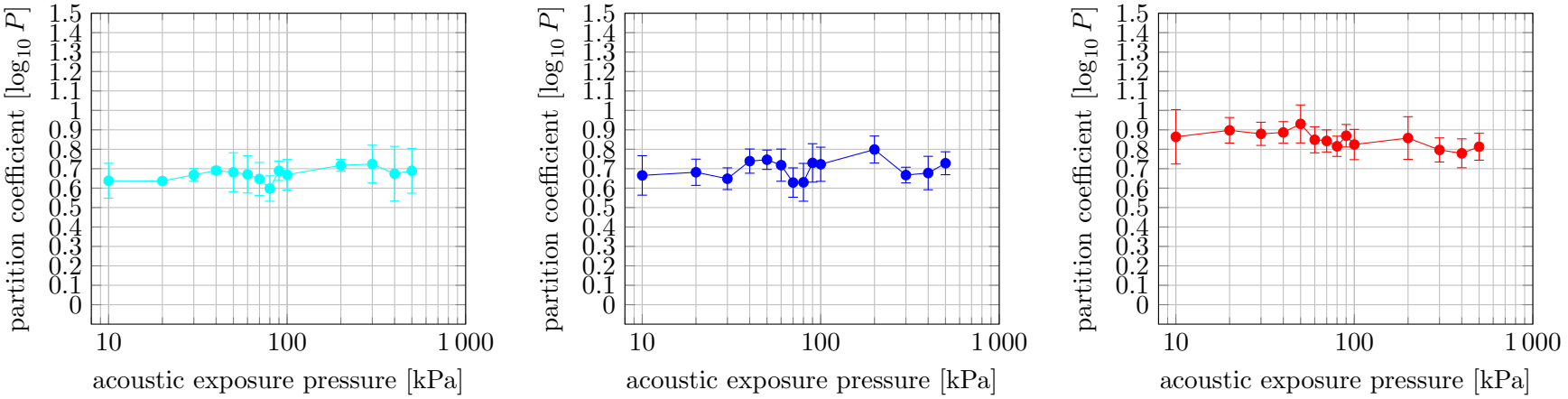

(a) imaged at 2.5 min

(b) imaged at 5 min

(c) imaged at 7.5 min

Figure B.16: Partition coefficients of hydrophobic microparticles exposed to an acoustic frequency of 10MHz at pressures >100 kPa

Appendix C

Colourimetry partition coefficient calculation

The fundamental mathematical equation for calculating the partition coefficient using the principles of colourimetry is discussed here in detail. The resulting digital image processing (DIP) equation is implemented in-code as seen in Appendix D. The fundamental objective of the code is to locate the relevant regions of interest (ROIs) of the samples in the images and perform digital processing to calculate the partition coefficient of the samples in the digital image. The derivation of the Colourimetric Partition Coefficient Equation 3.4 is now covered.

The concentrations of the carbon black microparticles, in the octanol and water phases of the samples, need to be determined to calculate the partition coefficient. This is done through image colourimetry in each phase. The transmitted light intensity of a solution is characterised by the Intensity Absorbance Equation C.1 [1],

$$I = I_0 e^{-A} \tag{C.1}$$

where, I is the transmitted light intensity; I_0 is the incident light intensity; and A is the optical molar absorptivity, the medium's optical properties.

Additionally, the optical molar absorptivity is further related to the optical molar attenuation coefficient ε, the concentration of the substance c_x, and the optical path length l. The equation relating these parameters is the Beer-Lambert Law [1]. The parameters are modified here to represent the equation for carbon black microparticles (cbmp) in the respective phase,

$$A^{\varphi}_{\text{cbmp}} = \varepsilon_{\text{cbmp}} c^{\varphi}_{\text{cbmp}} l_0 \tag{C.2}$$

The optical molar attenuation coefficient $\varepsilon_{\text{cbmp}}$ is constant under the experimental conditions of this research. The optical path length l_0 is also kept constant by the imaging

setup as explained in Section 3.5. Therefore, for a given phase φ (either octanol or water), the resultant phase-specific optical molar absorptivity is

$$\begin{aligned} A^{\varphi}_{\text{cbmp}} &= \varepsilon_{\text{cbmp}} c^{\varphi}_{\text{cbmp}} l_0 \\ &= \alpha_{\text{cbmp}} c^{\varphi}_{\text{cbmp}} \end{aligned} \tag{C.3}$$

The α_{cbmp} value is inherent to the optical properties of the microparticles under this constant path length l_0, regardless of the phase φ.

However, each optical medium φ, both for octanol and water phases and even the cuvette material itself, has its own non-zero optical attenuation. These attenuations could be but are not necessarily negligible. The attenuation is accounted for as an effective attenuation parameter determined using a calibration reference (the clear octanol-water reference). This calibration reference is then used for compensating the non-zero attenuation in the final partition coefficient calculation. The resultant absorptivity due to the phase and cuvette is additive. Subsequently, the effective attenuation coefficient of multicomponent materials is simply the appropriately weighted sum of the attenuation coefficients ε_x and relevant path lengths [1]. In this case, the weighting is the corresponding materials' molar concentration. However, the molar concentration of the phase and cuvette is replaced with the molar density.

$$B_{\varphi\nu} = \beta_{\varphi} + \beta_{\nu} \tag{C.4}$$

$$= \varepsilon_{\varphi} \rho_{\text{mol}_{\varphi}} l_0 + \varepsilon_{\nu} \rho_{\text{mol}_{\nu}} \chi \tag{C.5}$$

where, $B_{\varphi\nu}$ is the effective absorptivity of the phase φ (octanol or water) and the cuvette material ν; β_{φ} and β_{ν} are the optical absorptivity of the specific phase φ (octanol or water) and cuvette ν components; ε_{φ} and ε_{ν} are the optical molar-density attenuation coefficients, for the phase φ (octanol or water) and the cuvette ν; $\rho_{\text{mol}_{\varphi}}$ and $\rho_{\text{mol}_{\nu}}$ are the molar densities of the octanol or water phase φ, and the cuvette ν (in place of the concentration since the concentration of the pure solvent and cuvette material is meaningless); l_0 is the optical path length in the octanol or water phase φ (same as the optical path for the microparticles), and χ is the total optical path length through both sides of the cuvette.

The exact values of the molar densities, the phase path length, and the cuvette thickness are unimportant, as will be demonstrated later. The effective total absorptivity of the

entire sample is then given by the weighted sum as follows,

$$A^{\varphi}_{\text{cbmp}_{\text{eff}}} = A^{\varphi}_{\text{cbmp}} + B_{\varphi\nu} \tag{C.6}$$

$$= \varepsilon_{\text{cbmp}} c^{\varphi}_{\text{cbmp}} l_0 + \varepsilon_{\varphi} \rho_{\text{mol}_{\varphi}} l_0 + \varepsilon_{\nu} \rho_{\text{mol}_{\nu}} \chi \tag{C.7}$$

The effective total transmitted intensity equation for the microparticles in a given phase φ is then simply

$$I^{\varphi}_{\text{cbmp}_{\text{eff}}} = I_0 e^{-A^{\varphi}_{\text{cbmp}_{\text{eff}}}} \tag{C.8}$$

$$= I_0 e^{-\left(A^{\varphi}_{\text{cbmp}} + B_{\varphi\nu}\right)} \tag{C.9}$$

$$= I_0 e^{-B_{\varphi\nu}} e^{-A^{\varphi}_{\text{cbmp}}} \tag{C.10}$$

$$= I_{\text{eff}_{\varphi}} e^{\left(-\alpha_{\text{cbmp}} c^{\varphi}_{\text{cbmp}}\right)} \tag{C.11}$$

where, $I^{\varphi}_{\text{cbmp}_{\text{eff}}}$ is the effective transmitted light intensity, passing through the cuvette, phase and carbon black microparticles; $I_{\text{eff}_{\varphi}}$ is the effective intensity of light due to only the cuvette and phase, i.e. the transmitted light through the cuvette and phase only. Therefore, the effective intensity of a sample in both the octanol and water phase is then,

$$I^{\text{oct}}_{\text{cbmp}_{\text{eff}}} = I_{\text{eff}_{\text{oct}}} e^{\left(-\alpha_{\text{cbmp}}\ c^{\text{oct}}_{\text{cbmp}}\right)} \qquad I^{\text{wat}}_{\text{cbmp}_{\text{eff}}} = I_{\text{eff}_{\text{wat}}} e^{\left(-\alpha_{\text{cbmp}}\ c^{\text{wat}}_{\text{cbmp}}\right)} \tag{C.12}$$

where, $I^{\text{oct}}_{\text{cbmp}_{\text{eff}}}$ and $I^{\text{wat}}_{\text{cbmp}_{\text{eff}}}$ are the total multicomponent transmitted light intensities due to the entire sample in the octanol and water phases, respectively; $I_{\text{eff}_{\text{oct}}}$ and $I_{\text{eff}_{\text{wat}}}$ are the effective transmitted light intensities of the cuvettes and respective octanol and water phases; α_{cbmp} is the attenuation coefficient for carbon black microparticles;$c^{\text{oct}}_{\text{cbmp}}$ and$c^{\text{wat}}_{\text{cbmp}}$ are the concentrations of carbon black microparticles in each respective octanol and water phase (these are the variables of interest regarding the partition coefficient).

The molar densities of the octanol and water phases, the molar density of the cuvette, and the cuvette thickness, are all lumped into the respective phase's effective transmitted light intensities $I_{\text{eff}_{\varphi}}$. Therefore, their respective explicit values are unimportant (as mentioned earlier). The microparticle concentration for each phase in the respective

exponential equations can be isolated by rearranging the terms, giving

$$\begin{aligned}
\frac{I^{\text{oct}}_{\text{cbmp}_{\text{eff}}}}{I_{\text{eff}_{\text{oct}}}} &= e^{-\alpha_{\text{cbmp}}\ c^{\text{oct}}_{\text{cbmp}}} & \frac{I^{\text{wat}}_{\text{cbmp}_{\text{eff}}}}{I_{\text{eff}_{\text{wat}}}} &= e^{-\alpha_{\text{cbmp}}\ c^{\text{wat}}_{\text{cbmp}}} \\
e^{\alpha_{\text{cbmp}}\ c^{\text{oct}}_{\text{cbmp}}} &= \frac{I_{\text{eff}_{\text{oct}}}}{I^{\text{oct}}_{\text{cbmp}_{\text{eff}}}} & e^{\alpha_{\text{cbmp}}\ c^{\text{wat}}_{\text{cbmp}}} &= \frac{I_{\text{eff}_{\text{wat}}}}{I^{\text{wat}}_{\text{cbmp}_{\text{eff}}}} \\
\alpha_{\text{cbmp}}\ c^{\text{oct}}_{\text{cbmp}} &= \ln\left(\frac{I_{\text{eff}_{\text{oct}}}}{I^{\text{oct}}_{\text{cbmp}_{\text{eff}}}}\right) & \alpha_{\text{cbmp}}\ c^{\text{wat}}_{\text{cbmp}} &= \ln\left(\frac{I_{\text{eff}_{\text{wat}}}}{I^{\text{wat}}_{\text{cbmp}_{\text{eff}}}}\right) \\
c^{\text{oct}}_{\text{cbmp}} &= \frac{1}{\alpha_{\text{cbmp}}}\ln\left(\frac{I_{\text{eff}_{\text{oct}}}}{I^{\text{oct}}_{\text{cbmp}_{\text{eff}}}}\right) & c^{\text{wat}}_{\text{cbmp}} &= \frac{1}{\alpha_{\text{cbmp}}}\ln\left(\frac{I_{\text{eff}_{\text{wat}}}}{I^{\text{wat}}_{\text{cbmp}_{\text{eff}}}}\right)
\end{aligned} \tag{C.13}$$

The intensities, although strictly having units of $\mathrm{W\,m^{-2}}$, are converted by the digital camera to a digital pixel value (between 0 to 255). However, the Equations C.13 only have intensity ratios and the actual units are not fundamentally important. Using Equation 2.2 and using the expression for the concentrations ${c_{\text{cbmp}}}^{\text{oct}}$ and ${c_{\text{cbmp}}}^{\text{wat}}$ from Equation C.13 above, the partition coefficient as a function of the sample's light intensities through each partitioning phase is then

$$\log_{10} P = \log_{10}\left(\frac{\frac{1}{\alpha_{\text{cbmp}}}\ln\left(\frac{I_{\text{eff}_{\text{oct}}}}{I^{\text{oct}}_{\text{cbmp}_{\text{eff}}}}\right)}{\frac{1}{\alpha_{\text{cbmp}}}\ln\left(\frac{I_{\text{eff}_{\text{wat}}}}{I^{\text{wat}}_{\text{cbmp}_{\text{eff}}}}\right)}\right)$$

The specific lumped optical molar-path-length attenuation coefficient α_{cbmp} cancels out, and its specific value is unimportant for the experimental quantification of the partition coefficient. This then simplifies to the DIP Colourimetric Partition Coefficient Equation C.14,

$$\log_{10} P = \log_{10}\left(\frac{\ln\left(\frac{I_{\text{eff}_{\text{oct}}}}{I^{\text{oct}}_{\text{cbmp}_{\text{eff}}}}\right)}{\ln\left(\frac{I_{\text{eff}_{\text{wat}}}}{I^{\text{wat}}_{\text{cbmp}_{\text{eff}}}}\right)}\right) \tag{C.14}$$

To clarify, $I_{\text{eff}_{\text{oct}}}$ is the mean pixel value in the ROI of the clear reference's octanol phase; $I_{\text{eff}_{\text{wat}}}$ is the mean pixel value in the ROI of the clear reference's water phase; $I^{\text{oct}}_{\text{cbmp}_{\text{eff}}}$ is the mean pixel value in the ROI of the sample's octanol phase; and $I^{\text{wat}}_{\text{cbmp}_{\text{eff}}}$ is the mean pixel value in the ROI of the sample's water phase;

References

[1] E. B. Podgorsak, *Radiation Physics for Medical Physicists*. Springer, 2016, ISBN: 9783319253800.

Appendix D

Matlab source code

This appendix provides an overview of the MATLAB source code that is used for digital image processing (DIP), and ultimately to calculate the partition coefficient of the samples imaged. The entire program consists conceptually of the following functions,

1. `main.xml`:
   This handles iterating through the experimental data sets and the relevant file calls. Seen in Section D.1.

2. `processFiles` function:
   This handles the current file name and the file calls for all relevant files. Seen in Section D.2.

3. `getImageData` function:
   This imports the actual images (.png) into a single image array. Seen in Section D.3.

4. `viewMask` function:
   Enables the user to manually check (and correct) the regions of interest (ROIs) settings for the specific experimental set images. Seen in Section D.4.

5. `processData` function:
   Calculates the partition coefficient of the samples in the images of the specific experimental data set. Seen in Section D.5.

6. `settings` function:
   A pseudo-function as a placeholder for `settings_[X]MHz[_subset]` functions that hold the ROIs pixel locations. Seen in Section D.6.

7. `writeRawData` function:
   Writes the pixel statistical data of a particular image to a .txt file. Seen in Section D.7.

8. `writeData` function:
   Writes the partition coefficient statistical information for an experimental set to a .txt file. Seen in Section D.8.

The core function of importance is the `processData` which actually calculates the partition coefficients of the given images of a particular experimental data set. The `processData` is detailed in Section D.5. Another core function is the `settings` function. This isn't a specific function as such but rather a pseudo-function as a placeholder for a collection of MATLAB (.m) files that provide the image settings and image ROIs pixel locations for each experimental set.

The details of the functions are provided in each of the associated sections below.

D.1 The `main` function

The main function handles the overall conceptual data set calls and iterations, and their options. Additionally, it handles the calls to functions that save the raw image sample pixel data and the partitioning coefficients mean and standard deviation of the experimental set. The code is described below.

D.1.1 The initialisation

The first part of the main function code is see in Source-code D.1.
Here, the `[show]=showPrompt();` is a simple command window prompt that requests if the user would like to be shown the ROIs over the images. This makes the `processFiles.m` function call the `viewMask.m` function which enables the user to see, and subsequently, adjust and update the ROI settings in the relevant settings file. This is detailed further in Section D.2 and Section D.4.

Further in Source-code D.1, the `Subset = ["","Preview","Afterview"]` simply provides the key-words used to identify the image files according to the 2.5 min, 5 min and 7.5 min imaging times, explained in the experimental process (as described in Chapter 3).

Next are some explicit folder declarations from lines 6 to 18 and the declaration of the image file extension as portable network graphics (png) in line 20.

The number of clear reference samples and null reference samples in each image are specified, one each, in lines 22 and 23.

Finally in Source-code D.1, an empty array of mean partition coefficients for the entire experimental control region is predefined, `LgP = zeros(10,15,3)` in line 25. The structure of this array is 10-rows for each control frequency 1 MHz to 10 MHz in 1 MHz intervals; by 15-columns, which is the control amplitudes, 0 kPa to 100 kPa in intervals of 10 kPa, plus the extended pressures for selected frequencies; by 3-layers, which corresponds to the experimental sets described by `Subset = ["","Preview","Afterview"]` corresponding to the images taken at 5 min, 2.5 min and 7.5 min respectively.

Source-code D.1: `main.m` options initialising

```
1  [show]=showPrompt();
2  clc
3
4  Subset = ["","Preview","Afterview"];
5
6  rootPath = 'Drive:\the_root_path';
7  cd(rootPath);
8
9  dataFolder = strcat(rootPath,'\Data\');
10 rawDataFolder = strcat(rootPath,'\rawData\');
11 settingsPath = strcat(rootPath,'\Settings\');
12
13 if ~exist(dataFolder, 'dir')
14    mkdir(dataFolder)
15 end
16 if ~exist(rawDataFolder, 'dir')
17    mkdir(rawDataFolder)
18 end
19
20 fileExt = '.png';
21
22 clearSamples = 1;
23 refSamples = 1;
24
25 LgP = zeros(10,15,3);
```

D.1.2 The subset iteration

The next part of the main function handles the iteration through each subset as seen in Source-code D.2. The first part sets some further subset-specific initialisation "options". Firstly, `subset = Subset(set)` specifically selects the explicit keyword for the filenames of the experimental subset. Following this is the `Data` and `rawData` empty array initialisation.

`Data=zeros(10,15,10)` is of similar structure to `LgP` above, except the three-dimensional

(3D) layers are associated with the images of the specific experimental subset. It stores the calculated partition coefficient of each possible image (standard and extended pressure ranges) in this array, which is later used to determine the mean and standard deviation of the experimental set.

`rawData=zeros(10,12,10,4)` is also of similar structure. However, the two-dimensional (2D) columns are associated with the (maximum) number of samples in the image, the clear reference, null experiment, and then the ten (or six) other acoustically exposed samples. The fourth dimension (4D) stores the sample's pixel statistics, namely, the octanol phase mean pixel value, the octanol phase pixel value standard deviation, the water phase mean pixel value, and the water phase pixel value standard deviation. Therefore the array consists of the dimension [frequency]x[image samples]x[image number]x[sample's pixel statistics].

The next step iterates through each frequency (which, for convenience of explanation, is contracted here). This is detailed later within Subsection D.1.3 with the associated code in Source-code D.3 and Source-code D.4. The important concept here is that it handles the frequency iteration for each experimental image as a nested loop, and retrieves the actual image data for the `Data` and `rawData` arrays.

After the nested frequency iteration, the statistical information from the `Data` array is calculated with the local function `MeanStd`. This simply calculates the mean and standard deviation of the experimental data stored in the `Data` array. It implements MATLAB standard functions; however, it is adapted to handle the possibility of "missing image" zero data.

The mean is calculated directly from the number of non-zero elements along the required dimension, as seen in line 27 of Source-code D.2. The number of non-zero elements are found with `sum(M~=0,dim)`. Here, `M~=0` returns a logical matrix with a one in the positions that are non-zero, and zero otherwise. This is then summed along the required dimension, essentially forming a matrix of reduced dimensions, compressed along dimension `dim` with entries that are the number of non-zero elements along the dimension `dim`. `sum(M, dim)` sums the elements of `M` along the dimension `dim`, and the element-wise division with the number of non-zero elements `sum(M~=0,dim)` returns the

mean value of the matrix `M` along the dimension `dim`.

`std_M = nanstd(M,mode,dim)` in line 30 calculates the standard deviation of the `M` array, which has had its zeros replaced with `nan` in line 29. The MATLAB function `nanstd()` calculates the standard deviation of the input matrix, along the specified dimension, while excluding nan entries from the calculation. This prevents the zero entries from skewing the standard deviation calculation.

Going back to the main part of the `main` function in Source-code D.2, the remaining lines simply save the `Data` and `rawData` to the necessary files using the correspondingly named functions. Lastly, on line 23, the mean partition coefficients of the subset is saved to the `LgP` array.

Source-code D.2: `main.m` subset iteration

```
for set = 1:length(Subset)
    subset = Subset(set)

    Data = zeros(10,15,10);

    rawData = zeros(10,12,10,4);

    for freq = 1:10
    end
    [LgP_mean, LgP_std, LgP_stdPercent] = MeanStd(Data,3,1);

    currentFolder = pwd;
    cd(rawDataFolder);
    writeRawData(subset, rawData);
    cd(currentFolder);

    Data(Data==0) = nan;
    currentFolder = pwd;
    cd(dataFolder);
    writeData(subset, Data, LgP_mean, LgP_std, LgP_stdPercent);
    cd(currentFolder);

    LgP(:,:,set) = LgP_mean;
end

function [mean_M, std_M, std_Percent_M] = MeanStd(M,dim,mode)
    mean_M = sum(M, dim)./sum(M~=0,dim);

    M(M==0) = nan;
    std_M = nanstd(M,mode,dim);

    std_Percent_M = (std_M./mean_M).*100;
end
```

D.1.3 The frequency iteration

The frequency iteration is nested within the subset loop, and primarily handles the file call to the necessary `processFiles` function. The frequency iteration is conceptually divided into the standard pressure file call, as seen in Source-code D.3, and the extended pressure file call through conditional if statement checks, as seen in Source-code D.4.

Firstly for the standard pressure range, in Source-code D.3, the `settings` file name is specified on lines 3 to 6. Following this is the specification of the image axis limits for if the `show` option for viewing the ROIs was selected. Next, the number of samples for the standard range is specified, `Samples = 10`, along with the minimum and maximum pressure of the standard range.

Line 17 to 21 of Source-code D.3 is a single function call to `processFiles`, which processes the image files as needed. This returns the specific partition coefficient data as required. Finally the data is stored in the `Data` and `rawData` matricies as needed.

Source-code D.3: `main.m` subset nested frequency iteration for standard pressure range

```
1      for freq = 1:10
2
3          settings = strcat('settings_',num2str(freq),'MHz');
4          if (strlength(subset)) ~=0
5              settings = strcat(settings,'_',subset);
6          end
7
8          extended = false;
9          xLim1 = [380 660];
10         xLim2 = [660 940];
11         yLim = [340 450];
12
13         Samples = 10;
14         amplow = 10;
15         amphigh = 100;
16
17         [lgP,oct_pix_val,wat_pix_val,NumImages] = processFiles(...
18             rootPath, settingsPath, fileExt,...
19             settings, subset, freq, extended,...
20             amplow, amphigh, Samples, clearSamples, refSamples,...
21             show, xLim1, xLim2, yLim);
22         Data(freq,1:11,1:NumImages) = lgP;
23         rawData(freq,1:12,1:NumImages,:) = cat(3,oct_pix_val,wat_pix_val);
```

For the extended pressures for selected frequencies, the settings file is appended, the image axis limits and the number of samples are changed accordingly. This is seen in lines 1 to 7 of Source-code D.4. Following this is a conditional if statement check for each of the frequencies that have extended pressure range experiments. In each condition, the upper amplitude is changed, and the same `processFiles` function is called. The local function `getExtended` is called to handle the correct assignment of the resultant partition coefficient data into the `Data` and `rawData` arrays. (Note, for the `elseif` cases, the function calls of `processFiles` and `getExtended` are omitted for easier code viewing. They are the same as the initial if statement)

Source-code D.4: `main.m` subset nested frequency iteration fore frequency specific extended pressure ranges

```
1           extended = true;
2           settings = strcat(settings,'_extended');
3           xLim1 = [480 675];
4           xLim2 = [675 870];
5           yLim = [340 450];
6
7           Samples = 6;
8
9           if (freq == 5)
10              amphigh = 400;
11
12              [lgP,oct_pix_val,wat_pix_val,NumImages] = processFiles(...
13                  rootPath, settingsPath, fileExt,...
14                  settings, subset, freq, extended,...
15                  amplow, amphigh, Samples, clearSamples, refSamples,...
16                  show, xLim1, xLim2, yLim);
17              [Data,rawData] = getExtended(Data,rawData,...
18                  freq,lgP,oct_pix_val,wat_pix_val,NumImages);
19
20          elseif (freq == 6) || (freq == 10)
21              amphigh = 500;
22          elseif (freq == 7) || (freq == 8) || (freq == 9)
23              amphigh = 800;
24          end
25      end
26
27  function [Data,rawData] = getExtended(Data,rawData, ...
28      freq,lgP,oct_pix_val,wat_pix_val,NumImages)
29
30      Data(freq,[1,2,11],(5+1):(5+NumImages)) = lgP(1:3,:);
31      Data(freq,[12:end],(5+1):(5+NumImages)) = lgP(4:end,:);
32
33      rawData(freq,1:8,(5+1):(5+NumImages),:) = cat(3, ...
34          oct_pix_val(1:end,:,:), wat_pix_val(1:end,:,:));
35  end
```

D.1.4 viewing the results

The remaining code of the `main.m` file simply graphs the results as a surface. Details of this are trivial. The complete and uncontracted code can be seen in Section D.9.

D.2 The `processFiles` function

The `processFiles` function handles the main image file interactions. The code is provided in Source-code D.5. Firstly, the total number of samples and the required root filenames of the images are set. Following this is the fetching of the experimental set images' settings and the generation of the image array for DIP. This is done with the local function `getROISettigns` which is further seen in Source-code D.6.

Conceptually, the `getROISettings` function goes to the settings file path, and calls the "`Settings`" function, which is a generic variable name for the actual filename function from line 8, `Settings = str2func(settings)`. The settings file's generic structure is detailed in Section D.6. Then the `getROISettings` function calls the `getImageData` function which returns the `Im` array containing all the relevant experimental images and, for convenience, the image row and column size. The `getImageData` function is further detailed in Section D.3.

Continuing with the `processFiles` function in Source-code D.5, the conditional if statement simply checks if the `show` variable is set from the `main` function. It calls the `viewMask` function which overlays the ROIs on the images and prompts the user to continue or implicitly allows the user to directly change the ROI file settings and review the updated ROIs.

Finally, the `processFiles` function calls the `processData` function, which actually processes the images of the experimental data set and calculates the partition coefficients of the samples in the image. The `processData` function is further detailed in Section D.5.

The full code of `processFiles` can be seen in Section D.9.

Source-code D.5: `processFiles.m` function for image file handeling

```
function [lgP,oct_pix_val,wat_pix_val,NumImages] = processFiles(...
    rootPath, settingsPath, fileExt,...
    settings, subset, freq, extended,...
    amplow, amphigh, Samples, clearSamples, refSamples,...
    show, xLim1, xLim2, yLim)

    numSamples = Samples + clearSamples + refSamples;
    rootName = strcat('TatooInk',subset, ...
        '~Amp(',num2str(amplow),'-', ...
        num2str(amphigh),'_kPa)', ...
        '~Freq(',num2str(freq),'_MHz)', ...
        '~ExpTime(5_min)');

    if show
        done = false;
        prompt = "Continue? [y]\n";
        while ~done
            [NumImages, r0, c0, rn, cn, row_Adj, col_Adj, ...
                Im, Rows_Im, Cols_Im] = getROISettings( ...
                    rootPath,settingsPath, ...
                    settings,numSamples,rootName,fileExt);
            viewMask(subset, freq, extended, ...
                NumImages, numSamples, Im, ...
                r0, c0, rn, cn, row_Adj, col_Adj, ...
                xLim1, xLim2, yLim);
            txt = input(prompt,"s");
            done = strcmpi(txt,'y');
        end
    end
    [NumImages, r0, c0, rn, cn, row_Adj, col_Adj,...
        Im, Rows_Im, Cols_Im] = getROISettings(...
        rootPath,settingsPath,...
        settings,numSamples,rootName,fileExt);
    [lgP,oct_pix_val,wat_pix_val] = processData(...
        NumImages, numSamples, Im, Rows_Im, Cols_Im,...
        r0, c0, rn, cn, row_Adj, col_Adj);
end
```

Source-code D.6: `processFiles.m` local function for direct settings call and image array generation from experimental images

```
% Local function
function [NumImages, r0, c0, rn, cn, row_Adj, col_Adj,...
    Im, Rows_Im, Cols_Im] = getROISettings(...
    rootPath,settingsPath,...
    settings,numSamples,rootName,fileExt)

    cd(settingsPath);
    Settings = str2func(settings);
    [NumImages, r0, c0, rn, cn, row_Adj, col_Adj] = Settings(numSamples);
    cd(rootPath);

    [Im,Rows_Im,Cols_Im] = getImageData(NumImages,rootName,fileExt);
end
```

Source-code D.7: The `getImageData` function for importing the images of an experimental set

```
function [Im,Rows_Im,Cols_Im] = getImageData(NumImages,rootName,fileExt)
    currentFolder = pwd;
    path = strcat(rootName,'\ExperimentalImages\');
    cd(path)

    fileName = strcat(rootName,'~OriginalImage~dataset');
    activeImage = imread(strcat(fileName,'1',fileExt));
    [Rows_Im,Cols_Im,pix] = size(activeImage);

    Im = uint8(zeros([Rows_Im,Cols_Im,pix,NumImages]));
    Im(:,:,:,1) = activeImage;
    n=2;
    while n < NumImages+1

        activeImage = imread(strcat(fileName,num2str(n),fileExt));
        Im(:,:,:,n) = activeImage;
        n = n+1;
    end

    cd(currentFolder);
end
```

D.3 The `getImageData` function

The `getImageData` function is tasked with navigating to the correct directory for the experimental images for the particular set, and then importing the images into an `Im` array. The `Im` array is four-dimensional (4D), the rows and columns are the image rows and image columns, the third dimension is the actual red-green-blue (RGB) pixel layers' values of the image. This is embedded into the fourth dimension, the image number, for each experimental image. The function can be seen in Source-code D.7, and in Section D.9.

D.4 The `viewMask` function

The `viewMask` function simply enables the user to view the image ROIs before the ROIs are used to calculate the partition coefficients. The code can be seen in Source-code D.8.

The code prints out which experimental data set images are actively being shown with lines 6 to 8. Next, the ROI size is defined as an offset from the centre pixels of the ROIs. The code then iterates through each image. The samples are defined as an index offset, relative to the first and last row, and first and last column, as `row_Select` and `col_Select` respectively. `row_Select` indexes the row of the sample to either the octanol or water phase. `col_Select` indexes the column (beginning at the clear reference) and is calculated from the difference of the beginning end columns positions divided by 11 (for the 11 spaces between the 12 samples).

The code then iterates through the sample indexes, and the row (phase) index, handling one ROI at a time. The code marks the edge of the ROI in the image. Line(s) 19 (to 21) defines the top edge of the ROI, line(s) 21 (to 24) defines the right edge, line(s) 25 (to 27) the bottom edge, and line(s) 28 (to 30) the left edge of the ROI.

The function then displays the resultant image with the overlaid ROI-boundaries in two parts (divided equally) for easier viewing. (note, the actual code to display the images has been contracted). The full code can be seen in Section D.9.

Source-code D.8: The `viewMask` function for viewing the rois on the images.

```
function [] = viewMask(subset, freq, extended, ...
    NumImages, numSamples, Im, ...
    r0, c0, rn, cn, row_Adj, col_Adj, ...
    xLim1, xLim2, yLim)

    fprintf(strcat('Subset=',subset, ...
        ' : Frequency=',num2str(freq), ...
        ' : extended=',num2str(extended),'\n\n'))
    dr= 12;
    dc = 7;
    for N = 1:NumImages
        msg = strcat('Image ',num2str(N))

        row_Select = (rn(N)-r0(N))
        col_Select = ceil((cn(N)-c0(N))/(numSamples-1))

        im(:,:,:) = Im(:,:,:,N);
        for i = (1:numSamples)-1
            for j = 0:1
                im(r0(N)-dr + j*row_Select + row_Adj(j+1,i+1,N), ...
                    c0(N)+(-dc:dc) + i*col_Select + col_Adj(N,(i+1)), ...
                    :) = 255;
                im(r0(N)+(-dr:dr) + j*row_Select + row_Adj(j+1,i+1,N), ...
                    c0(N)+dc + i*col_Select + col_Adj(N,(i+1)), ...
                    :) = 255;
                im(r0(N)+dr + j*row_Select + row_Adj(j+1,i+1,N), ...
                    c0(N)+(-dc:dc) + i*col_Select + col_Adj(N,(i+1)), ...
                    :) = 255;
                im(r0(N)+(-dr:dr) + j*row_Select + row_Adj(j+1,i+1,N), ...
                    c0(N)-dc + i*col_Select + col_Adj(N,(i+1)), ...
                    :) = 255;
            end

        fig1 = figure();
        ylim(ax2,yLim)
    end
```

D.5 The `processData` function

This is the core function for the DIP and calculating the resultant partition coefficient of the samples in the experimental set images. The function is declared below in Source-code D.9. Since this is the core function, more detail is provided about this function, its variables and how it operates. The full code can be seen in Section D.9.

D.5.1 The function call

The function call as seen in Source-code D.9 has a number of input variables. These variables are split into two groups. The image level properties and the image sample settings.

Source-code D.9: `processData` function call

```
1 function [lgP,oct_pix_val,wat_pix_val] = processData(...
2     NumImages, numSamples, Im, Rows_Im, Cols_Im,...
3     r0, c0, rn, cn, row_Adj, col_Adj)
```

The inputs on line 2 are image-level settings and properties. `NumImages` is the number of images for the particular experimental set being handled and has a typical value of 5. Similarly, `numSamples` is the total number of samples (the clear reference, null experiment and the actively exposed samples) which are specified for the experimental set. This is either 12 in total (1 clear, 1 null, and 10 actively exposed samples) for the standard pressure range experiments, or 8 (1 clear, 1 null, and 6 actively exposed samples) for the extended pressure range experiments for selected frequencies. The `Im` input is the image array that is generated by `getImageData` as seen in Section D.3, along with the image size properties, `Rows_Im` which is the number of rows in the image and is typically 1080, and `Cols_Im` which is the number of columns in the image and is typically 720.

The next line 3 of the function call is settings associated with the samples in the images themselves. `r0` defines the row of the centre pixel of the first sample's octanol phase

(which is the clear reference's octanol phase centre). `c0` similarly defines the column of the centre pixel of the first sample's octanol phase. This defines the "origin" pixel of the sample indexing that is used. Similarly, `rn` and `cn` define the row and column centre pixel of the last sample's water phase. The `row_Adj` and `col_Adj` provide offset and position correction of the ROI centres that may be present from the auto-generated ROIs. These input variables are defined by the settings file associated with the experimental set. This is further detailed in Section D.6.

The functionality of the `processData` function is further explored below.

D.5.2 The image mask generation

The images are masked with a logical array that is zero (false) everywhere except where the ROIs are defined (as true). This is later multiplied with the image to actually extract the ROIs from the image. The code snippet of the mask generation is seen in Source-code D.10. The code is conceptually similar to that of the `viewMask` function in Section D.4, since there it simply overlays the mask boundary on the images, whereas here, the mask is actually generated as an array.

The values `dr` and `dc` define the ROI size, as an offset from the centre pixels' to the edges of the ROIs. The `total_roi_pixels` size is defined and is explicitly $(2\texttt{dr} + 1)$-by-$(2\texttt{dc} + 1)$ which is $25 \times 15 = 375$ pixels. The mask is defined and preset to false. Next, the mask ROIs for each sample and each corresponding phase are set. This is handled by indexing through the number of samples and phases as defined in lines 8 and 9 with their corresponding for loops. This is iterated for each image.

Source-code D.10: `processData` function mask generation

```
dr = 12;
dc = 7;
total_roi_pixels = (2*dr+1)*(2*dc+1);

mask = false([Rows_Im,Cols_Im,NumImages]);

for N = 1:NumImages
    row_Select = (rn(N)-r0(N));
    col_Select = ceil((cn(N)-c0(N))/(numSamples-1));

    for i = (1:numSamples)-1
        for j = 0:1
        mask(r0(N) + j*row_Select + row_Adj(j+1,i+1,N) + (-dr:dr),...
            c0(N) + i*col_Select + col_Adj(N,(i+1)) + (-dc:dc),N) = true;
        end
    end
end
```

D.5.3 Roi pixel extraction, pixel statistics and partition coefficient calculation

The partition coefficient calculation occurs in the remaining part of the `processData` function, which can be seen in Source-code D.11. Firstly, there is an initialisation of empty arrays for the samples' octanol phase pixel values (`oct_pix_val`), the samples' water phase pixel values (`wat_pix_val`), and the partition coefficients of the samples in the image (`lgP`). The phase pixel value arrays each have the following dimension; the total number of samples, by the number of images, by two for the mean and standard deviation of the phases' ROI pixel values. The `lgP` array has one less "sample" size because the value of the clear reference is omitted (this is justified by the methodology of colourimetry being unable to work for a pure miscible and relatively optically transparent substance here. It is also only present for calibration purposes, not actual measurement).

Next, the active image being processed is converted to a separate grey-scale image which is further processed. The mask generated earlier in Source-code D.10 identifies all the ROIs. However, the logical mask array cannot distinguish between the individual samples nor the octanol and water phases within the sample, as a pure logical matrix.

The active sample region of interest is found using the code in lines 7 and 10 of Source-code D.11. Firstly, the relevant logical mask array is converted to a labelled image using the MATLAB function `bwlabel` in line 7. This generates a labelled matrix where all the 8-connected "ones/trues" are reassigned to a specific connected value. If there are n distinct connected object regions in an array, then each connected object-regions will have a value between 1 and n assigned, with labelling priority given top-down, then left-right, for the numerical value assigned. Conceptually this results in the octanol ROIs being assigned odd numbers from left to right, and the water ROIs below them being assigned even numbers from left to right. This is then used to conveniently index each sample and the phases of the sample.

The `for n=1:numSamples` loop on line 8 iterates through the number of samples in the image. The sample's octanol and water regions are identified with an odd-even pair mapping of the current sample number `n` in a nested loop, i.e. `for p = 2*n+(-1:0)` on line 9. From here, the calculations and statistics used for the ROI are the same regardless

of the active phase ROI. The assignment of the value to the correct variable is simply done using a conditional if statement later in the code.

To extract the ROI pixel values, the `bw_roi_mask` is multiplied with the grey-scale image. This generates an image the same size as the original but is zero everywhere except in the ROI (but not exclusively, as any pixels in the ROI could be zero). The non-zero pixels are then extracted from the resultant ROI masked image using the MATLAB function `nonzeros()` in line 12. To calculate the mean pixel value `mu_pix`, the non-zero pixels are summed together and divided by the total number of pixels in the ROI. This is seen in lines 14 and 15.

To calculate the standard deviation, the non-zero pixels need to be padded with zeros if the region actually had zeros in it that were removed by the `nonzeros()` function. This is done by comparing the length of the non-zero pixels `nz_pix` with the total number of pixels (expected to be) in the ROI, and `nz_pix` is padded as needed to give `pix`. This is seen in line 16 of Source-code D.11. Finally the standard deviation `std_pix` is calculated on the `pix` using the MATLAB function `std()` on line 17.

The conditional if statement `if mod(p,2)` on line 21 of Source-code D.11 checks if the current ROI encoding is even or odd. If p is odd, then mod(p,2) returns 1, and the mean and standard deviation values are assigned to the octanol array `oct_pix_val`. Else, p is even, mod(p,2) returns 0, and the values are assigned to the water array `wat_pix_val`.

The conditional statement on line 29 checks if the sample count is larger than 1 (i.e. not the clear reference sample) and then actually calculates the partition value.

The concentration within the phase is calculated with the natural logarithm of the ratio of the pixel intensity of the clear reference phase to the pixel intensity of the sample Phase. This is done for both octanol and water phases on lines 30 and 31. The partition coefficient is then calculated as the base 10 logarithm of the ratio of the octanol phase concentration to that of the water phase concentration on line 32.

The full `processData` code can be seen in Section D.9.

Minimum value check

There is a minimum value check for the mean pixel value seen on lines 18 to 20. This simply ensures that if the mean pixel value calculated is zero, then this is corrected to the minimum usable non-zero value of the measurement system. This minimum is a pixel value of 1 (with the other pixels zero) in the ROI, divided by 375, the total number of pixels. This prevents possible issues with division by zero and log of zero issues that could occur with the rest of the partition coefficient calculation. This is expected to happen mostly in the octanol phase due to the microparticles being hydrophobic. It is also expected to have minimal impact on the calculation since the partition coefficient will then be dominated by the water phase mean pixel value.

Source-code D.11: `processData` function roi pixel extraction and partition coefficient calculation

```
oct_pix_val = zeros(numSamples,NumImages,2);
wat_pix_val = zeros(numSamples,NumImages,2);
lgP = zeros(numSamples-1,NumImages);

for N = 1:NumImages
    greyIm = rgb2gray(Im(:,:,:,N));
    labelIm = bwlabel(mask(:,:,N));
    for n=1:numSamples
        for p = 2*n+(-1:0)
            bw_roi_mask = uint8((labelIm)==p);
            roi_pixels = greyIm.*bw_roi_mask;
            nz_pix = nonzeros(roi_pixels);

            sum_pix = sum(nz_pix);
            mu_pix = sum_pix/total_roi_pixels;
            pix = [nz_pix; zeros((total_roi_pixels-length(nz_pix)),1)];
            std_pix = std(double(pix));
            if mu_pix < (1/375)
                mu_pix = (1/375);
            end
            if mod(p,2)
                oct_pix_val(n,N,1) = mu_pix;
                oct_pix_val(n,N,2) = std_pix;
            else
                wat_pix_val(n,N,1) = mu_pix;
                wat_pix_val(n,N,2) = std_pix;
            end
        end
        if n>1
            o_conc = log( (oct_pix_val(1,N,1))./(oct_pix_val(n,N,1)) );
            w_conc = log( (wat_pix_val(1,N,1))./(wat_pix_val(n,N,1)) );
            lgP(n-1,N) = log10(o_conc/w_conc);
        end
    end
end
end
```

D.6 The `settings` functions

The settings files have a structure that can be seen in Source-code D.12. The files are named according to the following convention `settings_[X]MHz[_subset]`, where `[X]` is the frequency of the experimental set, and `[_subset]` indicates the subset. The subset values are: nothing " ", if it is the standard image set taken at 5 min; "Preview", for the image set taken at 2.5 min; and "Afterview", for the image set taken at 7.5 min after the samples are reshaken at 5 min.

The structure of the file is as follows. The number of images that are part of the experimental data set is first declared, and the `row_Adj` and `col_Adj` are predefined empty in the first few lines of code. Then for each image (the start of which is indicated by an explicit comment), the following values are set.

- `r0` : the row number of the first (clear reference) sample's octanol phase ROI centre pixel.
- `c0` : the column number of the first (clear reference) sample's octanol phase ROI centre pixel.
- `rn` : the row number of the last sample's water phase ROI centre pixel.
- `cn` : the column number of the last sample's water phase ROI centre pixel.

This is used to index the location of the other sample phase centre pixel locations automatically. This, however, may be positioned incorrectly due to image projection distortions. The `row_Adj` and `col_Adj` values are used as a correction for this error and is set as needed (in conjunction with the initial run and the `viewMask` function). The `row_Adj` is capable of adjusting each of the rows of the ROIs individually, i.e. each phase of each sample. The `col_Adj` can adjust the column of the samples. The individual phase ROIs doesn't need a specific column correction since the phases are vertically confined and aligned.

These values are repeated as needed for each of the images in the experimental set.

Source-code D.12: Example of the `settings_[X]MHz[_subset]` files

```
function [NumImages, r0, c0, rn, cn, row_Adj, col_Adj] = ...
    settings_[X]MHz[_subset](numSamples)

NumImages = 5;

row_Adj = zeros(2,numSamples,NumImages);
col_Adj = zeros(NumImages,numSamples);

% Image1
n=1;
r0(n) = 50;
c0(n) = 100;
rn(n) = 100;
cn(n) = 1200;

row_Adj(:,:,n) = [   0,0,0,0,0,0,0,0,0,0,0,0; ...
                     0,0,0,0,0,0,0,0,0,0,0,0];

col_Adj(n,:) = [0,0,0,0,0,0,0,0,0,0,0,0];
%%%%%%%%%%%%%%%%%%%%%%%%%

end
```

D.7 The `writeRawData` function

The `writeRawData` function writes the raw pixel value data `oct_pix_val` and `wat_pix_val` contained in the `rawData` array to a file. The file is named corresponding to the experimental data set and related image of that data set. The specific details of this are not necessary for this document, the code is simply presented "as is" in Section D.9.

D.8 The `writeData` function

The `writeData` function writes the partition coefficient statistical information, mean partitian coefficient and standard deviation of the partition coefficient of the experimental set images, to a file. The file is named according to the experimental set. Similarly to the `writeRawData`, specific details of this are not necessary for this document, the code is simply presented "as is" in Section D.9.

D.9 Complete code

`main` function

```
%%%%%%%%% Main function for Digital Image Processing Colourimetry %%%%%%%%%
clear all
clc
%%%%%%%%%%%%%%%%%%%%%%%%%%%%%%%%%%%%%%%%%%%%%%%%%%%%%%%%%%%%%%%%%%%%%%%%%%%

% prompt user: show the
[show]=showPrompt();
clc

%define the subsets of the files
Subset = ["","Preview","Afterview"];

rootPath = 'Drive:\the_root_path';
cd(rootPath);

% Relative folder paths
dataFolder = strcat(rootPath,'\Data\');% for colourimetry partition data
rawDataFolder = strcat(rootPath,'\rawData\');% for raw image pixel data
settingsPath = strcat(rootPath,'\Settings\');% for image processing setting

% Check if data and rawData folders exist, creat if necessary
if ~exist(dataFolder, 'dir')
   mkdir(dataFolder)
end
if ~exist(rawDataFolder, 'dir')
   mkdir(rawDataFolder)
end

% The image file extension
fileExt = '.png';

% The number of clear sample and "null" reference samples in the images
clearSamples = 1;
refSamples = 1;

```

```
% predefined partition matrix for all the data
LgP = zeros(10,15,3);
%([frequencies],[image experimental samples + extended],...
% [mean+std+std%])

for set = 1:length(Subset)
    subset = Subset(set)% the current subset

    % The Data matrix for the current set
    Data = zeros(10,15,10);
    %([frequencies],[image experimental samples + extended],...
    % [num images+extended amplitude images])

    % The rawData matrix for the current set
    rawData = zeros(10,12,10,4);
    %([frequencies],[all image samples],...
    % [num images+extended amplitude images],[phases:mean+std])

    for freq = 1:10

        % define the settings file name
        settings = strcat('settings_',num2str(freq),'MHz');
        if (strlength(subset)) ~=0
            settings = strcat(settings,'_',subset);
        end

        %%%%%%%%%%%%%%%%%%%%
        % standard pressure range with relevant settings
        extended = false;
        % Define image axis limits for viewing
        xLim1 = [380 660];
        xLim2 = [660 940];
        yLim = [340 450];

        % Number of samples for the std pressure range
        Samples = 10;
        amplow = 10;
        amphigh = 100;

        % Process files, assign the Data and rawData matricies as needed
        [lgP,oct_pix_val,wat_pix_val,NumImages] = processFiles(...
```

```
77              rootPath, settingsPath, fileExt,...
78              settings, subset, freq, extended,...
79              amplow, amphigh, Samples, clearSamples, refSamples,...
80              show, xLim1, xLim2, yLim);
81          Data(freq,1:11,1:NumImages) = lgP;
82          rawData(freq,1:12,1:NumImages,:) = cat(3,oct_pix_val,wat_pix_val);
83
84          %%%%%%%%%%%%%%%%%%%
85          % extended pressure range with relevant settings
86          extended = true;
87          % append the settings file name
88          settings = strcat(settings,'_extended');
89          % define image axis limits for viewing
90          xLim1 = [480 675];
91          xLim2 = [675 870];
92          yLim = [340 450];
93
94          %the number of samples for the extended range
95          Samples = 6;
96
97          % Process files, assign the Data and rawData matricies as needed
98              % for the extended ranges
99          if (freq == 5)
100             amphigh = 400;
101
102             [lgP,oct_pix_val,wat_pix_val,NumImages] = processFiles(...
103                 rootPath, settingsPath, fileExt,...
104                 settings, subset, freq, extended,...
105                 amplow, amphigh, Samples, clearSamples, refSamples,...
106                 show, xLim1, xLim2, yLim);
107             [Data,rawData] = getExtended(Data,rawData,...
108                 freq,lgP,oct_pix_val,wat_pix_val,NumImages);
109
110         elseif (freq == 6) || (freq == 10)
111             amphigh = 500;
112
113             [lgP,oct_pix_val,wat_pix_val,NumImages] = processFiles(...
114                 rootPath, settingsPath, fileExt,...
115                 settings, subset, freq, extended,...
116                 amplow, amphigh, Samples, clearSamples, refSamples,...
117                 show, xLim1, xLim2, yLim);
```

```
118             [Data,rawData] = getExtended(Data,rawData,...
119                 freq,lgP,oct_pix_val,wat_pix_val,NumImages);
120 
121         elseif (freq == 7) || (freq == 8) || (freq == 9)
122             amphigh = 800;
123 
124             [lgP,oct_pix_val,wat_pix_val,NumImages] = processFiles(...
125                 rootPath, settingsPath, fileExt,...
126                 settings, subset, freq, extended,...
127                 amplow, amphigh, Samples, clearSamples, refSamples,...
128                 show, xLim1, xLim2, yLim);
129             [Data,rawData] = getExtended(Data,rawData,...
130                 freq,lgP,oct_pix_val,wat_pix_val,NumImages);
131 
132         end
133     end
134     %Calculate the statistical information from the Data
135     [LgP_mean, LgP_std, LgP_stdPercent] = MeanStd(Data,3,1);
136 
137     % Save the raw data in rawData to relevant .txt files
138     currentFolder = pwd;
139     cd(rawDataFolder);
140     writeRawData(subset, rawData);
141     cd(currentFolder);
142 
143     % Save the data in Data to relevant .txt files
144     Data(Data==0) = nan;
145     currentFolder = pwd;
146     cd(dataFolder);
147     writeData(subset, Data, LgP_mean, LgP_std, LgP_stdPercent);
148     cd(currentFolder);
149 
150     % Save the set statistical measurements to the partition matrix
151     LgP(:,:,set) = LgP_mean;
152 end
153 clear Subset subset set ...
154     rootPath dataFolder rawDataFolder settingsPath fileExt ...
155     Data rawData clearSamples refSamples ...
156     show xLim1 xLim2 yLim ...
157     freq settings extended Samples NumImages amplow amphigh...
158     lgP oct_pix_val wat_pix_val;
```

```
159
160 % Plot the partition vlaue surfaces for each subset
161 one= ones(1,15);
162 One = ones(10,1);
163
164 X = One*[0:10:100,200:100:500];
165 X(5,13:15) = [250,300,400];
166 X(7,13:15) = [400,600,800];
167 X(8,13:15) = [400,600,800];
168 X(9,13:15) = [400,600,800];
169
170 Y = [1:10]'*one;
171
172 clear One one
173
174 figure;
175 surf(X,Y,LgP(:,:,1))
176 view (10,50)
177 set(gca, 'XScale', 'log')
178 xlabel("Acoustic amplitude (kPa)")
179 ylabel("Acoustic frequency (MHz)")
180 zlabel("Partition coefficent (log[P])")
181 axis([10 1000 0 10 0 0.35])
182
183 figure;
184 surf(X,Y,LgP(:,:,2))
185 view (10,50)
186 set(gca, 'XScale', 'log')
187 xlabel("Acoustic amplitude (kPa)")
188 ylabel("Acoustic frequency (MHz)")
189 zlabel("Partition coefficent (log[P])")
190 axis([10 1000 0 10 0 0.35])
191
192 figure;
193 surf(X,Y,LgP(:,:,3))
194 view (10,50)
195 set(gca, 'XScale', 'log')
196 xlabel("Acoustic amplitude (kPa)")
197 ylabel("Acoustic frequency (MHz)")
198 zlabel("Partition coefficent (log[P])")
199 axis([10 1000 0 10 0 0.35])
```

```
%%%%%%%%%%%%%%%%%%%%%%%%%%%%%%%%%%%%%%%%%%%%%%%%%%%%%%%%%%%%%%%%%%%%%%%%%%%%

% local functions
function [show] = showPrompt()
    %simple function to prompt user if the roi image overlays should show

    done = false;
    prompt = "Show image rois? [y/n]\n";

    % Initial prompt
    txt = input(prompt,"s");

    while ~done % only valid input allowed
        if strcmpi(txt,'y')&&~strcmpi(txt,'n')
            show = true;
            return; % end function on successful option
        elseif ~strcmpi(txt,'y')&&strcmpi(txt,'n')
            show = false;
            return; % end function on successful option
        else
            % Re-prompt on invalid txt
            txt = input(strcat("Incorrect input. ",prompt),"s");
        end
    end
end

function [mean_M, std_M, std_Percent_M] = MeanStd(M,dim,mode)
    % find the mean of the matrix along "dim"
    mean_M = sum(M, dim)./sum(M~=0,dim);

    % replace the entries = 0 with nan
    M(M==0) = nan;
    % find the std deviation of the elements (excluding nan's) along "dim"
    std_M = nanstd(M,mode,dim);

    % find the std as a percentage error of the mean value
    std_Percent_M = (std_M./mean_M).*100;
end
%%%%%%%%%%%%%%%%%%%%%%%%%%%%%%%%%%% END %%%%%%%%%%%%%%%%%%%%%%%%%%%%%%%%%%%
```

processFiles function

```
function [lgP,oct_pix_val,wat_pix_val,NumImages] = processFiles(...
    rootPath, settingsPath, fileExt,...
    settings, subset, freq, extended,...
    amplow, amphigh, Samples, clearSamples, refSamples,...
    show, xLim1, xLim2, yLim)
% Processes and handles high level interactions for the relevant file(s)
% filenames, fore the given experimental set itteration.
% Calls the relevant function to calculate and then returns the
% partition value data.
    %%
    %total number of samples in image
    numSamples = Samples + clearSamples + refSamples;

    % build the root filename
    rootName = strcat('TatooInk',subset, ... % the relavant file subset
        '~Amp(',num2str(amplow),'-',... % start amplitude
        num2str(amphigh),'_kPa)',... % end amplitude
        '~Freq(',num2str(freq),'_MHz)',... % frequency
        '~ExpTime(5_min)'); % exposure time (not implemented)

    if show
        done = false;
        prompt = "Continue? [y]\n";
        while ~done
            % get the roi settings for the experimental set images
            [NumImages, r0, c0, rn, cn, row_Adj, col_Adj, ...
                Im, Rows_Im, Cols_Im] = getROISettings( ...
                    rootPath,settingsPath, ...
                    settings,numSamples,rootName,fileExt);

            % view the image roi settings
            viewMask(subset, freq, extended, ...
                NumImages, numSamples, Im, ...
                r0, c0, rn, cn, row_Adj, col_Adj, ...
                xLim1, xLim2, yLim);

            % prompt to continue to next set
                %(or readjust the settings file manually and review)
```

```
39              txt = input(prompt,"s");
40              done = strcmpi(txt,'y'); % anything (except y) reruns
41          end
42      end
43
44      % (re-)get the roi settings for the experimental set images
45      [NumImages, r0, c0, rn, cn, row_Adj, col_Adj,...
46          Im, Rows_Im, Cols_Im] = getROISettings(...
47          rootPath,settingsPath,...
48          settings,numSamples,rootName,fileExt);
49
50      % process the image files to calculate log(P)
51      [lgP,oct_pix_val,wat_pix_val] = processData(...
52          NumImages, numSamples, Im, Rows_Im, Cols_Im,...
53          r0, c0, rn, cn, row_Adj, col_Adj);
54  end
55
56  % Local function
57  function [NumImages, r0, c0, rn, cn, row_Adj, col_Adj,...
58      Im, Rows_Im, Cols_Im] = getROISettings(...
59      rootPath,settingsPath,...
60      settings,numSamples,rootName,fileExt)
61
62      % load the required variable settings for the image dataset
63      cd(settingsPath);
64      Settings = str2func(settings);
65      [NumImages, r0, c0, rn, cn, row_Adj, col_Adj] = Settings(numSamples);
66      cd(rootPath);
67
68      % get the required images for the dataset as per settings
69      [Im,Rows_Im,Cols_Im] = getImageData(NumImages,rootName,fileExt);
70  end
```

getImageData function

```
function [Im,Rows_Im,Cols_Im] = getImageData(NumImages,rootName,fileExt)
% Changes the folder to retrieve the correct image for the dataset being
% processed. Combines the images into a single image matrix for easier code
% handeling.
    %%
    % save the "current folder"
    currentFolder = pwd;
    % go to the folder with images
    path = strcat(rootName,'\ExperimentalImages\');
    cd(path)

    fileName = strcat(rootName,'~OriginalImage~dataset');

    % get the first image from the root filename
    activeImage = imread(strcat(fileName,'1',fileExt));
    [Rows_Im,Cols_Im,pix] = size(activeImage);

    % create an image array to store all images
    Im = uint8(zeros([Rows_Im,Cols_Im,pix,NumImages]));

    % save the image in the image array
    Im(:,:,:,1) = activeImage;

    % load the other images into the image array
    n=2;
    while n < NumImages+1
        % get the nth image from the root filename
        activeImage = imread(strcat(fileName,num2str(n),fileExt));
        Im(:,:,:,n) = activeImage;
        n = n+1;
    end

    % return to "current folder"
    cd(currentFolder);
end
```

viewMask function

```
function [] = viewMask(subset, freq, extended, ...
    NumImages, numSamples, Im, ...
    r0, c0, rn, cn, row_Adj, col_Adj, ...
    xLim1, xLim2, yLim)
% Overlays the dataset images with the rois as specified in the settings
% file. Used for visual confermation of image rois.
    %%
    % tell the user which experimental set images are being viewed
    fprintf(strcat('Subset=',subset, ...
        ' : Frequency=',num2str(freq), ...
        ' : extended=',num2str(extended),'\n\n'))

    % the offset from centre pixels that determines the roi size
    dr= 12;
    dc = 7;
    % roi size explicitly [(2*dr+1)]-by -[(2*dc+1)] = 25x15 = 375 pixels

    for N = 1:NumImages
        %specify the image
        msg = strcat('Image ',num2str(N))

        % find the sample indexes
        Dr = (rn(N)-r0(N))
        Dc = ceil((cn(N)-c0(N))/(numSamples-1))

        % extract the relerant image from the image matrix
        im(:,:,:) = Im(:,:,:,N);
        % overlay the rois of each sample and each phase
        for i = (1:numSamples)-1
            for j = 0:1
                % the top line
                im(r0(N)-dr + j*Dr + row_Adj(j+1,i+1,N), ...
                    c0(N)+(-dc:dc) + i*Dc + col_Adj(N,(i+1)), ...
                    :) = 255;
                % the right side line
                im(r0(N)+(-dr:dr) + j*Dr + row_Adj(j+1,i+1,N), ...
                    c0(N)+dc + i*Dc + col_Adj(N,(i+1)), ...
                    :) = 255;
```

```
39                  % the bottom line
40                  im(r0(N)+dr + j*Dr + row_Adj(j+1,i+1,N), ...
41                      c0(N)+(-dc:dc) + i*Dc + col_Adj(N,(i+1)), ...
42                      :) = 255;
43                  %the left side line
44                  im(r0(N)+(-dr:dr) + j*Dr + row_Adj(j+1,i+1,N), ...
45                      c0(N)-dc + i*Dc + col_Adj(N,(i+1)), ...
46                      :) = 255;
47              end
48          end
49
50          % show the images with the overlayed rois
51              % the image is split into two parts for easier viewing
52          % part 1
53          fig1 = figure();
54          ax1 = axes(fig1);
55          image(ax1,im)
56          xlim(ax1,xLim1)
57          ylim(ax1,yLim)
58          % part 2
59          fig2 = figure;
60          ax2 = axes(fig2);
61          image(ax2,im)
62          xlim(ax2,xLim2)
63          ylim(ax2,yLim)
64      end
65  end
```

processData function

```
function [lgP,oct_pix_val,wat_pix_val] = processData(...
    NumImages, numSamples, Im, Rows_Im, Cols_Im,...
    r0, c0, rn, cn, row_Adj, col_Adj)
% Performs the core digital image processing. Creates the rois and
% calculates the pixel statistical information. Uses the averages to
% calculate the octanol-water partition coefficient.
%%
dr = 12; %roi row centre-to-edge size
dc = 7; %roi col centre-to-edge size
total_roi_pixels = (2*dr+1)*(2*dc+1);

% Predefine mask size
mask = false([Rows_Im,Cols_Im,NumImages]);

%Create masks
for N = 1:NumImages
    row_Select = (rn(N)-r0(N));
    col_Select = ceil((cn(N)-c0(N))/(numSamples-1));

    for i = (1:numSamples)-1
        for j = 0:1
        % set the rois from the settings
        mask(r0(N) + j*row_Select + row_Adj(j+1,i+1,N) + (-dr:dr),...
            c0(N) + i*col_Select + col_Adj(N,(i+1)) + (-dc:dc),N) = true;

        end
    end
end
%%
%predefine octanol and water pixel average and std dev matrix
oct_pix_val = zeros(numSamples,NumImages,2);
wat_pix_val = zeros(numSamples,NumImages,2);
%predefine the log(P) matrix
lgP = zeros(numSamples-1,NumImages);

for N = 1:NumImages %for each image
    %convert the required image to greyscale
    greyIm = rgb2gray(Im(:,:,:,N));
```

```
39
40      for n=1:numSamples %fore each sample (in the image)
41          for p = 2*n+(-1:0) %fore each phase (in the sample, in the image)
42
43              %select the relevant roi
44              bw_roi_mask = uint8((bwlabel(mask(:,:,N)))==p);
45
46              %extract the relevant roi
47              pixels = greyIm.*bw_roi_mask;
48
49              %find the non-zero pixels of the masked image
50              % this returns the pixels in the roi
51              nz_pix = nonzeros(pixels);
52
53              %find the average pixel value in the roi
54              % (explixitly using the total number of roi pixels)
55              sum_pix = sum(nz_pix);
56              mu_pix = sum_pix/total_roi_pixels;
57
58              %pad the extracted nonzeros with zeros if necessary
59              % the total length of the vector must b =total_roi_pixels
60              pix = [nz_pix; zeros((total_roi_pixels-length(nz_pix)),1)];
61              %calculate the std of the pixel values
62              std_pix = std(double(pix));
63              % minimum mean pixel value check
64              if mu_pix < (1/375)
65                  mu_pix = (1/375);
66              end
67              %temporarily store the values according the the roi phase
68              if mod(p,2)
69                  oct_pix_val(n,N,1) = mu_pix;
70                  oct_pix_val(n,N,2) = std_pix;
71              else
72                  wat_pix_val(n,N,1) = mu_pix;
73                  wat_pix_val(n,N,2) = std_pix;
74              end
75
76          end
77
78          %calculate the partition value
79          if (n-1)>0
```

```
80              %calculate the concentration
81              o_conc = log( (oct_pix_val(1,N,1))./(oct_pix_val(n,N,1)) );
82              w_conc = log( (wat_pix_val(1,N,1))./(wat_pix_val(n,N,1)) );
83
84              %the partition value
85              lgP(n-1,N) = log10(o_conc/w_conc);
86          end
87      end
88  end
89
90  end
```

`settings` function(s)

```
function [NumImages, r0, c0, rn, cn, row_Adj, col_Adj] = ...
    settings_[X]MHz[_subset](numSamples)
% The name format is "settings_[frequency]MHz[_set]" for the function call.
% An example of the settings file format with arbitrary example values
%%
%the number of images for the experimental dataset
NumImages = 5;

% predefine the row and column adjusting variables
row_Adj = zeros(2,numSamples,NumImages);
col_Adj = zeros(NumImages,numSamples);

% Image1
n=1; %index number
r0(n) = 50; % the pixle row value of the starting sample row
c0(n) = 100; % the pixle column value of the starting sample column
rn(n) = 100; % the pixle row value of the ending sample row
cn(n) = 1200; % the pixle column value of the ending sample column

% the row adjusting values compensating for each phases' offset error
row_Adj(:,:,n) = [   0,0,0,0,0,0,0,0,0,0,0,0; ... % octanol phase offset
                    0,0,0,0,0,0,0,0,0,0,0,0]; % water phase offset

% the column adjusting values compensating for each phases' offset error
col_Adj(n,:) = [0,0,0,0,0,0,0,0,0,0,0,0];

%%%%%%%%%%%%%%%%%%%%%%%%%
% Image2
% Format repeated as needed for the number of images
end
```

writeRawData function

```
function [] = writeRawData(subset, rawData)
% Writes the raw image pixel statistical information to relavant files.
% Each image has its own unique associated file of pixel information.
    %%
    for freq=1:10
        % create the frequency dataset file name
        name = "RawData";
        if (strlength(subset)) ~= 0
            name = strcat(name,'_',subset);
        end
        name = strcat(name,'_',num2str(freq),'MHz');

        % for each possible image
        for N = 1:5
            % list of the experimental set (constant) frequency
            Freq = ones(1,12).*freq;
            % list of the experimental set (control variable) amplitude
                % include clear reference (as nan)
            amp  = [nan,0:10:100];

            % extract the relevant experimental set image pixel statistics
                % from the rawData matrix
            temp = zeros(12,4);
            temp(:,:) = rawData(freq,:,N,:);
            data = [Freq;amp;temp'];

            % append the file name fore the specific image
            file = strcat(name,'_Im',num2str(N));
            % writeFile local function to write the data of the specific
                % image to the associated file
            writeFile(file,data);

            %%%%%%%%%%%%%%%%%%%%%%%%%
            % for the extended pressure range, create the file name
            file = strcat(file,'_extended');

            temp = zeros(8,4);
            %create the necessary amplitude vector for the data
```

```
39              amp = [nan,0,10,100,nan,nan,nan,nan];
40              if (freq == 5)
41                  % assign the correct extended pressure amplitudes
42                  amp(5:end) = [200,250,300,400];
43                  % extract the relevant data
44                  temp(:,:) = rawData(freq,1:8,(N+5),:);
45                  data = [Freq(1,1:8);amp;temp'];
46                  % writeData local function to write data as needed
47                  writeFile(file,data);
48
49              elseif (freq == 6) || (freq == 10)
50                  % assign the correct extended pressure amplitudes
51                  amphigh = 500;
52                  amp(5:end) = [200:100:amphigh];
53                  % extract the relevant data
54                  temp(:,:) = rawData(freq,1:8,(N+5),:);
55                  data = [Freq(1,1:8);amp;temp'];
56                  % writeData local function to write data as needed
57                  writeFile(file,data);
58
59              elseif (freq == 7) || (freq == 8) || (freq == 9)
60                  % assign the correct extended pressure amplitudes
61                  amphigh = 800;
62                  amp(5:end) = [200:200:amphigh];
63                  % extract the relevant data
64                  temp(:,:) = rawData(freq,1:8,(N+5),:);
65                  data = [Freq(1,1:8);amp;temp'];
66                  % writeData local function to write data as needed
67                  writeFile(file,data);
68
69              end
70          end
71      end
72  end
73  % local function
74  function [] = writeFile(file,data)
75      % create the relevant file for the specific image of the data set
76      fileID = fopen(strcat(file,'.txt'),'w+');
77      % create the file headder
78      fprintf(fileID,'%10s, %10s, %10s, %10s, %10s, %10s\n',...
79          'frequency', 'amplitude', 'oct_mu','oct_std', 'wat_mu','wat_std');
```

```
80      % print the image extperimental data set pixel values to the file
81      fprintf(fileID,'%10.0f, %10.0f, %10.6f, %10.6f, %10.6f, %10.6f\n',...
82          data);
83      %close the file
84      fclose(fileID);
85  end
```

`writeData` function

```
function [] = writeData(subset, Data, LgP_mean, LgP_std, LgP_stdPercent)
% Writes the calculated partitioning information to the relevant
% experimental set file. The files are constant frequency and constant
% amplitude.
    %%
    % create the accumulated data file name
    dataname = 'Data';
    if (strlength(subset)) == 0
        dataname = strcat(dataname,'.txt');
    else
       dataname = strcat(dataname,'_',subset,'.txt');
    end

    % accumulated data file
    fileID = fopen(dataname,'w+');
    fprintf(fileID,'%10s, %10s, %10s\n', ...
        'frequency','amplitude','mean_logP');
    fclose(fileID);

    for freq=1:10
        % list of the experimental set (constant) frequency
        Freq = ones(1,15).*freq;
        % extract the relevant experimental set data from the Data matrix
        data(:,:) = Data(freq,:,:);

        % list of the experimental set (control variable) amplitude
        amp  = [0:10:100];
        if (freq == 5)
            amp = [amp,200,250,300,400];

        elseif (freq == 6) || (freq == 10)
            amphigh = 500;
            amp = [amp,200:100:amphigh];

        elseif (freq == 7) || (freq == 8) || (freq == 9)
            amphigh = 800;
            amp = [amp,200:200:amphigh];
        else
```

```
39              amp = [amp, nan, nan, nan, nan];
40          end
41
42          % create the experimental set (frequency) file name
43          if (strlength(subset)) == 0
44              name = strcat(num2str(freq),'MHz');
45
46          else
47              name = strcat(num2str(freq),'MHz_',subset);
48          end
49          name = strcat(name,'.txt');
50
51          % open the the file
52          fileID = fopen(name,'w+');
53          % create the file headder
54          fprintf(fileID,'%10s, %10s, %10s, %10s, %10s\n', ...
55              'frequency','amplitude','mean_logP','std_logP', 'std_percent');
56          % print the statistical information to the file
57          fprintf(fileID,'%10.0f, %10.0f, %10.6f, %10.6f, %10.2f\n', ...
58              [Freq;amp;...
59              LgP_mean(freq,:); LgP_std(freq,:); LgP_stdPercent(freq,:)]);
60          %close the file
61          fclose(fileID);
62
63          % append to accumulated data file
64          fileID = fopen(dataname,'a+');
65          fprintf(fileID,'%10.0f, %10.0f, %10.6f\n',...
66              [Freq;amp;LgP_mean(freq,:)]);
67          fclose(fileID);
68
69          %%
70          name = replace(name,'.txt','');
71          name = strcat(name,'_data.txt');
72
73          % create the file headder for the experimental set partition values
74              % for each image (constant frequency)
75          format = '%10s, %10s';
76          vars(1,1:2) = ["frequency","amplitude"];
77          for i=1:10
78              format = strcat(format,', %10s');
79              vars(1,i+2) = strcat("logP",num2str(i));
```

```
80          end
81          format = strcat(format,"\n");
82
83          % create the file for the partition data for the images of the
84              % experimental set
85          fileID = fopen(name,'w+');
86          fprintf(fileID,format,vars);
87          % add the data, with correct formatting
88          format = '%10.0f, %10.0f';
89          for i=1:10
90              format = strcat(format,', %10.6f');
91          end
92          format = strcat(format,'\n');
93          fprintf(fileID,format,[Freq;amp;data']);
94          %close the file
95          fclose(fileID);
96      end
97      % clear the temporary data
98      data = [];
99      for pressureInd=1:11
100         % list of the experimental set (constant) pressure
101         Pressure = ones(1,10).*(pressureInd-1)*10;
102         % extract the relevant experimental set data from the Data matrix
103         data(:,:) = Data(:,pressureInd,:);
104         % list of the experimental set (control variable) frequency
105         Freq  = [1:10];
106
107         % create the experimental set (amplitude) file name
108         if (strlength(subset)) == 0
109             name = strcat(num2str((pressureInd-1)*10),'kPa');
110
111         else
112             name = strcat(num2str((pressureInd-1)*10),'kPa_',subset);
113         end
114         name = strcat(name,'.txt');
115
116         % open the the file
117         fileID = fopen(name,'w+');
118         % create the file headder
119         fprintf(fileID,'%10s, %10s, %10s, %10s, %10s\n',...
120             'frequency','amplitude','mean_logP','std_logP', 'std_percent');
```

```
121         % print the statistical information to the file
122         fprintf(fileID,'%10.0f, %10.0f, %10.6f, %10.6f, %10.2f\n',...
123             [Freq;Pressure;...
124             LgP_mean(:,pressureInd)';...
125             LgP_std(:,pressureInd)';...
126             LgP_stdPercent(:,pressureInd)']);
127         %close the file
128         fclose(fileID);
129 
130         %%
131         name = replace(name,'.txt','');
132         name = strcat(name,'_data.txt');
133 
134         % create the file headder for the experimental set partition values
135             % for each image (constant amplitude)
136         format = '%10s, %10s';
137         vars(1,1:2) = ["frequency","amplitude"];
138         for i=1:10
139             format = strcat(format,', %10s');
140             vars(1,i+2) = strcat("logP",num2str(i));
141         end
142         format = strcat(format,"\n");
143 
144         % create the file for the partition data for the images of the
145             % experimental set
146         fileID = fopen(name,'w+');
147         fprintf(fileID,format,vars);
148         % add the data, with correct formatting
149         format = '%10.0f, %10.0f';
150         for i=1:10
151             format = strcat(format,', %10.6f');
152         end
153         format = strcat(format,'\n');
154         fprintf(fileID,format,[Freq;Pressure;data']);
155         %close the file
156         fclose(fileID);
157     end
158 end
```

Appendix E

Partition Coefficient

Partitioning is the generalised term given to the favourability of a substance between two other materials in intimate contact. Contextually of importance is the octanol-water partition coefficient for quantifying hydrophobicity. The general details related to the octanol-water partition coefficient are covered with related thermodynamic principles.

The octanol-water partition coefficient is defined as the ratio of the concentration of a test species in octanol to that of water [1]. It is commonly reported in decade log form. Octanol and water are immiscible. However, they do have partial mutual solubility. The terminology is modified to the organic phase, which is octanol with a saturated amount of water, and the aqueous phase, which is water with a saturated amount of octanol. The partition ratio is therefore modified to be the ratio of the concentration of a test species in the organic phase to the aqueous phase [1]. This value is approximately equal to the original definition [1]. The equations relating to the concepts discussed above are as follows

$$P = \frac{c_x^{oct}}{c_x^{w}} \tag{E.1}$$

$$P \approx \frac{c_x^{org}}{c_x^{aq}} \tag{E.2}$$

$$log(P) = log\left(\frac{c_x^{org}}{c_x^{aq}}\right) \tag{E.3}$$

where, P is the partition coefficient; c_x is the concentration of the sample test species with superscripts denoting the particular phase.

The concentration of the sample test species in each phase is governed by the chemical thermodynamic processes of the mixtures [1]. When partitioning occurs and thermodynamic equilibrium is reached, the chemical potential of the sample in each phase is equal. For the sample in each (octanol and water) phase, the chemical potential is given as

$$\mu_x = \mu_x^0 + \mathcal{R}\Theta ln\left(\mathfrak{a}_x\right) \tag{E.4}$$

where, μ_x is the chemical potential of the species in solution; μ_x^0 is the chemical potential of the pure species; $\mathcal{R}$ is the gas constant; Θ is the temperature; and $\mathfrak{a}_x$ is the activity of the substance [1]. The activity $\mathfrak{a}_x$ is equal to $h_x\psi_x$ where h_x is the Henrian activity coefficient for dilute solutions [1, 2]. Importantly the volume fraction ψ_x is equal to the product of the molar volume Υ_x and the concentration c_x [1, 2]. Then the chemical potential becomes

$$\mu_x = \mu_x^0 + R\Theta ln\left(h_x c_x \Upsilon_x\right) \tag{E.5}$$

When partitioning is complete, the chemical potentials are equal for both phases, $\mu_x^{org} = \mu_x^{aq}$ is assumed, and the phases can be compared. This results in the following simplification,

$$\mu_x^{org} = \mu_x^{aq} \tag{E.6}$$

$$\mu_x^0 + R\Theta ln\left(\mathfrak{a}_x^{org}\right) = \mu_x^0 + R\Theta ln\left(\mathfrak{a}_x^{aq}\right) \tag{E.7}$$

$$\Rightarrow \mathfrak{a}_x^{org} = \mathfrak{a}_x^{aq} \tag{E.8}$$

$$h_x^{org} c_x^{org} \Upsilon_x^{org} = h_x^{aq} c_x^{aq} \Upsilon_x^{aq} \tag{E.9}$$

If the molar volume is assumed to be equal for both phases, $\Upsilon_x^{org} = \Upsilon_x^{aq}$, then the equation simplifies effectively to an equivalent form of the partitioning coefficient

$$log(P) = log\left(\frac{c_x^{org}}{c_x^{aq}}\right) = log\left(\frac{h_x^{aq}}{h_x^{org}}\right) \tag{E.10}$$

This demonstrates that the partitioning coefficient is equivalent to the ratio of the Henrian activity coefficients of the substance h_x, in water and octanol [1]. This is derived from the activity $\mathfrak{a}_x$ of a substance in a real solution. The activity of a substance in solution accounts for the transition from Henry's Law of dilute-ideal to Raoult's Law of ideal solutions. Although this makes the partition coefficient invariant to all concentrations, it is assumed that a test species follows Henry's Law up to saturation [1].

Temperature plays a role in the thermodynamics of solutions, but the partition coefficient is relatively insensitive to temperature changes [1]. However, it is recommended to evaluate the octanol-water partition coefficient at $25°C$.

Additionally, the chemical potential μ_x as a thermodynamic variable is a hidden mechanism in the partitioning coefficient and the partitioning phenomenon.

E.1 Maximum Particle Dispersion Method

A recent method has been proposed to measure the hydrophobicity of micro- and nanoparticles, the maximum particle dispersion method [3]. Although this method is not central to the proposed research nor its method, it does provide some insight into the relationship between chemical thermodynamics, such as intermolecular forces and surface thermodynamics, particularly the surface free energy of microparticles.

The maximum particle dispersion method used to measure the Surface Free Energy of micro- and nanoparticles [3]. The Method uses surface free energy as a quantitative measure to describe the hydrophobicity of the particles. This method presented by [3] is briefly discussed below.

The method uses probing liquids into which a sample of the particles is mixed. The probing liquids used consisted of analytical grade water and ethanol. Other long-chain alkane hydrocarbons were also used in place of ethanol. The theoretical principle is

based on the van der Waals intermolecular attraction of colloidal systems. Particles will maximally disperse in a liquid with equal Surface Free Energy values. If particles do not disperse, then they cluster and either sink or float. This is then quantified by the optical density of the probing mixture. The Surface Free Energy is equivalent to the probing liquid's surface tension. The alkanes used had relatively low surface tension, $16.00 - 27.47\ mJ/m^2$. Mixtures of various concentrations of ethanol and water, ranging from pure ethanol to pure water, were prepared. The surface tensions of these mixtures range from pure ethanol $22.10 mJ/m^2$ to pure water $72.80 mJ/m^2$.

The particle material is prapared in a stock solution. A trace amount of the sample of the stock is added to the different probing liquids, vortexed and left undisturbed for 10-30 min to sediment. If sedimentation was too slow, the samples were centrifuged. The optical density of these mixtures is measured with a characteristic wavelength of $400nm$. The optical densities are plotted against the probing liquid's surface tension. The peak of the curve-fitted date is found and defined as the surface free energy of the micro- or nanoparticle material. The measurements were found to be in close agreement with existing literature. The particles investigated ranged in size from $50nm$ to $5\mu m$, as well as shape and composition.

One of the theoretical limitations of the method is that it relies on the van der Waals forces of colloidal systems and colloidal stability [3]. Additional intermolecular forces may dominate for very hydrophilic materials with high surface free energy values. This then falls out of the theoretical principle of the maximum particle dispersion method presented by [3]. One of the practical limitations is the method cannot measure particles that dissolve in the probing liquids. Another limitation is that particles with refractive indices equal to or comparable to that of the particular probing liquid cannot be measured. These limitations can be resolved by selecting another probing liquid with a similar surface tension that does not dissolve the particles or has a different refractive index.

References

[1] J. Sangster, 'Octanol-water partition coefficients of simple organic compounds,' *Journal of Physical and Chemical Reference Data*, vol. 18, no. 3, pp. 1111–1229, Jul. 1989.

[2] P. W. Atkins and J. de Paula, *Atkins' Physical chemistry*. New York: W.H. Freeman, 2006.

[3] Z. Cao, S. N. Tsai and Y. Y. Zuo, 'An optical method for quantitatively determining the surface free energy of micro- and nanoparticles,' *Analytical Chemistry*, vol. 91, no. 20, pp. 12 819–12 826, Sep. 2019.

Appendix F

Contact Angle and Surface Tension

The contact angle is the angle measured and defined in a three-phase system [1]. In an everyday context, these phases are a given solid material, liquid water, and the ambient atmosphere [1]. The solid is assumed locally flat and smooth [1, 2]. These phases meet at a common interface line. For simplicity, this is analysed in a two-dimensional section [1]. In circumstances where the bulk solid material is a curved surface, the tangent plane of the solid at the three-phase contact line is used, and subsequently an ordinary two-dimensional section is analysed [1]. The concept is generally extended to include general three-phase systems with general contact angles [2]. The phases are denoted with the symbol φ and a relevant subscript. The interfaces are denoted with the symbol ς and a subscript of the relevant two phases. The generalised contact angle phenomenon can be seen in Figure F.1a. The interfaces also denote the surface tension between the two phases. Surface tension is discussed below.

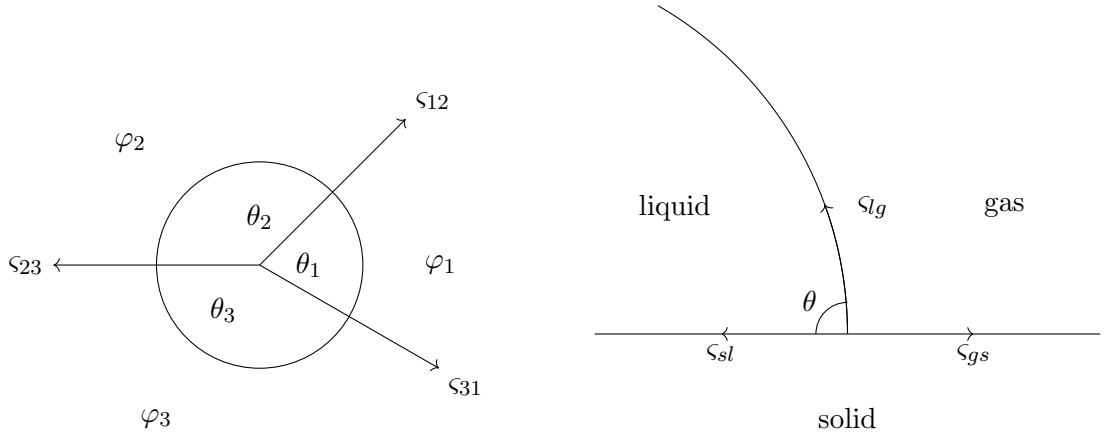

(a) General three-phase

(b) Solid-Liquid-Gas

Figure F.1: Contact Angle

Analysing the three-phase interfaces in Figure F.1b, the contact angle is defined as the angle formed between the solid-liquid interface and the liquid-gas interface. It is also referred to as the liquid angle. A hydrophobic surface is classified as having a contact angle > 90, while a hydrophilic surface has a contact angle < 90.

A force balance analysis of the surface tension geometry gives rise to Young's contact angle equation

$$cos(\theta) = \frac{\varsigma_{sg} - \varsigma_{sl}}{\varsigma_{lg}} \tag{F.1}$$

where, θ is the contact angle; and ς are the surface tensions with subscripts (s-solid, l-liquid, g-gas) indicating the particular interfaces [1–3]. This quantifies the relationship between the measured contact angle and the surface tension of the three interfaces.

F.1 Surface Tension

Surface tension is defined as the ratio of proportionality between the energy required to deform a surface to the change in the area that occurs under the deformation, given as

$$\frac{\partial W}{\partial A} = \varsigma \tag{F.2}$$

where, W is the energy; A is the surface area; and ς is the surface tension [1, 2]. Subsequently, it has units of Joules per unit square meter ($\mathrm{J\,m^{-2}}$) and is dimensionally equivalent to Newtons per meter ($\mathrm{Nm^{-1}}$) [1, 2].

Surface tension can be interpreted at a molecular scale. Molecules of a bulk condensed phase experience intermolecular forces [1]. For molecules in the bulk material, the forces balance due to the other surrounding molecules [1]. At an interface, the molecules are in an unbalanced state due to being only partially surrounded by other molecules [1]. This is thermodynamically unfavourable [1]. Excess energy is therefore required to move and keep a molecule at the interface [1]. This is defined as the surface excess or surface free energy [1]. The effect of surface tension is to minimise the surface area to minimise this excess energy [1]. Since surface tension is governed by inter-molecular forces and is a thermodynamic phenomenon, the value of surface tension is dependent on the composition of the material, its vapour or surrounding material, the ambient pressure and temperature [1, 2].

Surface thermodynamics can also be extended to curved surfaces of liquids [1, 2]. At thermodynamic equilibrium, if a liquid surface is curved, then there is a pressure difference across the interface [1, 2]. This pressure difference is equal to the product of the surface tension with the arithmetic curvature of the surface [1, 2]. The arithmetic curvature is simply the sum of the two principle curvatures, i.e. the reciprocals of the two principle radii. This is represented as the Young-Laplace equation,

$$\Delta\ P = \varsigma \left(\frac{1}{R_1} + \frac{1}{R_2} \right) \tag{F.3}$$

where, $\Delta\ P$ is the pressure difference; ς is the surface tension; and R_1 and R_2 are the principle radii [1, 2]. For a spherical surface, the radii are equal, i.e. $R_1 = R_2 = R_0$, and the arithmetic curvature is simply two times the reciprocal of the radius. This reduces the Young-Laplace equation to

$$\Delta\ P = \frac{2\varsigma}{R_0} \tag{F.4}$$

Equation F.4 is a fundamental starting point for analysing bubble dynamics [1, 2, 4].

This equation applies to liquid droplets in air, or gaseous bubbles in liquids, since both surfaces are curved spherical surfaces [1, 2]. It fundamentally describes the relationship between a bubble's pressure, specifically the pressure difference across its surface, the surface tension, and the bubble radius [1, 2, 4]. Appendix G explores the thermodynamics of bubbles further, using Equation F.4 as the fundamental starting point.

References

[1] H.-J. Butt, K. Graf and M. Kappl, *Physics and Chemistry of Interfaces*. Wiley, Sep. 2003.

[2] A. Neumann, R. David and Y. Zuo, Eds., *Applied Surface Thermodynamics*. CRC Press, Oct. 2010.

[3] A. I. Rusanov, N. E. Esipova and V. D. Sobolev, 'Strong dependence of contact angle on pressure,' *Doklady Physical Chemistry*, vol. 487, no. 1, pp. 87–90, Jul. 2019.

[4] M. Postema, *Fundamentals of Medical Ultrasonics*. London: CRC Press, 2011.

Appendix G

Bubble Dynamics

The relationship between a bubble's radius and the bubble pressure is central to the nature of bubble dynamics. The foundation of bubble statics, relating the balance between a bubble's radius and pressure, is described before bubble dynamics is analysed.

G.1 Bubble Statics

It is important to understand bubble statics to analyse a bubble in dynamic conditions. The fundamentals of bubble statics starts with a bubble, as illustrated in Figure G.1, and the Young-Laplace equation,

$$\Delta\ P = \frac{2\varsigma}{R_0} \tag{G.1}$$

which describes the relationship between the radius of a bubble, the liquid-gas surface tension, and the pressure difference across the bubble interface [1, 2]. This was explained in the last two paragraphs of Appendix F. This is also derived from the force balance of an area section A through the spherical bubble,

$$\Delta P \mathcal{A} = \varsigma S \tag{G.2}$$

where, ΔP is the pressure difference; $\mathcal{A}$ is the cross-section area of the bubble; ς is the surface tension; and S is the circumference (generally the surface perimeter) [2]. The

area can be expressed as $\pi {R_0}^2$, while the circumference as $2\pi R_0$, giving

$$\Delta P \left(\pi {R_0}^2\right) = \varsigma \left(2\pi R_0\right) \tag{G.3}$$

$$\Rightarrow \Delta\ P = \frac{2\varsigma}{R_0} \tag{G.4}$$

as before. What is of particular interest is how a bubble, and particularly its radius, might behave when exposed to a changing pressure gradient. To do this, the analysis of the unforced static bubble is necessary. The schematic of a bubble Figure G.1 is used further to aid in visual interpretation of the unforced static bubble system.

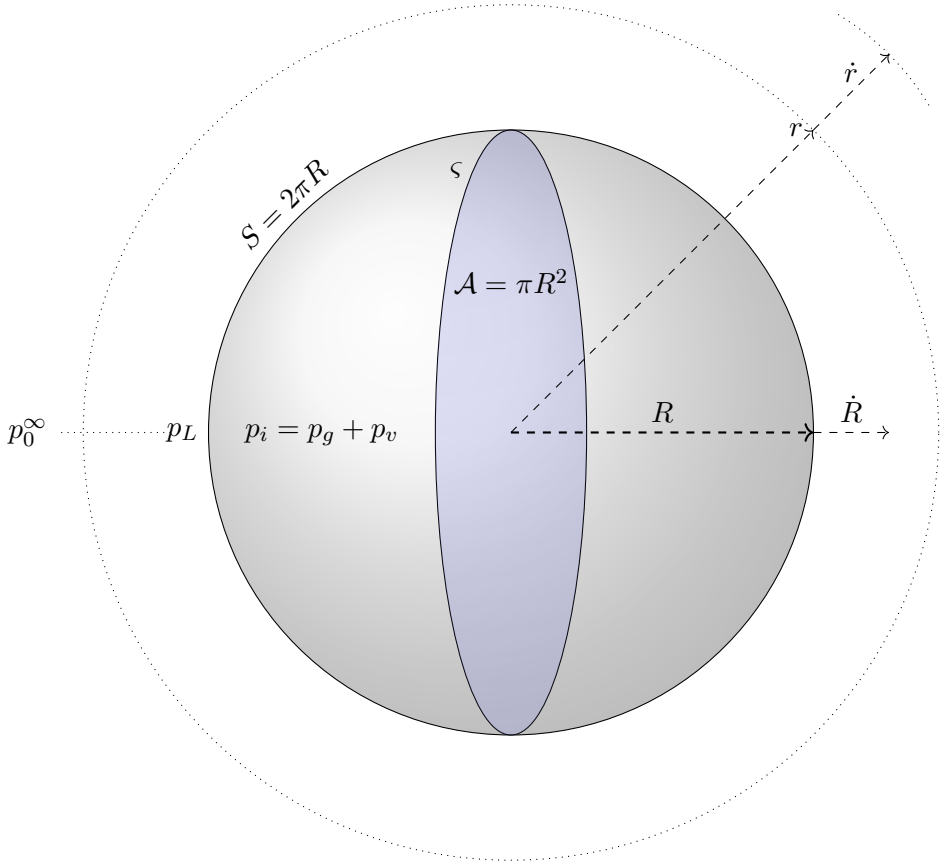

Figure G.1: Bubble Schematic

The analysis of the static bubble is described in detail below (and guided by [2–5]). Importantly the bubble is in a quasi-static state. Over long time periods bubbles are unstable due to the pressure difference across the interface driving a mass transfer of the

internal vapour and gas across the interface [2–5]. The bubble is assumed to compose of gas and liquid vapour, each forming the internal pressure $p_i = p_g + p_v$. The external pressure p_0^∞ is the ambient pressure of the liquid assumed uniform and infinitely far (for simplicity, this is indicted as p_0). Thus the pressure difference across the bubble liquid-gas interface is $\Delta P = p_i - p_0 = p_g + p_v - p_0$. Substituting in the Young-Laplace Equation G.1 for ΔP with the different pressures and reordering gives

$$p_g = p_0 - p_v + \frac{2\varsigma}{R_0} \tag{G.5}$$

The gas in the bubble is assumed polytropic, where the relationship

$$p_g V^\gamma = \text{constant} \tag{G.6}$$

holds [2–6]. Here p_g is the gas partial pressure as above, V is the volume of gas, and $\gamma = \frac{C_P}{C_V}$ is the ratio of specific heats of the gas, at constant pressure C_P, and constant volume C_V [2, 6]. This is characteristic of an adiabatic and reversible process, essentially there is no heat or mass transfer between the gas in the bubble and the surrounding liquid, and temperature is assumed constant [2–6]. Equation G.6 enables the comparison between two adiabatic processes with different pressure and volume. Assume the initial conditions for a bubble are an initial radius R_0 and subsequent volume V_0, and the partial pressure of the gas p_g is given in Equation G.5. Then for any other condition with the instantaneous pressure at the liquid interface all around the bubble p_L, and the associated radius is R and volume V, the equation becomes

$$\left(p_0 - p_v + \frac{2\varsigma}{R_0}\right) V_0^\gamma = \left(p_L - p_v + \frac{2\varsigma}{R}\right) V^\gamma \tag{G.7}$$

Recognising that $V_0 = \frac{4}{3}\pi R_0^3$ and $V = \frac{4}{3}\pi R^3$, substituting and rearranging in terms of the liquid interface pressure gives,

$$p_L = \left(p_0 - p_v + \frac{2\varsigma}{R_0}\right)\left(\frac{R_0}{R}\right)^{3\gamma} + p_v - \frac{2\varsigma}{R} \tag{G.8}$$

Equation G.8 describes the relation of the instantaneous external surface pressure p_L of a bubble and the bubble radius R [2–5]; given initial conditions of the ambient pressure p_0 and the initial radius R_0. One important assumption is that the interface pressure is assumed to be uniform across the entire bubble surface [2].

In summary, Equation G.8 is the force-balanced equation of bubble dynamics under static pressure conditions. Next, Equation G.8 is discussed under dynamic pressure conditions, giving rise to bubble dynamics.

G.2 Forced bubble dynamics

The dynamics of bubbles are continued from the quasi-static bubble analysis and assisted further by [2–5]. This section specifically assists the reader through the theory and derivation of the fundamental equation of bubble dynamics. The equation of bubble dynamics fundamentally describes the relationship between a bubble's radius (and the radial velocity) and an externally forced bulk dynamic pressure. Additionally, the fundamental equation is modified to describe the dynamics of antibubbles.

The schematic of a bubble Figure G.1 is used further in the discussion on bubble dynamics below. If the liquid interface pressure of a bubble changes, its radius changes accordingly. When a bubble changes radius, it displaces the liquid surrounding it, causing a flow of the liquid. The mass displaced by the moving bubble interface must equal the mass flow in the liquid [2–5]. Suppose a bubble changes radius from R_0 to R, and consider the liquid flow at a point $r > R$ outside the bubble. Then the velocity of the liquid anywhere outside the bubble is simply $\dot{r}$, and the velocity of the liquid at the bubble interface is $\dot{R}$. The mass flow rate is conserved, assuming the liquid is incompressible. The mass flow rate of the liquid $\dot{m}$ is equal to the volume flow rate of the liquid at a specific radius V_x, multiplied by the density of the fluid ρ. The mass flow rate balance is then

$$\dot{m_R} = \dot{m_r} \tag{G.9}$$

$$\rho\dot{V_R} = \rho\dot{V_r} \tag{G.10}$$

$$\rho\mathcal{A}_R\dot{R} = \rho\mathcal{A}_r\dot{r} \tag{G.11}$$

$$\rho\ 4\pi R^2\ \dot{R} = \rho\ 4\pi r^2\ \dot{r} \tag{G.12}$$

$$\Rightarrow \dot{r} = \left(\frac{R}{r}\right)^2 \dot{R} \tag{G.13}$$

Equation G.13 is characteristic of an incompressible fluid flow [4, 5]. The liquid mass flow has kinetic energy, which must equal the thermodynamic work done by the bubble [2–5]. The adiabatic reversible work of the bubble is then

$$W = \int_{V_i}^{V_f} (p_f - p_i)\, dV \tag{G.14}$$

as described by [4].

The volume of a sphere is $V = \frac{4}{3}\pi R^3$. The final pressure $p_f = p_L$ and the initial pressure is $p_i = p_0$. The differential dV can be calculated from the volume of a sphere and is $dV = 4\pi R^2 dR$. Substituting this and working through the expression, the equations below follows [2–5],

$$W = \int_{R_0}^{R} (p_L - p_0)\, 4\pi R^2 dR \tag{G.15}$$

$$W = (p_L - p_0)\, 4\pi \int_{R_0}^{R} R^2 dR \tag{G.16}$$

$$W = \frac{4}{3}\pi\, (p_L - p_0)\left(R^3 - R_0^3\right) \tag{G.17}$$

As mentioned before, this work must equal the kinetic energy of the liquid mass flow. The kinetic energy of the liquid mass flow in a time period is simply,

$$K_E = \int \frac{1}{2} v^2 \frac{dm}{dt} dt \tag{G.18}$$

$$K_E = \int \frac{1}{2} v^2 dm \tag{G.19}$$

As mentioned, the mass of a volume of liquid is $m = \rho V$, and considering the mass flow rate, volume flow rate relationship $\dot{m} = \rho \dot{V}$, then $dm = \rho dV = \rho 4\pi r^2 dr$. Additionally, the velocity of the flow is given by $v = \dot{r}$. Substituting and integrating over the entire liquid volume, from $r > R$ to ∞ gives,

$$K_E = \int_{R}^{\infty} \frac{1}{2} \dot{r}^2 \rho 4\pi r^2 dr \tag{G.20}$$

$$K_E = 2\pi\rho \int_{R}^{\infty} \dot{r}^2 r^2 dr \tag{G.21}$$

as seen in [2–5]. Then substituting in the relation between $\dot{r}$ and $\dot{R}$ from Equation G.13 gives,

$$K_E = 2\pi\rho \int_{R}^{\infty} \left(\left(\frac{R}{r}\right)^2 \dot{R}\right)^2 r^2 dr \tag{G.22}$$

$$K_E = 2\pi\rho \int_{R}^{\infty} R^4 \dot{R}^2 \frac{1}{r^2} dr \tag{G.23}$$

$$K_E = 2\pi\rho R^4 \dot{R}^2 \int_{R}^{\infty} \frac{1}{r^2} dr \tag{G.24}$$

$$K_E = 2\pi\rho R^3 \dot{R}^2 \tag{G.25}$$

as explained in [2–5]. Equating the adiabatic volumetric work from Equation G.17 and the kinetic energy from Equation G.25 gives,

$$\frac{4}{3}\pi\left(p_L - p_0\right)\left(R^3 - R_0^3\right) = 2\pi\rho R^3\dot{R}^2 \tag{G.26}$$

Differentiating this equation with respect to the bubble radius R gives,

$$\frac{4}{3}\pi\left(p_L - p_0\right)\frac{d}{dR}\left(R^3 - R_0\right) = 2\pi\rho\frac{d}{dR}\left(R^3\dot{R}^2\right) \tag{G.27}$$

Working through the derivative and applying the product rule where necessary gives the following,

$$\frac{4}{3}\pi\left(p_L - p_0\right)\left(3R^2 - 0\right) = 2\pi\rho\left[\left(\frac{d}{dR}R^3\right)\dot{R}^2 + R^3\left(\frac{\partial}{\partial R}\dot{R}\dot{R}\right)\right] \tag{G.28}$$

$$4\pi\left(p_L - p_0\right)R^2 = 2\pi\rho\left[3R^2\dot{R}^2 + R^3\left(\left(\frac{\partial}{\partial R}\frac{dR}{dt}\right)\dot{R} + \left(\frac{\partial}{\partial R}\frac{dR}{dt}\right)\dot{R}\right)\right] \tag{G.29}$$

$$4\pi\left(p_L - p_0\right)R^2 = 2\pi\rho\left[3R^2\dot{R}^2 + R^3\left(\frac{d}{dt}\dot{R} + \frac{d}{dt}\dot{R}\right)\right] \tag{G.30}$$

$$4\pi\left(p_L - p_0\right)R^2 = 2\pi\rho\left[3R^2\dot{R}^2 + 2R^3\ddot{R}\right] \tag{G.31}$$

$$\Rightarrow \frac{1}{\rho}\left(p_L - p_0\right) = \frac{3}{2}\dot{R}^2 + R\ddot{R} \tag{G.32}$$

as seen in [2–5]. This equation relates the position R, velocity $\dot{R}$, and acceleration $\ddot{R}$ of the bubble wall through a non-linear equation with the pressure difference between the bubble wall p_L and the ambient pressure p_0, and the liquid density ρ. Assume that the pressure is now forced, the ambient pressure term p_0 is modified to the sum of the ambient pressure with a superimposed pressure signal $p_0 = p_0 + P(t)$. Substituting the forced pressure into Equation G.32 provides the dynamic component of bubble behaviour

$$\frac{1}{\rho}\left(p_L - p_0 - P(t)\right) = \frac{3}{2}\dot{R}^2 + R\ddot{R} \tag{G.33}$$

Rearranging and substituting the dynamic component Equation G.33 with the statics component Equation G.8; specifically substituting the expression of the liquid pressure p_L at the bubble wall gives,

$$\frac{3}{2}\dot{R}^2 + R\ddot{R} = \frac{1}{\rho}\left[\left(p_0 - p_v + \frac{2\varsigma}{R_0}\right)\left(\frac{R_0}{R}\right)^{3\gamma} + p_v - \frac{2\varsigma}{R} - p_0 - P(t)\right] \tag{G.34}$$

This is the fundamental equation of bubble dynamics subject to a uniform bulk dynamic pressure $P(t)$ and is called the Rayleigh-Plesset Equation [2–5]. Equation G.34 is used to further describe the behaviour of microbubbles in a uniform acoustic sound field.

G.2.1 Behaviour of oscillating microbubbles in a sound filed

Any type of microbubble in a fluid, either as an ordinary bubble, ultrasound contrast agent or an antibubble, is acoustically active [2, 7–10]. Bubbles exposed to ultrasound experience forces that cause the bubble to oscillate, which in turn causes the bubble to radiate its own spherical wave acoustic field. This can result in the bubble translating due to primary radiation forces [2, 11] and attract or repel other bubbles due to secondary radiation forces [2].

The primary radiation force results from a bubble oscillating in a sound field [2, 11]. The changing pressure of the sound field changes the bubble volume due to the compressibility of the gas. The applied acoustic field has a resonance radius associated with the centre frequency of the sound field [2, 11]. If there is a standing wave sound field, then any bubble with a radius larger than resonance will translate to the nodes (N) of the sound field, where the least dynamic pressure changes occur [11]. Bubbles with a smaller radius than resonance will translate to the antinodes (AN), where the most dynamic pressure changes occur [11]. An example of the translation caused by a standing wave acoustic field, with bubbles having radii less than and larger than the resonance radius, are seen in Figure G.2a to G.2d. In a travelling wave, the dynamics are similar. The larger bubbles translate away from the acoustic focus, while smaller bubbles translate towards the acoustic focus [11].

Secondary radiation forces result from bubbles' interaction with other bubbles' sound fields. Typically, bubbles that oscillate in phase attract, while bubbles that oscillate out of phase will repel [12]. A visual of the clustering that results can be seen in Figures G.2e and G.2f for bubbles with radii less than and larger than resonance.

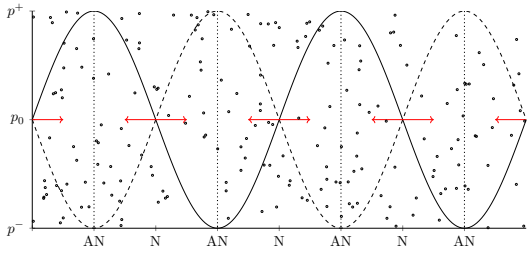

(a) $R_0 < R_{f_0}$

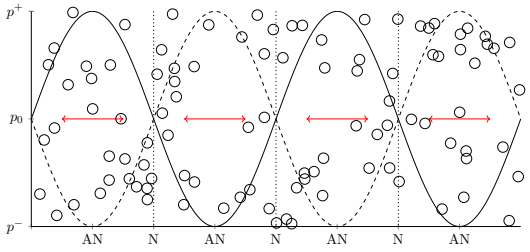

(b) $R_0 > R_{f_0}$

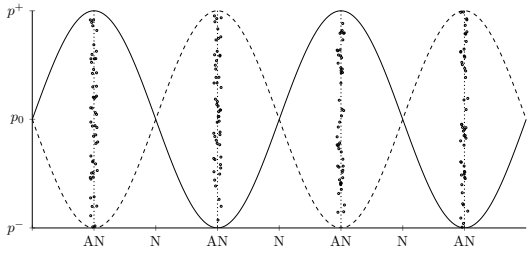

(c) $R_0 < R_{f_0}$ spatial separation (primary forces)

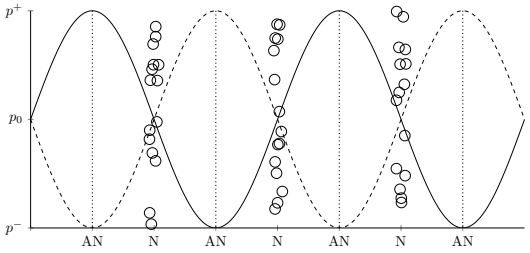

(d) $R_0 > R_{f_0}$ spatial separation (primary forces)

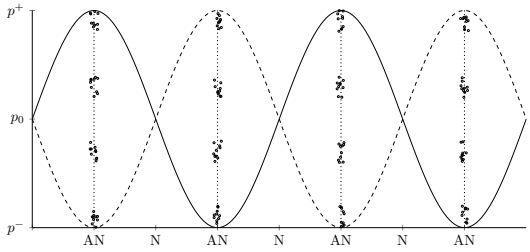

(e) $R_0 < R_{f_0}$ clustering (secondary forces)

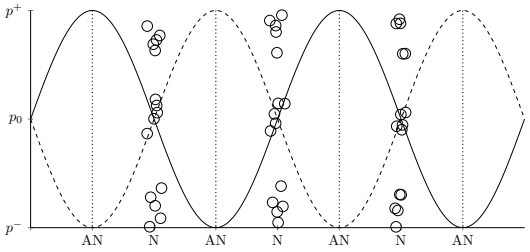

(f) $R_0 > R_{f_0}$ clustering (secondary forces)

Figure G.2: Translation due to primary and secondary forces

Bubbles oscillate symmetrically at relatively low acoustic amplitudes. However, bubbles oscillate asymmetrically at higher amplitudes with noticeable harmonics in their frequency spectrum [9, 10]. High acoustic amplitudes can result in the fragmentation of the bubble. Antibubbles, like ordinary bubbles, behave very similarly in an acoustic field. Due to the presence of the incompressible core, however, antibubbles oscillate more asymmetrically and at lower acoustic amplitudes [9, 10, 13, 14]. This results in the harmonics of antibubbles having a comparable magnitude to the fundamental [9, 10, 14]. The resonance frequency of the bubble can be derived from the fundamental equation of bubble dynamics Equation G.34 (the Rayleigh-Plesset Equation) [2, 4].

Equation G.34 is easily modified for antibubble dynamics as explained by [10]. Consider the factor $\left(\frac{R_0}{R}\right)^{3\gamma}$ and how is is derived from the volume of the polytropic gas Equation G.6. For an antibubble the gas volume is a fraction of the entire volume of the bubble and is simply modified. This modification can be expressed for the two conditions as

$$V_0 = V_{R_0} - V_{R_c} \qquad V = V_R - V_{R_c} \tag{G.35}$$

$$V_0 = \frac{4}{3}\pi R_0^3 - \frac{4}{3}\pi R_c^3 \qquad V = \frac{4}{3}\pi R^3 - \frac{4}{3}\pi R_c^3 \tag{G.36}$$

$$V_0 = \frac{4}{3}\pi\left(R_0^3 - R_c^3\right) \qquad V = \frac{4}{3}\pi\left(R^3 - R_c^3\right) \tag{G.37}$$

therefore combining the equations for both conditions gives,

$$\Rightarrow \frac{V_0}{V} = \left(\frac{R_0^3 - R_c^3}{R^3 - R_c^3}\right) \tag{G.38}$$

where V_0 is the initial volume and V is the final volume. V_{R_0} is the initial and V_R is the final total volume occupied by the antibubble. V_{R_c} is the incompressible core volume with corresponding radius R_c. The gas volumes are simply the difference between the total volume and the particle volume [10]. Substituting this new volume ratio and following the same mathematical reasoning as before, Equation G.34 is modified as explained in [10] and becomes,

$$\frac{3}{2}\dot{R}^2 + R\ddot{R} = \frac{1}{\rho}\left[\left(p_0 - p_v + \frac{2\varsigma}{R_0}\right)\left(\frac{R_0^3 - R_c^3}{R^3 - R_c^3}\right)^{\gamma} + p_v - \frac{2\varsigma}{R} - p_0 - P(t)\right] \tag{G.39}$$

Equation G.39 is further modified to include the nonlinear effects of the asymmetrical oscillation caused by the presence of the incompressible core for further generalisation. This simply introduces a factor of $\dfrac{1}{1 - \left(\dfrac{R_c}{R_0}\right)^2}$ to the $\dfrac{2\varsigma}{R_0}$ terms, making them $\dfrac{2\varsigma R_0}{{R_0}^2 - {R_c}^2}$.

Equation G.39 subsequently becomes,

$$\frac{3}{2}\dot{R}^2 + R\ddot{R} = \frac{1}{\rho}\left[\left(p_0 - p_v + \frac{2\varsigma R_0}{{R_0}^2 - {R_c}^2}\right)\left(\frac{R_0^3 - R_c^3}{R^3 - R_c^3}\right)^{\gamma} + p_v - \frac{2\varsigma R}{R^2 - {R_c}^2} - p_0 - P(t)\right] \tag{G.40}$$

This is then linearised and rearranged to solve for the resonant frequency of an antibubble. The relationship between antibubble radius and the resonance frequency is given in Equation G.41 with the associated variable descriptions in **??**. (these values are assumed for water at normal temperature and pressure (NTP)).

$$f_0 = \frac{1}{2\pi R_0\sqrt{\rho}}\sqrt{\left(3\gamma\left(\frac{p_0 - p_v + \frac{2\varsigma R_0}{{R_0}^2 - {R_c}^2}}{1 - \left(\frac{R_c}{R_0}\right)^3}\right) - \frac{2\varsigma R_0}{{R_0}^2 - {R_c}^2}\right)} \tag{G.41}$$

To show the relationship graphically, the resonant frequency of antibubbles ranging from $1-1000\mu m$ with different core ratios is given in Figure G.3 below. The resonant frequency of an antibubble is inversely proportional to the antibubble radius. Additionally, as the core ratio increases, the resonance frequency increases significantly.

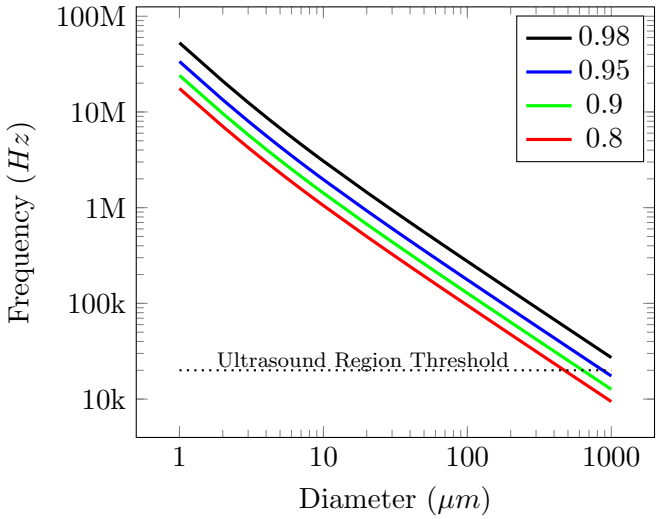

Figure G.3: Antibubble resonance frequency for different core ratios

References

[1] H.-J. Butt, K. Graf and M. Kappl, *Physics and Chemistry of Interfaces*. Wiley, Sep. 2003.

[2] M. Postema, *Fundamentals of Medical Ultrasonics*. London: CRC Press, 2011.

[3] H. Kuttruff, *Ultrasonics: Fundamentals and Applications*. Springer Netherlands, 1991.

[4] F. R. Young, *Cavitation*. ICP, 1999.

[5] J. D. N. Cheeke, *Fundamentals and Applications of Ultrasonic Waves*, J. David and N. Cheeke, Eds. CRC Press, Dec. 2017.

[6] P. W. Atkins and J. de Paula, *Atkins' Physical chemistry*. New York: W.H. Freeman, 2006.

[7] M. Postema, *Medical bubbles*. Universal Press Veenendaal, 2004.

[8] N. Kudo *et al.*, 'Asymmetric oscillations of endoskeletal antibubbles,' *Japanese Journal of Applied Physics*, vol. 59, no. SK, SKKE02, Mar. 2020.

[9] M. Postema, A. Novell, C. Sennoga, A. T. Poortinga and A. Bouakaz, 'Harmonic response from microscopic antibubbles,' *Applied Acoustics*, vol. 137, pp. 148–150, Aug. 2018.

[10] S. Kotopoulis, K. Johansen, O. Gilja, A. Poortinga and M. Postema, 'Acoustically active antibubbles,' *Acta Physica Polonica A*, vol. 127, no. 1, pp. 99–102, Jan. 2015.

[11] T. G. Leighton, A. J. Walton and M. J. W. Pickworth, 'Primary bjerknes forces,' *European Journal of Physics*, vol. 11, no. 1, pp. 47–50, Jan. 1990.

[12] S. Kotopoulis and M. Postema, 'Microfoam formation in a capillary,' *Ultrasonics*, vol. 50, no. 2, pp. 260–268, Feb. 2010.

[13] K. Johansen, S. Kotopoulis, A. T. Poortinga and M. Postema, 'Nonlinear echoes from encapsulated antibubbles,' *Physics Procedia*, vol. 70, pp. 1079–1082, 2015.

[14] M. Postema *et al.*, 'Ultrasonic identification technique in recycling of lithium ion batteries,' in *2019 IEEE AFRICON*, IEEE, Sep. 2019.

Appendix H

Proposed partition coefficient microscopy setup

The system flowchart of the proposed setup of the apparatus is given in Figure H.1. The setup is extended and modified from the original setup in Section 3.2. The proposed setup here includes a brightfield light microscope and a high-speed camera. The microscope and high-speed camera incorporate the imaging into the ultrasonic setup for in-situ analysis, and thus the separate imaging setup in Section 3.2 is omitted. The rest of the ultrasonic setup is practically identical to Section 3.2.

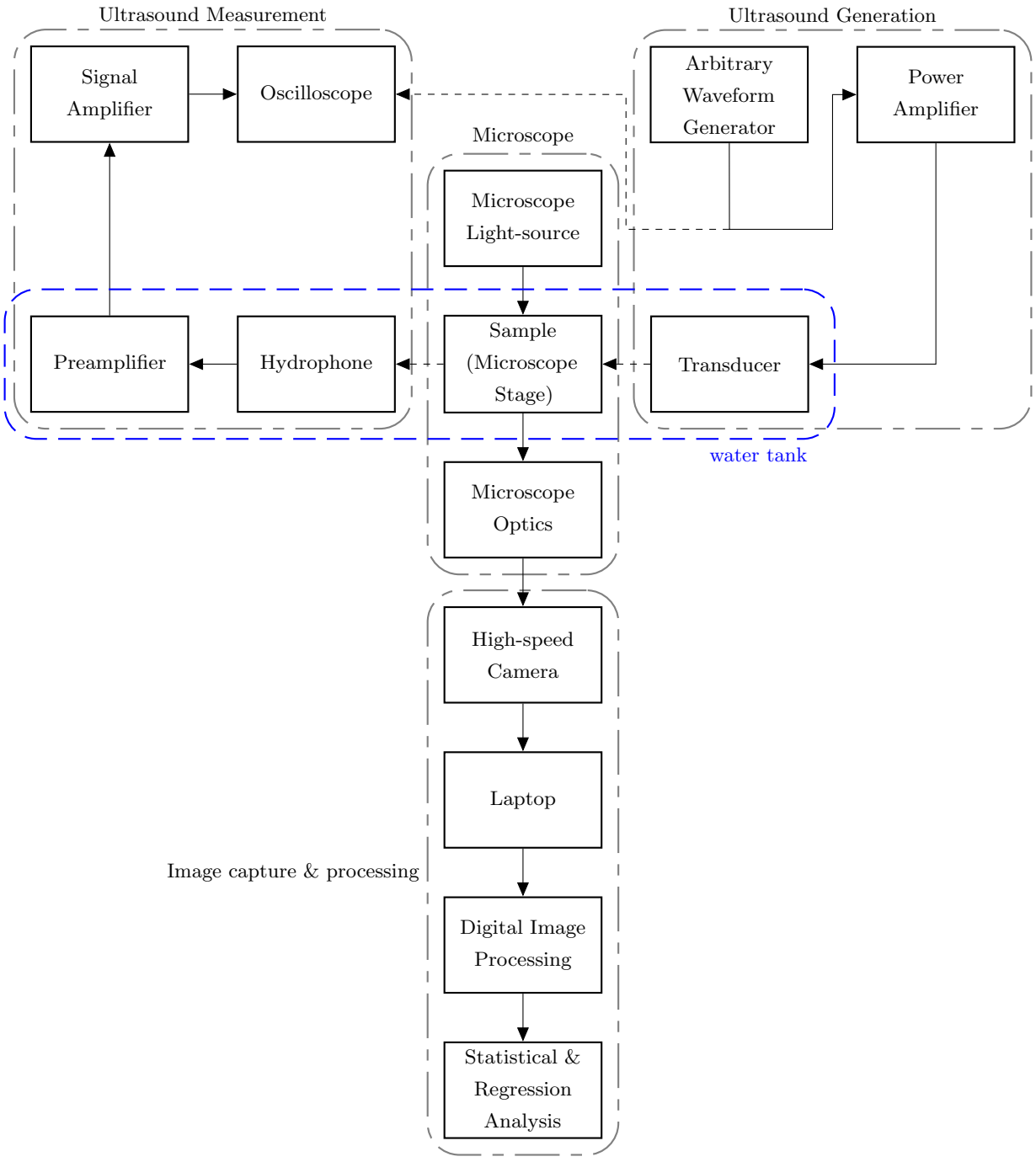

Figure H.1: Block diagram of partition coefficient microscopy setup

H.1 setup details

An arbitrary waveform generator (AFG3022B, Tektronix, Inc., Beaverton, Oregon, USA) is used to produce the electrical signal desired. This signal is split and measured with the oscilloscope (DPO4034, Tektronix, Inc., Beaverton, OR, USA) for signal verification and measurement purposes. The other signal is fed to a power amplifier (A150 RF, Precision Acoustics Ltd. (Electronics & Innovation Ltd.)). The amplified signal is then connected to the custom ultrasound transducer.

The transducer is located in a custom-built Perspex tank and is submerged in degassed reverse osmosis water. The tank is attached to a microscope (CKX31 inverted microscope, Olympus Corporation, Tokyo, Japan). The microscope is oriented so that a sample container's octanol-water boundary is coplanar to the microscope's optical axis and the transducer's acoustic axis. A high-speed camera (FASTCAM MC2.1, Photron (EU) Ltd., Wetzlar, Germany) is attached to an eyepiece of the microscope. The laptop controls the camera, which also serves as the storage and processing device.

The octanol-water partitioned microparticle sample contained in a container is submerged in water. The submerged container is placed directly between the front of the transducer and the hydrophone-preamplifier (HGL-0200 and AH-2010-025, Onda Corp., California, USA), all of which are submerged. Here, the submerged container is exposed to the desired ultrasound regime within the tank. The container is held with a custom-made 3D printed stand (Ultimaker PLA). The transducer and hydrophone are appropriately spaced away from the sample container. The acoustic signal from the hydrophone-preamplifier is measured directly with the oscilloscope. A schematic of the microscope and tank with the transducer and a sample is given in Figure H.2.

Note: the container should be, and may necessarily need to be, thin or at least "optically flat" along the microscope image axis. This is to ensure that the different refractive indices do not significantly distort the field depth of the microscope. This would also impact the numerical aperture, which could affect the quality of the image and imaging process The optical effects of the octanol-water interface need to be adequately assessed and possibly quantified to determine the imaging method's validity.

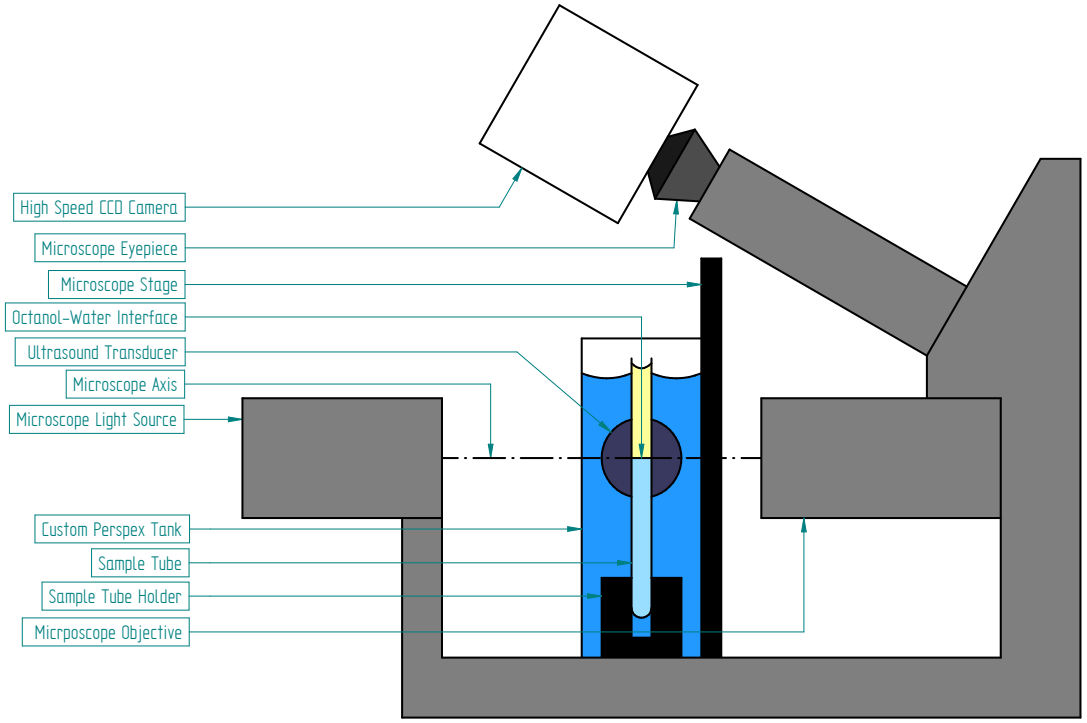

Figure H.2: Partition coefficient microscopy setup

H.2 Proposed protocol

A brief protocol is provided here for a better context of the experimental setup. Essentially the protocol is similar to the standard process of exposure in Chapter 3, but modified for in-situ observations.

The sample is prepared and partitioned prior to sonication. The octanol-water interface of the sample is moved into the field of view and focused. The desired acoustic parameters are set for the experiment as required. The camera and arbitrary waveform generator are pulse-controlled with the desired duty cycle and duration. The acoustically exposed samples are simply observed and recorded for the duration of the pulsed exposure using the high-speed camera. Essentially the partitioning phenomenon and the associated acoustic phenomenon of hydrophobic microparticles are recorded in situ. It is expected that the microparticles will be seen nucleating and transitioning between the phases as the hydrophobicity of each microparticle in the field of view is changed sonically. The core work of the methodology then lies in the digital image post-processing (DIP) algorithm.

The algorithm can be adopted from Chapter 3 and Appendix D, and further developed as necessary. The important modification is to use a region of interest (ROI) algorithm to find the partition boundary and each microparticle/antibubble in the field of view. The particles can then be counted and used as a representation of the molar concentration in each boundary. This is essentially a discretised form of colourimetry; or even a direct concentration measurement through molar measurement and physical counting. This analysis can provide a crude and modified in-situ partition coefficient measurement that can be determined for each image frame. These results can be cross-examined and compared with the nucleation analysis algorithm of hydrophobic microparticles. This analysis would then clarify the associated change in microparticle hydrophobicity caused by ultrasound through the partition coefficient and link it more conclusively with microparticle acoustic nucleation.